

**Mechanical Behaviour of  
Single Crystal, Polycrystalline and Nanocrystalline  
Metallic Nanopillars Under Compression**

by

Zeinab Jahed Motlagh

A thesis

presented to the University of Waterloo

in fulfilment of the

thesis requirement for the degree of

Master of Applied Science

in

Mechanical Engineering

Waterloo, Ontario, Canada, 2011

© Zeinab Jahed Motlagh 2011

## **Author's Declaration**

I hereby declare that I am the sole author of this thesis. This is a true copy of the thesis, including any required final revisions, as accepted by my examiners.

I understand that my thesis may be made electronically available to the public.

## **Abstract**

Fabrication techniques, and mechanical behaviours of vertically aligned cylindrical nanopillars of various metals, including tin, bismuth, palladium, indium, rhodium and cobalt have been presented in this work.

These, vertically aligned, cylindrical nanopillars of various diameters have been fabricated via an electron beam lithography and electroplating method. Microstructural properties of these pillars were studied using high resolution scanning electron and transmission electron microscopy. A non-destructive synchrotron X-ray microdiffraction ( $\mu$ SXRD) technique was used for the characterization of tin and indium nanopillars.

The results indicated single crystal body-centered tetragonal structured tin, polycrystalline rhombohedral bismuth, single crystal tetragonal indium, and nanocrystalline palladium, cobalt and rhodium nanopillars. The mechanical properties of these structures were studied by uniaxial compression under a nanoindenter outfitted with a flat punch diamond tip. The strain rate sensitivities and flow stresses were analyzed for each material.

Single crystal tin and indium nanopillars showed size-dependent flow stresses where smaller diameter pillars exhibit greater attained strengths. The observed size-dependence matches closely to that previously reported for single-crystalline face centered cubic metals at the nanoscale.

Polycrystalline bismuth nanopillars showed a size effect with a change in the deformation mechanism from grain boundary mediated mechanisms to dislocation processes as the pillar diameter approached the average grain size. Nanocrystalline palladium pillars showed an inverse size effect where a decrease in strength was seen for pillars with smaller diameters.

Finally, a thorough study is presented on the buckling behaviours of 130nm diameter palladium, cobalt and rhodium nanocrystalline pillars with various height-to-diameter ratios and the elastic moduli of these materials are extracted.

## Acknowledgments

Thanks to my supervisors, Dr. Tsui, for his constant availability and guidance throughout my masters degree and Prof. Sullivan for her support.

I thank my parents: my mom for her unconditional love and support and my dad for inspiring and encouraging me to do what I do today.

Thanks to the most important people in my life: MSN, ZJ, FJ, MJ, AJ, HJ, JC, AT and ASN, who have always been there for me and tolerated more than a year of “No, I’m too busy, I don’t have the time”.

Many thanks AT, JC and ED for proof reading my thesis

Finally, I must thank my colleagues:

MJ Burek, for the initiation of this project, and his guidance and expertise in this area of research.

Sumin, for speeding up the research with her help.

And SB for always finding wrong reasons to smile, in the basement of C2.

I would like to thank Aju Jugessur and Edward Xu for assistance with operation of the Leica EBPG5000+ electron beam lithography system and gratefully acknowledge the critical support and infrastructure provided for this work by the Emerging Communications Technology Institute at the University of Toronto. The characterization by a non-destructive synchrotron X-ray microdiffraction ( $\mu$ SXRD) presented in this work was done by Arief Suriadi Budiman at Lawrence Berkeley National Laboratory and University of California, Berkeley, California. The TEM research described in this work was performed at the Canadian Centre for Electron Microscopy, which is supported by the NSERC and other government agencies.

The results presented in chapters 2 and 3 of this work have also been published in two journal papers (ref. [104] and [110]).

*“Argument is conclusive, but it does not remove doubt, so that the mind may rest in the sure knowledge of the truth, unless it finds it by the method of experiment”*

- Doctor Mirabilis

## Table of Contents

Author's declaration	ii
Abstract	iii
Acknowledgements	iv
List of figures	ix
Chapter 1: Introduction	1
1.1 Bulk Scale Mechanical Compression and Tensile Tests	1
1.2 Plastic Deformation Mechanisms of Metals	2
1.2.1 Dislocation Creep	2
1.2.2 Grain Boundary Sliding	2
1.3 Micro and Nano Scale Mechanical Testing	3
1.3.1 Conventional Nanoindentation Experiments	3
1.3.2 Micro-Compression Tests	5
1.3.3 Compression Test Specimen Preparation	5
1.3.4 Size Dependant Behaviour of Material	8
Chapter 2: Mechanical Behavior of Single Crystal Tin Nanostructures	10
2.1 Background on Sn Applications and Mechanical Properties	10
2.2 Experimental methods	12
2.2.1 Fabrication of Pillars	12
2.2.2 Microstructural Characterization Using Synchrotron X-ray Microdiffraction	15
2.2.3 Pillar Compression	16
2.3 Results and Discussion	17
2.3.1 Fabrication of Pillars	18
2.3.2 Post Compression Pillar Analysis	24
2.3.3 Strain Rate Sensitivity	28
2.3.4 $\mu$ SXRD Study of Deformed Tin Nanopillars	34
2.4 Conclusions and Recommendations	38

Chapter 3: Polycrystalline Bismuth Nanostructures .....	39
3.1 Background on Bi applications and Mechanical Properties .....	39
3.2 Experimental Methods .....	41
3.2.1 Pillar Fabrication .....	41
3.2.2 Pillar Compression.....	42
3.3 Results and Discussion.....	43
3.3.1 Stress-Strain Relationships and Size Effects .....	46
3.4 Conclusions.....	67
Chapter 4: Nano-crystalline Palladium.....	68
4.1 Background on Nanocrystalline Metals and Pd Applications .....	68
4.2 Experimental Methods .....	70
4.3 Results and Discussion.....	71
4.3.1 Fabricated Pillar Structures.....	71
4.3.2 Stress-Strain Relationships .....	72
4.3.3 Strain Rate Sensitivity .....	77
4.3.4 Size Effect.....	78
4.3.5 Conclusions and Recommendations .....	84
Chapter 5: Indium Nanostructures: A Sophisticated Behavior Under Micro-compression.....	85
5.1 Background .....	85
5.2 Experimental Methods .....	86
5.3 Results and Discussions .....	89
5.3.1 Strain Rate sensitivity (Stress Exponent).....	89
5.3.2 Size Effect.....	94
5.3.3 Reaching Theoretical Strength.....	103
5.3.4 Mechanical Annealing (Dislocation Annihilation) .....	106
5.4 Conclusions.....	110
Chapter 6: Inelastic Buckling of Palladium, Cobalt and Rhodium Nanopillars .....	111
6.1 Introduction.....	111

6.2	Experimental Methods .....	113
6.2.1	Electron Beam Lithography Process .....	113
6.2.2	Nano-pillar Electroplating .....	114
6.2.3	Uniaxial Compression Testing.....	115
6.3	Results and Discussions .....	116
6.3.1	Nanopillar Geometry and Microstructure .....	116
6.3.2	Post Compression SEM Analysis .....	121
6.3.3	Load-Displacement Behaviors.....	126
6.4	Conclusions.....	141
Chapter 7: Conclusions and Future Research Directions.....		142
7.1	Micro-tensile Tests.....	142
7.2	Variable Temperature Tests .....	143
7.3	Statistical Analysis .....	146
7.4	In-situ Experimentss.....	148
Bibliography .....		149

## List of Figures

Figure 1.1: Commercially available nanoindentation system for micro compression tests (*adapted from [1]*)

Figure 2.1: Nanopillar fabrication process

Figure 2.2:(a) SEM image of an array of  $\sim 950$  nm diameter tin nanopillars showing characteristic disproportionate plating with many overplated specimens. (b) Close up SEM image of a typical overplated tin nanopillar

Figure 2.3: SEM images of as-fabricated tin nanopillars with diameters of (a) 920, (b) 590 nm, (c) 335 nm, (d) 130 nm, and (e) 70 nm. All SEM images taken at a 70° stage tilt

Figure 2.4: Representative quantitative  $\mu$ SXRD analysis of an uncompressed  $\sim 920$  nm diameter tin nanopillar. (a) SEM image of the tin nanopillar and (b) Laue diffraction pattern generated throughout the nanopillar volume (c) (406) Laue diffraction peak; (d) (624) Laue diffraction peak.

Figure 2.5: (a) The peak broadening due to crystal rotation of the (406) Laue diffraction spot. (b) This Laue spot has a FWHM of  $0.439^\circ$ . It was measured from the intensity line scan in (a).

Figure 2.6: Representative engineering stress–strain curves for tin nanopillars with diameters of (a) 920nm, (b) 560nm, and (c) 350nm. All deformed with strain rate of  $\sim 0.001$  s<sup>-1</sup>.

Figure 2.7: Pre and post compression SEM images of  $\sim 920$  nm diameter tin nanopillars.

Figure 2.8: Pre and post compression SEM images of  $\sim 560$  nm diameter tin nanopillars

Figure 2.9: Pre and post compression SEM images of  $\sim 350$  nm diameter tin nanopillars.

Figure 2.10: (a) Log – log plot of engineering flow stress measured at  $\sim 5\%$  strain as a function of engineering strain rate for all tin nanopillars tested in this work.

Figure 2.11: Log – log plot of engineering flow stress measured at  $\sim 5\%$  strain as a function of pillar diameters. These samples were compressed at a  $\sim 0.001$  s<sup>-1</sup> strain rate. The errors bars indicate one standard deviation.

Figure 2.12: Representative quantitative  $\mu$ SXRD analysis of a  $\sim 950$  nm diameter tin nanopillar after uniaxial compression to  $\sim 22$  % engineering strain. Pre and post compression SEM images of the tin nanopillar are shown in (a) and (b) respectively, with the corresponding engineering stress – strain curve displayed in (c).

Figure 2.13: Representative quantitative  $\mu$ SXRD analysis of a  $\sim 920$  nm diameter tin nanopillar after uniaxial compression to  $\sim 22$  % engineering strain. Laue diffraction spots of (204) and (105) are shown in (a) and (b) respectively. The axes used for intensity measurements are illustrated in (c). The peak intensity of the (204) Laue diffraction spot (d) yields a FWHM of  $0.458^\circ$ .

Figure 3.1: SEM images of as-fabricated bismuth nanopillars with diameters of (a) 1100 nm, (b) 840 nm, (c) 540 nm, (d) 230 nm, and (e) 130 nm. All SEM images taken at a  $70^\circ$  stage tilt.

Figure 3.2: (a) TEM bright field image and (b) TEM dark field image of an 1100 nm diameter bismuth nanopillar. The grain boundaries of this nanostructure are highlighted in (b).

Figure 3.3: Representative engineering stress – strain curves for bismuth nanopillars. All specimens were deformed with a strain rate of  $10^{-3} \text{ s}^{-1}$

Figure 3.4: Post-compression SEM images of (a) 1100 nm, (b) 840 nm, (c) 540 nm, (d) 230nm, and (e) 130 nm diameter bismuth nanopillars. Additional post-compression SEM images of (f) 1100 nm and (g) 540 nm diameter specimens to illustrate the transition in deformation mechanism from grain boundary mediated deformation to deformation dominated by dislocation glide. All SEM images taken at a  $70^\circ$  stage tilt.

Figure 3.5: Log – log plots of engineering flow stress measured at 5.0 % strain as a function of engineering strain rate for (a) 1100 nm, (b) 840 nm, (c) 540 nm, (d) 230nm, and (e) 130 nm diameter bismuth nanopillars. The average flow stress values are indicated by blue circles with error bars indicating one standard deviation.

Figure 3.6: (a) Log – log plot of averaged engineering strain rate as a function of engineering flow stress measured at 5.0 % strain and (b) linear plot of engineering flow stress measured at 5.0 % engineering strain as a function of nanopillar diameter. (c) Log-log plot of engineering flow stress measured at 5.0 % engineering strain for 540 nm, 230 nm, and 130nm diameter nanopillars. The error bars indicate one standard deviation.

Figure 4.1: SEM images of as-fabricated palladium nanopillars with diameters of (a) 120, (b) 240 nm, (c) 540 nm. All SEM images taken at a 70° stage tilt

Figure 4.2: (a) TEM dark field image of the full length of a ~520 nm palladium nanopillars along with diffractoin pattern. (b) Dark field high magnification image of a section of the palladium nanopillar (c) Dark field high magnification image of a section of the palladium nanopillar

Figure 4.3: (a) TEM dark field image of the full length of a ~520 nm palladium nanopillars along with diffractoin pattern. (b) Dark field high magnification image of a section of the palladium nanopillar (c) Dark field high magnification image of a section of the palladium nanopillar

Figure 4.4: Engineering strain vs. engineering stress for 550 nm palladium nano-pillars under compression (b) SEM images of 240 nm palladium nano-pillars going through plastic deformation before (left) and after (right) compression

Figure 4.5: Engineering strain vs. engineering stress for 550 nm palladium nano-pillars under compression (b) SEM images of 240 nm palladium nano-pillars going through plastic deformation before (left) and after (right) compression

Figure 4.6: log-log plot of flow stress measured at 8% strain for 550 nm Pd nanopillars as a function of strain rate. Strain rate sensitivity  $\sim m=0.68$

Figure 4.7: Log-log plot of engineering flow stress measured at 8.0 % engineering strain for 550 nm, 240 nm, and 120nm diameter Pd nanopillars. The error bars indicate one standard deviation.

Figure 4.8: Representative engineering strain vs. engineering stress for 550nm, 240nm and 120 nm palladium nano-pillars under compression

Figure 5.1: Time-displacement plot showing constant displacement rates during the compression tests ranging between 0.2-20 nm/s

Figure 5.2: SEM images of Fabricated (a) 120 nm (b) 240 nm (c) 560 nm and (d) 1020 nm diameter Indium nanopillar

Figure 5.3: FIB cross sectioned indium nano pillar (a proof of pillar solidity)

Figure 5.4: Strain rate as a function of average flow stress at 5% strain for pillar diameters ranging from 140-1070nm- error bars correspond to standard deviation.

Figure 5.5: Flow stresses measured at 5% strain for two strain rates ( $\sim 0.001 \text{ s}^{-1}$  and  $\sim 0.01 \text{ s}^{-1}$ ) and pillar diameters ranging from 140-1070nm

Figure 5.6: (a) log-log plot of flow stress at 5% strain as a function of pillar diameter (b) linear plot of flow stress at 5% strain as a function of pillar diameter

Figure 5.7: Engineering stress vs. engineering strain for 4 different pillar sizes

Figure 5.8: SEM images of (a) 1070 nm, (b) 560 nm, (c) 240 nm (d) 120 nm indium nanopillars before (left) and after (right) compression

Figure 5.9: Engineering strain vs. engineering stress for 240 nm indium nano-pillars going through type I and type II deformation

Figure 5.10: SEM images of 240 nm indium nano-pillars going through (a) type I (b) and type II deformation before (left) and after (right) compression

Figure 5.11: Engineering strain vs. engineering stress for two  $\sim 240$  nm indium nano-pillars (shown in figure 5.12) going through type III deformation

Figure 5.12: SEM images of  $\sim 240$  nm indium nanopillars going through type III deformation before (left) and after (right) compression (stress-strain relations shown in figure 5.11)

Figure 5.13: Ni single crystal nanopillars before (a) and after (b) compression and representative displacement vs stress curve (d)

Figure 6.1: SEM micrographs of as-fabricated (a) palladium, (b) cobalt, and (c) rhodium nanopillars. All structures have diameters of  $\sim 130$ nm and aspect ratio (L/r) near 10. All SEM images taken at a 70o stage tilt.

Figure 6.2: (a) TEM dark field image of the full length of a 520 nm palladium nanopillar along with diffraction pattern. (b) TEM dark field image of the full length of a  $\sim 520$  nm cobalt nano-pillar along with diffraction pattern. (c) High magnification SEM image of 1050nm rhodium nanopillar

Figure 6.3: Post compression SEM micrographs of palladium nanopillars with aspect ratios ( $L/r$ ) of (a) 3.4, (b) 8, and (c) 18.

Figure 6.4: Post compression SEM micrographs of cobalt pillars with aspect ratios ( $L/r$ ) of (a) 5, (b) 7, and (c) 14

Figure 6.5: Post compression SEM micrographs of rhodium nanopillars with aspect ratios ( $L/r$ ) of (a) 5, (b) 7, and (c) 17.

Figure 6.6: Representative engineering stress – strain curves for 130 nm diameter (a) palladium, (b) cobalt, and (c) rhodium nanopillars. All pillars were deformed at a constant displacement rate of 1 nm/s.

Figure 6.7: Plot of critical buckling load as a function of aspect ratios ( $L/r$ ) for (a) palladium, (b) cobalt, and (c) rhodium nanopillars.

Figure 6.8: Critical buckling load of palladium ( $L/r = 16$ ), cobalt ( $L/r = 14$ ), and rhodium ( $L/r = 11$ ) nanopillars at different displacement rates.

Figure 6.9: Plot of critical buckling load as a function of effective area  $\pi^2 I / (KL)^2$  for (a) palladium, (b) cobalt, and (c) rhodium nanopillars.

Figure 7.1: High temperature flow stresses at 5% strain for 1  $\mu$ m indium nanopillars at 2 different strain rates compared to room temperature tests

Figure 7.2: High temperature flow stresses at 5% strain for 200nm indium nanopillars at 3 different strain rates compared to room temperature tests

Figure 7.3: Indium ~1070 nm pillars showing two different forms of deformation : (a) barrelling (b) barrelling followed by plastic crystallographic shear

## Chapter 1: Introduction

### 1.1 Bulk Scale Mechanical Compression and Tensile Tests

Tension and compression tests are the most common types of mechanical testing of materials in bulk scale. According to the American Society for Testing and Materials (ASTM), the yield strength, yield point, Young's modulus, stress-strain curve, and the compressive strength of a material can be obtained from a standard compression test. However, these tests are mostly used to find the relationship between the average normal stress and the normal strain of materials.

If the material does not fail due to a shattering fracture, and it does not go through buckling or barrelling, the compressive strength of the material is dependent on the strain and the geometry of the test specimen.

In a compression test the materials to be tested are specially prepared in the form of a right circular cylinder with a flat surface at both ends and are dimensioned in a way to avoid buckling. The test specimen is then compressed and the applied load and the deformation (change of length) of the pillar are recorded at frequent intervals. The stress-strain relationship can be evaluated by the translation of load and displacement to stress and strain respectively. The average normal Stress ( $\sigma$ ) is calculated as below:

$$\sigma = \frac{F}{A}$$

Where  $F$  is an external force applied uniaxially on the test specimen and  $A$  is the cross sectional area of the cylinder on which the load is applied. There are two common methods of evaluating the cross sectional area; If the initial cross sectional area of the test specimen is used for the evaluation of stress, it is known as *engineering stress*. If the calculations include the changes in area at each instant of the test, the stress can be evaluated as the load divided by the cross sectional area at each instant, known as the *true stress*.

Strain ( $\epsilon$ ) is simply a measure of relative deformation of a body. This deformation can be explained as a vector representing the *displacement* of each point on a deformed material relative to its initial position.

The engineering normal strain which is commonly evaluated in compression tests can be evaluated as below:

$$\epsilon = \frac{\Delta l}{l_0}$$

where  $l_0$  is the initial length, and  $\Delta l$  is the change in length of the test specimen.

The stress-strain curve shows the elastic and plastic behaviour of the material. In a compression test, the curve begins with a region where the material follows Hooke's Law which states a linear relationship between the stress and strain, until the material yields at its *Yield point*. This is known as elastic behaviour: if the load is removed anywhere in this region, the material will return to its initial shape. Beyond this point, the material deforms plastically and will not return to its original shape and length if the applied load is removed. Most materials deform plastically; our interest is in the plastic deformation of metals. The various reasons behind this deformation are known as *deformation mechanisms*.

## 1.2 Plastic Deformation Mechanisms of Metals

### 1.2.1 Dislocation Creep

The plastic deformation of metals is usually associated with the existence of defects known as *dislocations*. A dislocation is a one-dimensional crystallographic defect in a crystal structure. It's what deviates the structure from a perfect defect-free crystal and corresponds to dislocated atoms in the structure. The atoms can be dislocated in two ways: *edge and screw dislocations*.

The movement of dislocations through the crystal under stress results in the plastic deformation of the material. Therefore, the plastic behaviour of material depends on the density (length of dislocation lines per volume) and dynamic properties of these dislocations [1].

### 1.2.2 Grain Boundary Sliding

Grain boundaries are two dimensional defects that result in the plastic deformation of polycrystalline materials. They are the interface between two grains in a polycrystalline material.

Grain boundaries limit the movement of dislocations and therefore reducing the grain size of materials is

a common method of strengthening materials; the dislocations will need more energy to change direction and move between grains. This is known as the Hall-Petch effect which will be discussed in detail in Chapter 5.

### **1.3 Micro and Nano Scale Mechanical Testing**

The study of materials in nano and submicron scale has been the focus of many researchers in recent years. There are various reasons why a material's nanoscale properties matter. First and foremost, there are several sources that show that materials behave differently in submicron and nano dimensions [2]. The strength of material, specifically, is known to increase when the size of the samples reaches the size of the material microstructures.

It is very important to take into consideration the inaccuracies in results due to erroneous testing methods in this scale. Recently, many testing methodologies have been presented with the attempt to minimize the inaccuracies of existing mechanical testing methodologies in micro and nano scale.

#### **1.3.1 Conventional Nanoindentation Experiments**

Nanoindentation is a common and powerful tool for measuring the elastic modulus (E) and hardness (H) of a material; generally in this method, a three sided pyramid shaped indenter tip known as a Berkovich tip, is indented into a test sample. The E and H values are extracted based on the analysis of unloading data obtained from a cycle of loading and unloading [3]. One disadvantage of the conventional indentation methods is that it does not allow the direct measurement of the flow stress; the flow stresses are calculated with the assumption that the hardness and yield strength are linearly related [33].

Although this method is widely used in determining the hardness of thin films, it has been argued that the properties of the substrate, to which these thin films are attached, can affect the results of the nano-indentation tests [4]. Nix Et al. studied the effect of substrate on the nano-indentation measurement of film properties and found that this effect was mostly evident in the case of hard films on a soft substrate [5]. Other indentation uncertainties have been extensively studied on events such as sink-in and pile-ups of the material in response to tip penetration. Studies by Pharr and Tsui show an overestimation of film

hardness as much as 68% in the case of soft films on hard substrates [6] and up to 100% (depending on penetration) in hard films on soft substrates [7] due to a “substrate-induced enhancement of indentation pile-up”.

Another important concern with the conventional nanoindentation method is the geometry of the nano-indenter tip and the introduction of strain gradients. During nano-indentation, only a small volume under the indenter is plastically deformed hence the introduction of non-uniform stresses and strains.

N.A. Sakharova et al. studied this effect for 3 common indenter tip geometries (Berkovich, Vickers and Conical) and found that distinct mechanical properties were seen for some materials using different indenter geometries. The depth at which the material plastically deforms is also dependant on the geometry of the tip [8].

A study on the nanoindentation of nanocrystalline Ni with geometrically different indenters showed a strong dependence of the material hardness on indenter geometry [9]. The common pyramid shaped indenter tips create a localized stress concentration at the tip and edge points of contact with the test surface, which results in a non-uniform strain and stress distribution.

All the above reasons highlight the need for a more precise testing method for accurately characterizing time dependant mechanical properties of material at nano scale.

### 1.3.2 Micro-Compression Tests

Uniaxial compression tests on cylindrical pillars, known as “micro-compression tests” were first implemented by Uchic et al to overcome the strain gradient effects of previous nanoindentation methods [10]. This method allows the study of the flow properties of material in small scale.

The test consists of the preparation of nano and micron scale cylindrical pillars of the material to be tested, followed by the compression of these pillars using a nano-indenter by replacing the Berkovich tip with a flat diamond tip, which distributes a homogeneous stress-strain throughout the specimen. Figure 1.1 shows a schematic of commercially available nano-indentation systems for micro-compression tests and the relative position of the test specimens [2]. This tool allows the collection of load, displacement, displacement rate and harmonic contact stiffness data at frequent intervals. Using this data, several mechanical parameters such as stress-strain characteristics and strain rate effects on flow stress can be extracted. With this method, pillars with a finite number of dislocations can be fabricated and tested; thereby allowing the study of dislocation movement through the pillar volume and also the interactions of the dislocations with nearby free surfaces [4].

This method has been used extensively for the studies of a small sub-set of single crystalline metals (i.e. Ni ([11]-[14], Au ([15]-[20]), Cu ([21]-[24]), Mo ([4],[19],[25]-[29]) and others ([27], [29]-[33]) with cubic structures with relatively high melting temperatures mostly with a homologous temperatures less than 0.5. With the exception of some experimental work that has been done on Indium [33], there has been little focus on metals with low melting temperatures.

### 1.3.3 Compression Test Specimen Preparation

Various methods have been implemented for preparing the pillars used for the micro-compression tests. FIB milling is the most common method, where the nano or micron sized pillar is milled out of a bulk crystal using a focused  $\text{Ga}^+$  ion beam. A drawback of this method that has been addressed in literature is the potential defects caused by  $\text{Ga}^+$  penetration into the pillar through the milling process ( $\text{Ga}^+$  implantation); however, the value of this penetration is known to be no more than 60nm [16]. Besides  $\text{Ga}^+$

implantation, another disadvantage of the FIB technique, and most other techniques, is that the test specimen is not free standing, as it would be in a bulk mechanical compression test. Since one end of the pillar is fixed, the boundary conditions differ from that of a standard compression test. This can be compared to the aforementioned effects of hard tests specimens on soft substrates during conventional nano-indentation tests. Although attempts have been made to correct for the lateral movement of the pillar into the substrate and the plastic deformation of the substrate in the analysis of the stress strain curves, the effect of the possible plastic deformation (when the fabricated pillars are stronger than the substrate they are attached to) is rarely addressed. This can happen when the fabricated pillars are initially defect free, or become dislocation free during the compression process (dislocation annihilation) [34]. Therefore the bulk substrate, though of the same material, becomes much softer than the pillar itself. Finally, the fabrication time of these pillars can be very long, even multiple days in the case of larger pillars sizes [35].

Another method recently used for the fabrication of the test specimens is electroplating the metal into photo-resist templates patterned by photolithography [36]. Substrate deflection is minimal in electroplated pillars which are fabricated on a substrate much harder than the metal that is being tested.

Greer et al. compared the strength of FIB milled Ni pillars versus electroplated pillars and the results showed that the electroplated pillars were generally stronger on average. However, despite which method is used for the fabrication of the compression test specimens, the pillars have shown a “size effect” in the value of flow stress in terms of a relationship between the flow stress and pillar diameter [16]. This size effect has been seen in all studies of FCC nanopillars to date and will be discussed in detail in the following section.

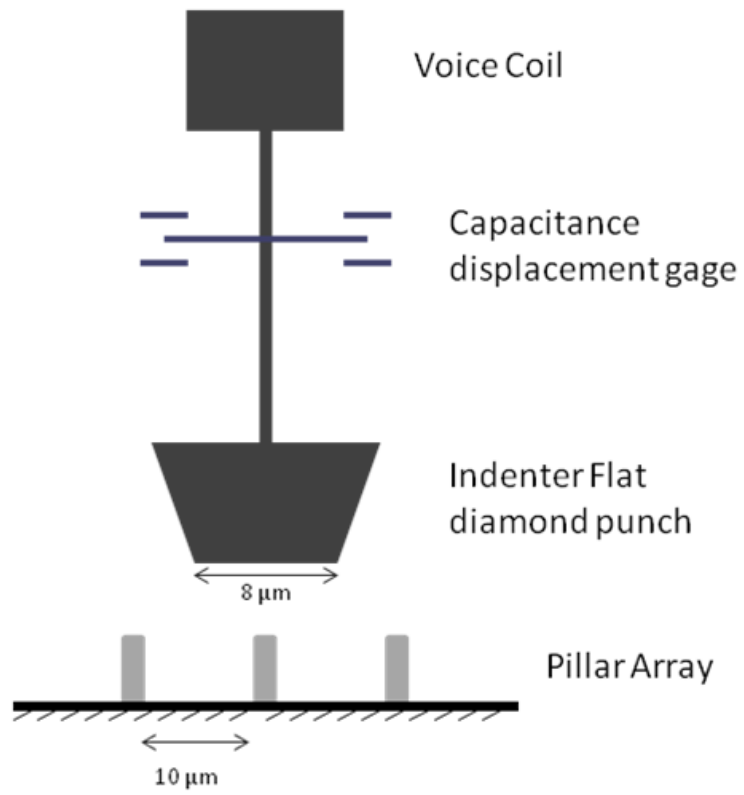


Figure 1.1: Commercially available Nanoindentation System for micro compression tests (adapted from [1])

### 1.3.4 Size Dependant Behaviour of Material

If a structure with nano scale dimensions is a single crystal consisting of a single grain (i.e. no two dimensional defects) and very few or no dislocations, it is reasonable to assume the material will deform at very high strengths near theoretical strength. Size-dependant mechanical properties of materials have become a great area of focus for researchers in the past decade.

All studies on single-crystalline FIB-fabricated ([11]-[33]) and electroplated ([16],[23]) nanopillars have shown an inverse relationship between pillar diameter ( $D$ ) and flow stress ( $\sigma$ ), as illustrated below:

$$\sigma \propto D^{-\gamma}$$

The parameter  $\gamma$  is the power-law exponent. Uchic *et al.* showed in their work that most size dependent strengthening data for nanoscale FCC single-crystalline metals, such as Ni, Au, Cu, and Al, could be collapsed onto a single line by plotting the normalized resolved shear effective stress versus pillar diameter [2]. The result of this normalization showed that a power-law exponent of  $\sim -0.6$  was for studied FCC metals [2]. However, even though higher strengths have been achieved in smaller dimensions, these strengths are far from theoretical strengths.

An overwhelming majority of experimental work has been concentrated on a small subset of single-crystalline metals with cubic structures and high melting temperatures (i.e. Ni ([11]-[14], Au ([15]-[20]), Cu ([21]-[24]), Mo ([4],[19],[25]-[29]) and others ([27], [29]-[33])). Several sound theories have been presented to explain this size dependant behaviour of cubic single-crystalline nanostructures. However, there remains a need for the study of other classes of material in nano-scale. Polycrystalline nanostructures and low melting point metals with low symmetry crystal structures are among the material classes that have rarely been studied [33]. Also, properties such as strain rate sensitivity have often not been addressed.

In this work the plastic deformation of single crystal tin, with a body centered tetragonal crystal structure, rhombohedra polycrystalline bismuth, nanocrystalline face centered cubic palladium and tetragonal indium single crystal nano-pillars is presented. Different size-dependant behaviour is seen for each material based on the pillar diameter. Tin and indium single crystals show similar results as previously

studied single crystals; the pillars get stronger as the pillar size decreases. In bismuth nanopillars, the pillars begin to get stronger only for pillar sizes less than a certain diameter. Finally, for palladium nanocrystalline pillars with grain sizes less than 50nm, an inverse size effect is seen. For this material and pillar structure, a decrease in pillar size results in an increase in flow stress. Chapters 2-5 present experimental work and results for each of these 4 materials and presents possible theories to explain the behaviour of these four metals in nano dimensions.

## Chapter 2: Mechanical Behavior of Single Crystal Tin Nanostructures

### 2.1 Background on Sn Applications and Mechanical Properties

Tin, with its low melting temperature, ductility, excellent wetting properties, high electrical conductivity and high electrical reliability ([37]-[39]), is often known as a promising replacement for lead in the microelectronics industry. It is used for elemental metal and alloy solders for chip packaging.

Since tin and tin-alloy structures used in microelectronic solder technology are part of the load bearing components, their mechanical properties approaching the nanometer scale are critically important for product reliability and lifetime. Another interesting application of tin is in the area of lithium ion battery anodes, where nanostructured tin-based anodes are being studied in order to improve charge storage and anode lifetime [40]. Thorough understandings of nanoscale tin deformation mechanisms are needed in order to attain the desired functionality and lifetime of these small-scale components.

This study seeks to achieve two goals: First, a process is presented for the fabrication of cylindrical tin nanopillars. Secondly, these fabricated pillars are utilized for the time dependent study of the mechanical behaviours of tin in micro and nano scale by uniaxial compressive loading (micro-compression tests).

The results presented here will help to understand how tin nanostructures behave during mechanical deformation. In addition, the new knowledge gained from this work will expand the current understanding in small-scale mechanical properties to the deformation mechanisms governing low melting temperature nanostructures. The melting temperature of tin is  $\sim 232$  °C, corresponding to a homologous temperature of approximately 0.6 in ambient conditions.

At room temperature, tin exists as its  $\beta$ -allotrope, also known as white tin. It has a body centered tetragonal (BCT) crystal structure with  $c/a = 0.5456$  [41]. According to Yang and Li, there are twelve possible slip systems in the tin crystal and at least six possible for BCT tin [41].

However, tin has shown to have three active slip systems under indentation at room temperature:

$(110)[\bar{1}11]$ ,  $(110)[001]$ ,  $(110)[010]$  [42]

The dimensions of the burger vectors are  $b[111] = 0.4411\text{nm}$ ,  $b[001] = 0.3157\text{ nm}$ ,  $b[010] =$

0.66293 nm [43]. The shear modulus of tin is 17.93 GPa at room temperature [43]. Like many other metals, bulk  $\beta$ -tin exhibits strain rate sensitivity where the flow stress varies with the deformation rate. Strain rate and other time dependent mechanical behaviours such as creep deformation, of bulk-scale tin have been studied in detail by Sherby [44], Frenkel *et al.* [45], Weertman and Breen [46], Breen and Weertman [47], Yang and Li [43], Chu and Li [42], Mohamed *et al.* [48], Raman and Berriche [49], and Mayo and Nix [50]. They observed that the relationship between the creep deformation rate ( $\dot{\epsilon}$ ) and stress ( $\sigma$ ) can be described by a simple relationship:

$$\dot{\epsilon} = K\sigma^n$$

Although tin has been extensively studied and characterized in bulk scale, and its mechanical properties have been well documented, to date there are no investigations on the small-scale deformation behaviours of tin nanostructures. Nearly all studies of material in nanoscale reveal that metals, when reduced to the nanoscale, exhibit remarkably different mechanical behaviour as compared to that in bulk [18] demonstrating the need for separate studies on material properties in nano scale.

## 2.2 Experimental methods

### 2.2.1 Fabrication of Pillars

In this chapter, the small scale plastic deformation of tin nanopillars were studied by uniaxial compression tests on vertically aligned, individually isolated nanopillars fabricated by electroplating techniques. As stated in Chapter 1, the electroplating method was chosen as a replacement for the FIB methods used in previous works to eliminate surface damage effects, which often associated with nanopillar fabrication techniques.

Figure 2.1 shows the integration scheme used to produce tin nanopillars. The fabrication method involves lithographic patterning of polymethylmethacrylate (PMMA) resist with electron beam lithography, followed by tin electroplating into the prescribed resist template. Preparation of the substrate began with Si (001) wafers, which were coated with a 20 nm-thick titanium adhesion layer and a 100 nm-thick gold layer deposited by electron beam evaporation. The metalized substrates were spin coated with various dilutions of 950 kD PMMA dissolved in anisole (MicroChem Corp.), then baked at 180 °C for approximately 15 minutes to cure the PMMA. An array of holes with various diameters was patterned in the PMMA resist by exposure; using a Leica EBPG 5000+ electron beam lithography system operating with an acceleration voltage of 100 kV. The patterned PMMA layer was developed in 1:3 solution of methylisobutylketone and isopropyl alcohol (IPA) for ~ 60 seconds followed by a five second rinse with IPA. The resulting feature size after PMMA development was holes of 70 to 920 nm in diameter. Before electroplating, the silicon wafer was diced into square 1 cm<sup>2</sup> chips with the patterned PMMA resist template in the chip center.

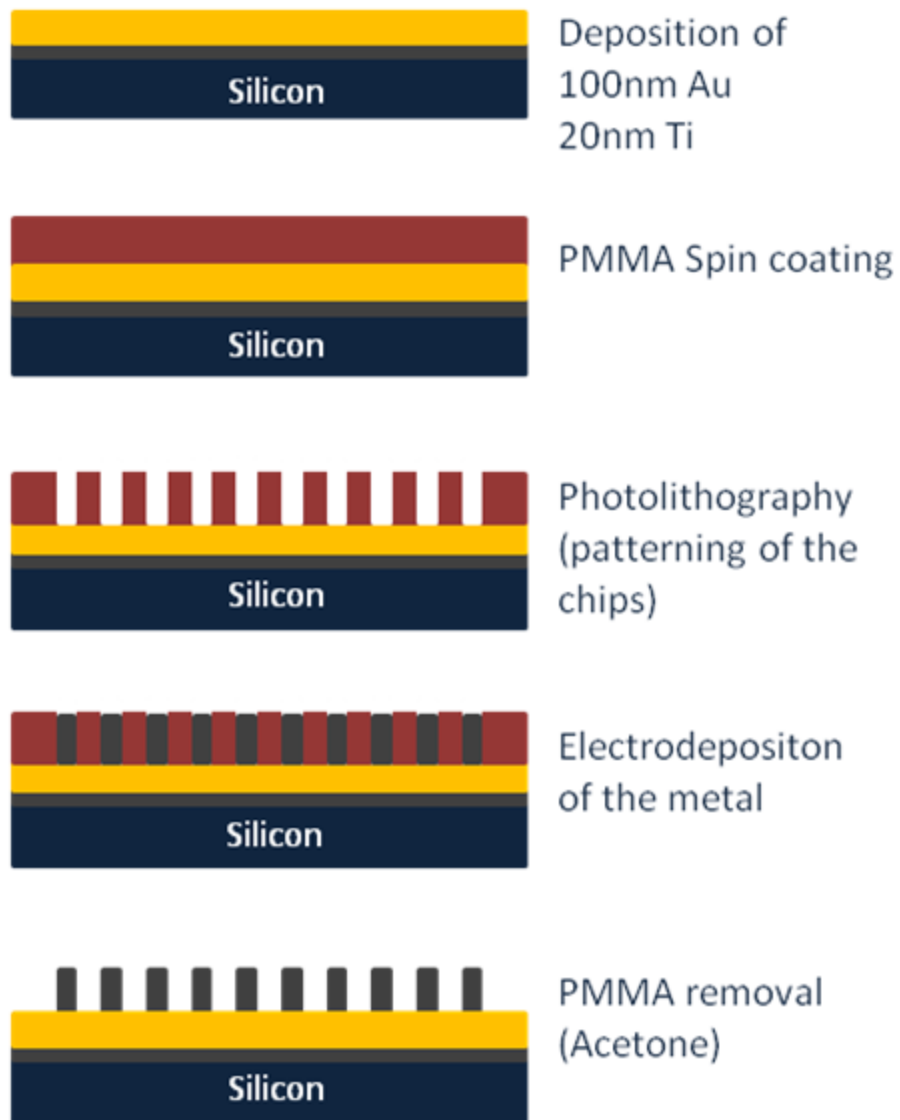


Figure 1.2: Nanopillar Fabrication Process

Tin electroplating was performed under alternating current conditions using a parallel two-electrode configuration. The tin plating solution was made in-house and consisted of 22 g/L tin(II) sulfate (95.5%, Alfa Aesar) and 75 g/L sulfuric acid. About 200 mL of the prepared solution was used for electroplating prior to deposition to ensure its homogeneity. The gold/titanium seed layer underneath the resist template acted as the cathode, and a high purity tin rod (6 mm diameter, 99.9985 %, Puratronic® from Alfa Aesar) was used as a soluble anode. The plating bath was maintained at room temperature and mechanically stirred throughout the deposition process. A Teflon backing and custom gold coated brass clips were used to mount the PMMA coated substrates in the solution and electrically interface with the gold/titanium cathode layer. The total cathode area, which included the patterned PMMA coated substrate, a blank 1 cm<sup>2</sup> chip, and the gold clips, was maintained at ~ 3.5 cm<sup>2</sup>, and the distance between the anode and the cathode was kept at approximately 25 mm.

Tin electroplating was initiated with a short current pulse at 50 mA/cm<sup>2</sup> for 5 seconds. This step was necessary to promote metal nucleation in all pores and to increase the final nanopillar yield and homogeneity. Subsequently, electroplating was conducted using an alternating current technique with 0.5 seconds of cathodic current at 7.5 mA/cm<sup>2</sup> followed by 0.1 seconds of anodic current at 5 mA/cm<sup>2</sup>. The alternating current technique was used to promote homogeneous deposition. Total plating times ranged from 15 to 60 minutes depending on the pillar diameter and desired aspect ratio, with shorter times for the smaller diameters. After the electrochemical deposition, the PMMA resist was stripped in acetone for at least 30 minutes. Prepared tin nanopillars are expected to have a native oxide thickness approximately 5 to 8 nm, which was observed by transmission electron microscopy of tin nanowires electroplated in polycarbonate membranes [51].

Using the above conditions, a yield of 100% was achieved for different sample sizes and the final chips consisted of 15625 pillars located in a 125x125 square array with a distance of 10 μm between pillars.

Among these samples, several pillars were investigated using a scanning electron microscope and pillars with a uniform cylindrical structure and a diameter to height aspect ratio of ~2-3 were selected and mapped for uniaxial compression tests. Based on simulation results by H. Zhang, this aspect ratio of two

does not exhibit stress misreading due to plastic buckling. Elastic Euler buckling is also not a concern in these experiments since it will not occur even for soft pillars for aspect ratios below 25 [5]. The samples were annealed at room temperature for a period of 2 weeks prior to compression.

The silicon chips with the pillar arrays were then mounted onto a flat stub using a lacquer. A lacquer was used in order to ensure that there is no lateral movement of the sample during the compression test and also to ensure the alignment of the pillars and the nano indenter. In his study, H. Zhang also simulates the effect of the alignment of the nano indenter on the accuracy of the compression tests and shows a decrease of the measured elastic modulus with an increase in the alignment of the pillar and indenter (i.e. the angle between the flat end surface normal of the indenter and the pillar axis) [5].

### **2.2.2 Microstructural Characterization Using Synchrotron X-ray Microdiffraction**

The microstructure of as-fabricated and uniaxially compressed 920 nm diameter tin nanopillars was characterized by the  $\mu$ SXRD technique at the Beamline 12.3.2 at the Advanced Light Source Synchrotron facility of the Lawrence Berkeley National Laboratory. Conventional structural characterization methods, such as electron backscattered diffraction and transmission electron microscopy, were not employed since exposure of low-melting temperature metals to high energy electron beams can result in localized joule heating. This may lead to the activation of thermally assisted processes like dislocation climb, defect annihilations, and grain growth. The unique capability of this technique as a local nanoplasticity probe stems from the continuous range of wavelengths in a white X-ray beam.

This allows Bragg's law to be satisfied even when the lattice is locally rotated or bent, resulting in the observation of asymmetric broadening/streaking in the Laue diffraction peaks. Since geometrically necessary dislocations (GNDs) are directly related to the local lattice curvature, this technique can be used to determine the density of GNDs [52]. This has proven to be useful in the study of length scale effects involving uniaxially compressed submicron pillars of single-crystalline gold [53], nanoindented bulk copper single crystals [54], low melting temperature electroplated indium nanopillars [33], and nanoscale Cu/Nb single-crystalline multilayer materials [55]. The symmetric broadening of the Laue diffraction

peaks, in the mean time, is useful to provide an indication of the relative of statistically stored dislocations (SSDs) [56].

Samples were mounted on a precision XY Huber stage and the  $\mu$ SXRD Laue diffraction patterns were collected using a MAR133 X-ray charge-coupled device (CCD) detector and analyzed using the XMAS software package [52]. Once the array of pillars was located using the synchrotron X-ray microfluorescence scanning, fine diffraction scanning was performed on the nanopillars of interest. The results from the Laue diffraction peak provide microstructural information of the tin nanopillars, such as crystal orientations, stresses/strains, dislocation densities and configurations. A comparison of the dislocation densities and configurations of tin nanopillars before and after the compression test would elucidate the plasticity involved during the deformation.

### **2.2.3 Pillar Compression**

The compression tests were performed on a nanoindenter (NanoIndenter G200, Agilent Technologies Inc.) at the Nanomechanics Laboratory at the University of Waterloo. The indenter functioned at Dynamic Contact Mode (DCM) and was equipped with a custom-made diamond  $8\mu\text{m} \times 8\mu\text{m}$  flat punch indenter tip. All pillar sizes were compressed uniaxially, at 3 different nominal engineering strain rates:  $0.01 \text{ s}^{-1}$ ,  $0.001 \text{ s}^{-1}$ ,  $0.0001 \text{ s}^{-1}$ . This strain rate is defined by the ratio of the constant pillar length change over time (displacement rate) to the initial pillar height.

### 2.3 Results and Discussion

Figure 2.2 shows an SEM image of an array of the fabricated tin nanopillars with a diameter of ~920nm. This figure demonstrates the high production yield of these nanopillars fabricated using the presented technique.

To demonstrate the versatility of the nanoscale fabrication processes developed in this work, tin nanopillars with diameters between 70 and 920 nm were prepared and inspected using a SEM.

Each pillar was dimensioned after being imaged with a scanning electron microscope. Figure 2.3 (a-e) show representative micrographs of the solid and vertically oriented tin nanopillars with smooth side walls.

As fabricated, tin nanopillars with a diameter of 920 nm were characterized using the non-destructive  $\mu$ SXRD Laue diffraction technique. Smaller nanopillars were not tested due to the lack of reliable diffracted X-ray signals. Close up views of the (406) and (624) diffraction peaks taken from a Laue diffraction pattern obtained from a single as-fabricated tin nanopillar are shown in Figures 2.4 (a) and (b) respectively. For this tin nanopillar, only one unique Laue diffraction pattern (not shown) belonging to a body-centered tetragonal (BCT) crystal was identified for the entire nanopillar volume. This indicates that the tin structures produced for this work is likely single-crystalline. However, another possibility is that the specimen consists of a very large grain which occupies the majority of the nanopillar volume and remaining grains are too small to diffract enough incident X-ray signals for detection. In either case, it is clear that the mechanical response of such a small specimen would be dominated by dislocation activities in the single large tin crystal. From the Laue diffraction pattern, the tin nanopillar was indexed as a body-centered tetragonal (BCT) tin with nanopillar axis oriented almost along the  $\langle 110 \rangle$  crystal direction. It is important to note that only a very small fraction of fabricated nanopillars were investigated by the  $\mu$ SXRD technique, thus the analysis presented in Figure 2.4 does not necessarily apply to the ensemble of nanopillars. However, the results shown in Figure 2.4 are a good indication that it is likely the electroplating parameters employed that produce tin nanopillars consisting of large grains.

The two representative peaks in Figures 2.4 (a) and (b) are diffuse in nature, which is consistent with the small nanopillar dimensions. The geometry of the peaks is mostly circular which strongly indicates a well annealed tin crystal with no excess initial dislocations of the same signs, i.e. no GNDs. To quantify the Laue spot intensity profile, the tin nanopillar (406) peak was further analyzed along the intensity traces at a particular direction and along the  $2\theta$  axis, as illustrated in Figure 2.5 (a). The intensity profiles were fitted with Lorentzian curves as shown in Figure 2.5 (b). The full-width half-maximum (FWHM) measurement shows a peak broadening of  $0.439^\circ$  for the (406) Laue diffraction spot. This peak broadening consists of three contributions: crystal size effect, instrumentation, and the possibility of random dislocation storage during fabrication of the nanopillars, i.e. non-zero initial dislocation density.

### **2.3.1 Fabrication of Pillars**

Figures 2.6 (a) – (c) shows the representative engineering stress–strain curves obtained from uniaxial compression experiments of tin nanopillars with average diameters of 920 nm, 560 nm, and 350 nm respectively. These specimens were compressed with the same engineering strain rate of  $\sim 0.001 \text{ s}^{-1}$ . The stress – strain curves show that the nanopillars exhibit strain bursts or softening events after initial yielding. Such strain bursts are believed to be associated with sudden catastrophic shear failures along crystallographic slip planes.

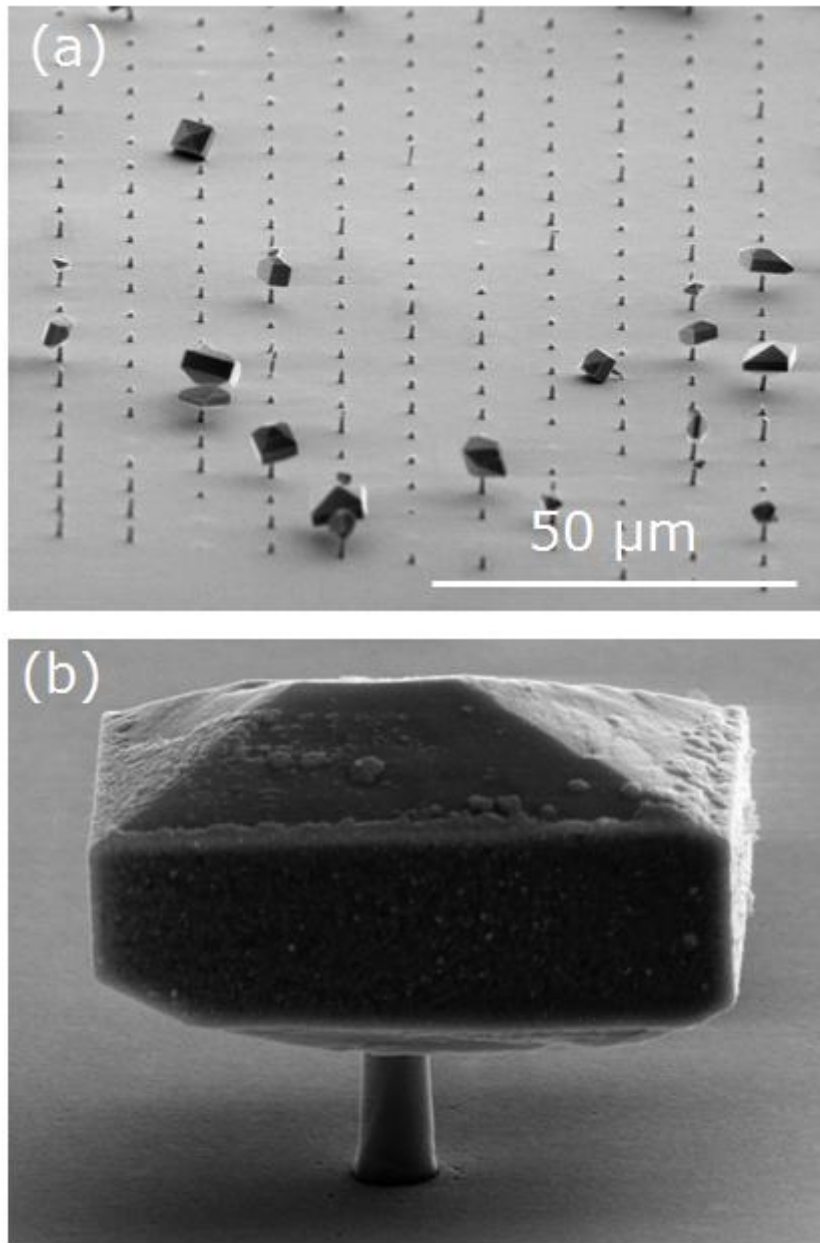


Figure 2.2: (a) SEM image of an array of ~950 nm diameter tin nanopillars showing characteristic disproportionate plating with many overplated specimens. (b) Close up SEM image of a typical overplated tin nanopillar

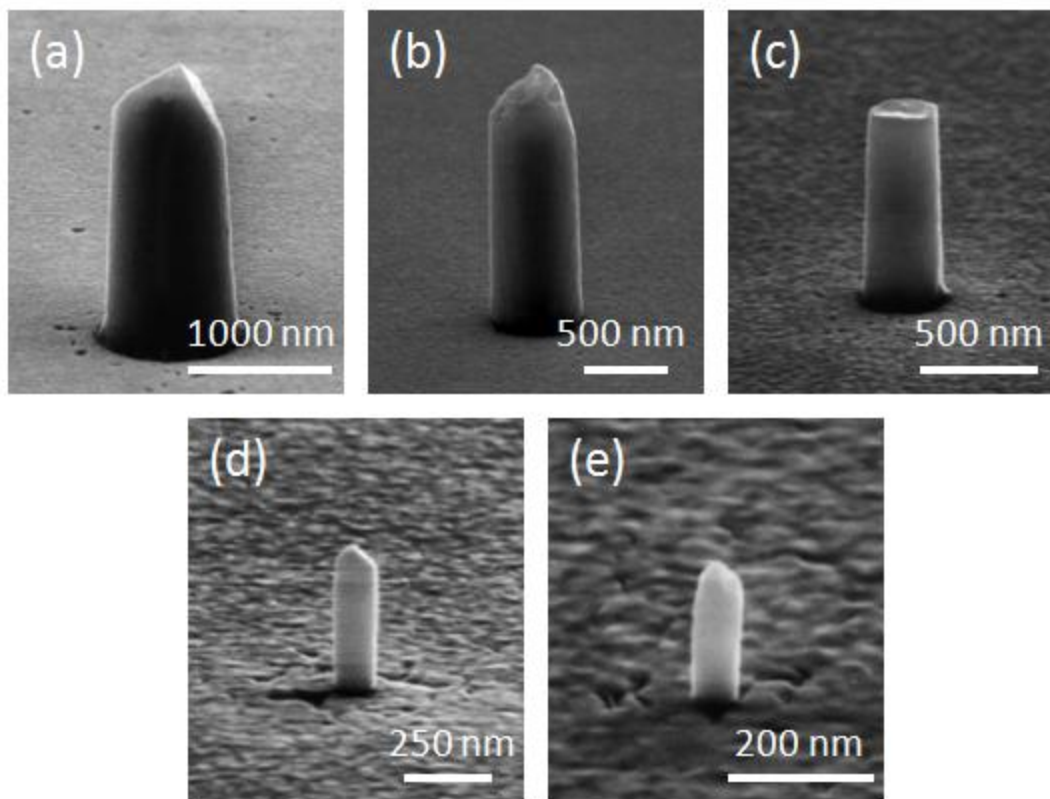


Figure 2.3: SEM images of as-fabricated tin nanopillars with diameters of (a) 920, (b) 590 nm, (c) 335 nm, (d) 130 nm, and (e) 70 nm. All SEM images taken at a 70° stage tilt

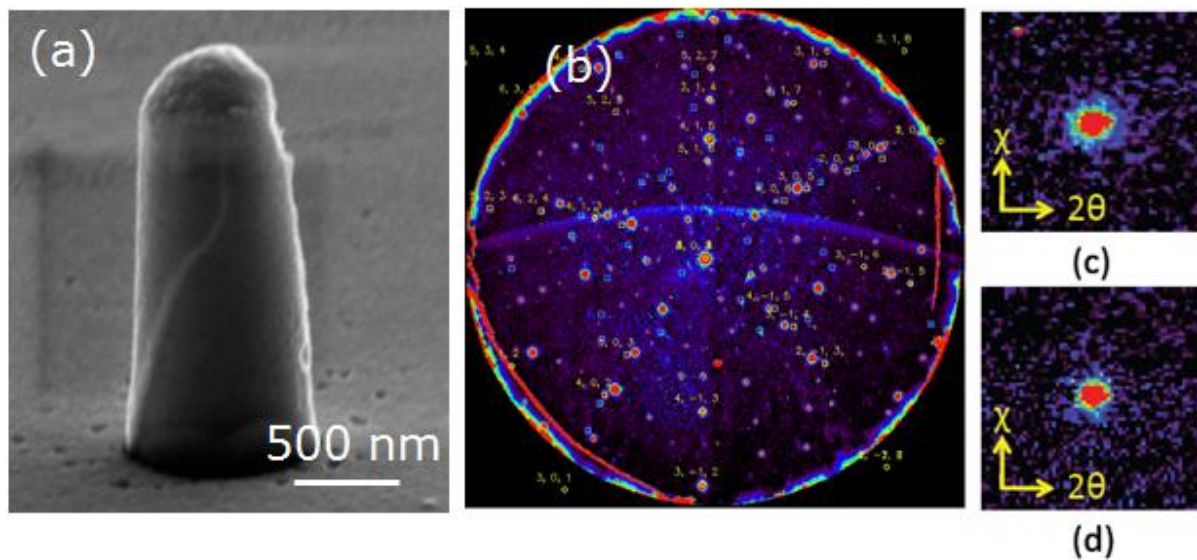


Figure 2.4: Representative quantitative  $\mu$ SXRD analysis of an uncompressed  $\sim 920$  nm diameter tin nanopillar. (a) SEM image of the tin nanopillar and (b) Laue diffraction pattern generated throughout the nanopillar volume (c) (406) Laue diffraction peak; (d) (624) Laue diffraction peak.

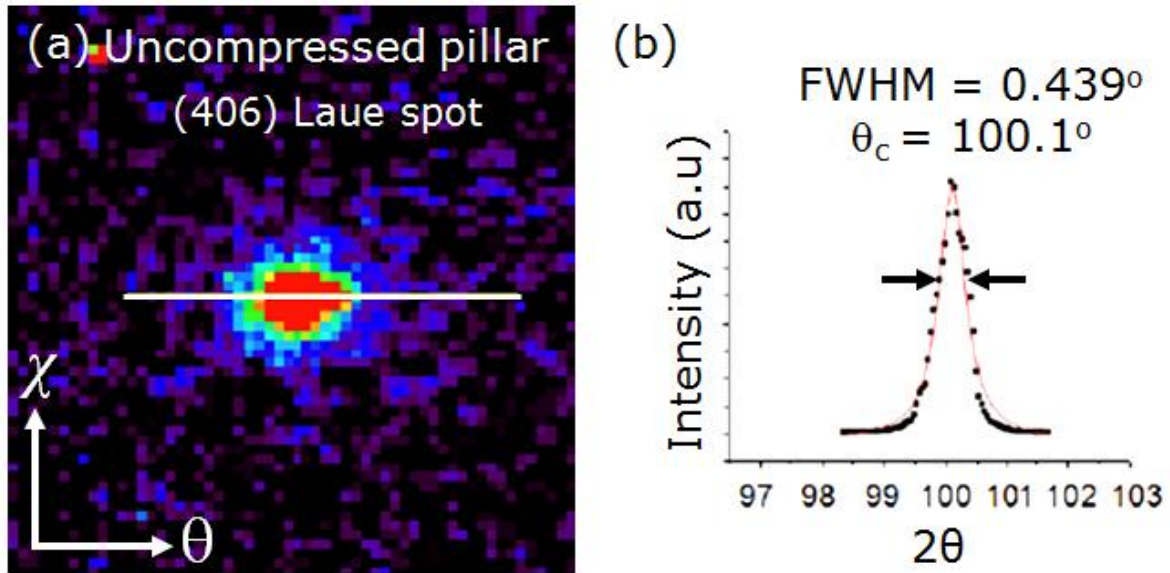


Figure 2.5: (a) The peak broadening due to crystal rotation of the (406) Laue diffraction spot . (b) This Laue spot has a FWHM of  $0.439^\circ$ . It was measured from the intensity line scan in (a).

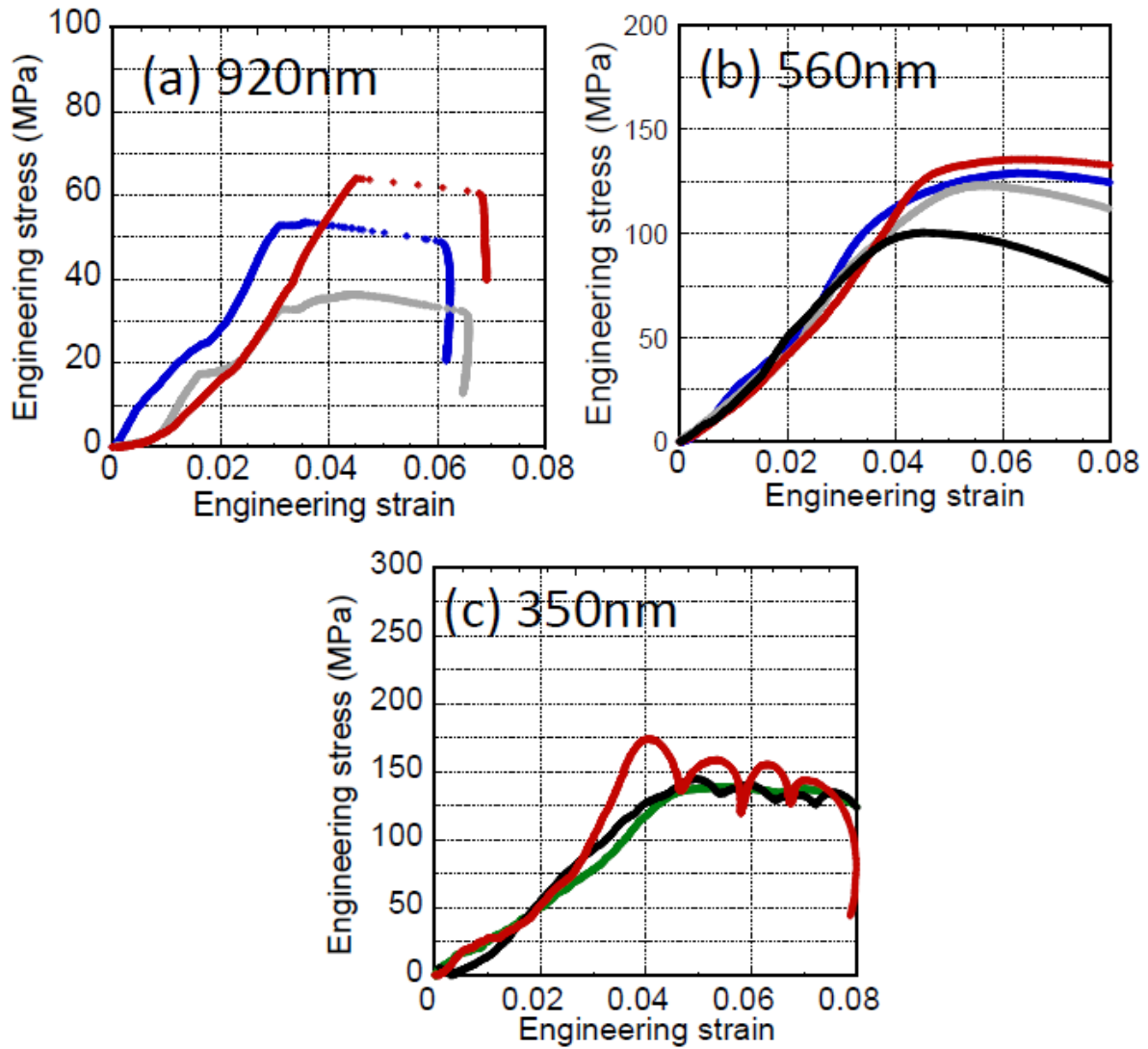


Figure 2.6: Representative engineering stress–strain curves for tin nanopillars with diameters of (a) 920nm, (b) 560nm, and (c) 350nm. All deformed with strain rate of  $\sim 0.001 \text{ s}^{-1}$ .

### 2.3.2 Post Compression Pillar Analysis

To further understand how small-scale tin structures behave plastically, all nanopillar specimens were carefully inspected before and after compression using high resolution SEM. Typical electron micrographs of tin nanopillars with diameters of  $\sim 920$  nm,  $\sim 560$  nm, and  $\sim 350$  nm before and after uniaxial compression at strain rate of  $\sim 0.001$  s<sup>-1</sup> are shown in Figures 2.7, 2.8, and 2.9, respectively. These figures show two distinct plastic flow features - crystallographic shear off-sets and material extrusion.

Both deformation features were observed for all three nanopillar sizes. Even though fine crystallographic slip lines are not apparent on the post compression images, examples of gross deformation by shear along crystallographic planes can be found in these SEM micrographs. This type of crystallographic shear behavior has been reported in almost all deformed single-crystalline metallic nanopillars ([11]-[20], [27]-[33]). Another deformation characteristic that can be found in Figures 2.7 to 2.9 is sidewall surface wrinkles and bulges perpendicular to the loading direction. All compressed tin nanopillars showed this type of plastic deformation where the compressive strain is compensated by material extrusions from the nanopillar sidewalls. The material extrusion type of deformation in tin nanopillars is not unexpected. At high homologous temperatures, a large number of slip systems will be activated which allows deformation in a greater number of crystallographic slip planes to occur simultaneously. The consequence is that fewer discrete slip planes are observed in the post-compression nanopillar, and instead strain resembles extrusion like deformation.

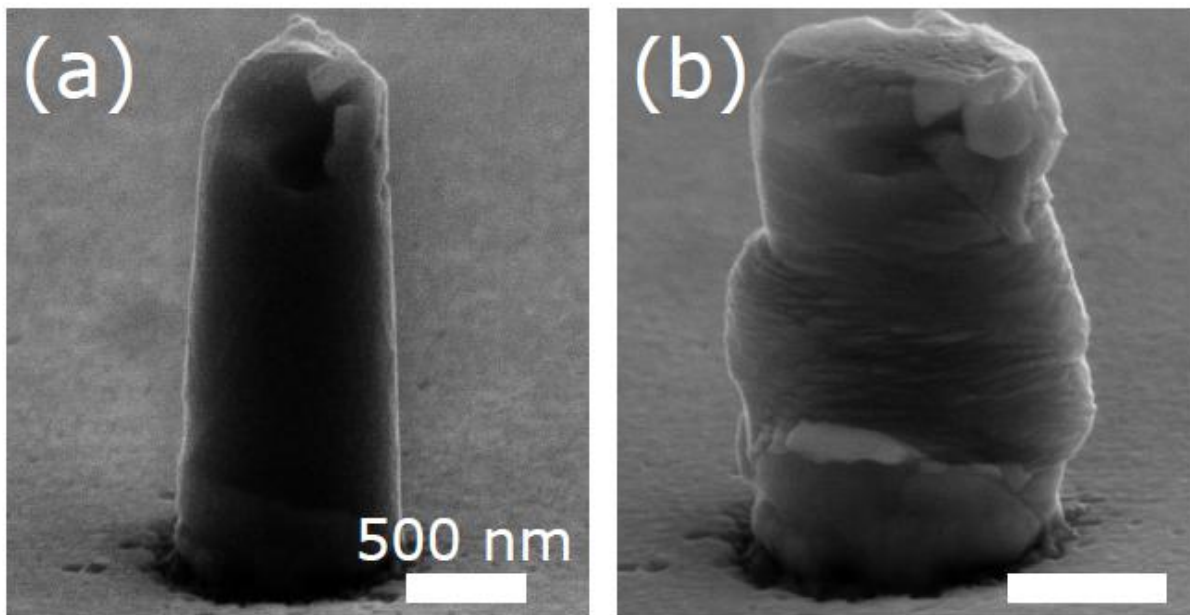


Figure 2.7: Pre and post compression SEM images of ~ 920 nm diameter tin nanopillars.

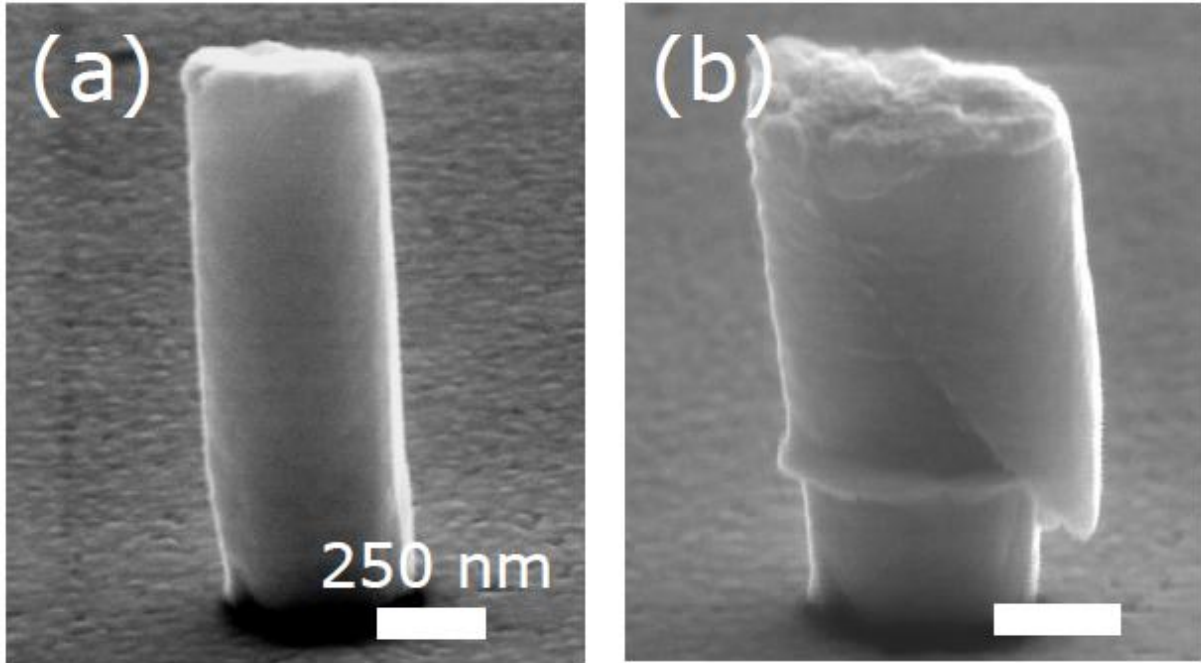


Figure 2.8: Pre and post compression SEM images of ~ 560 nm diameter tin nanopillars

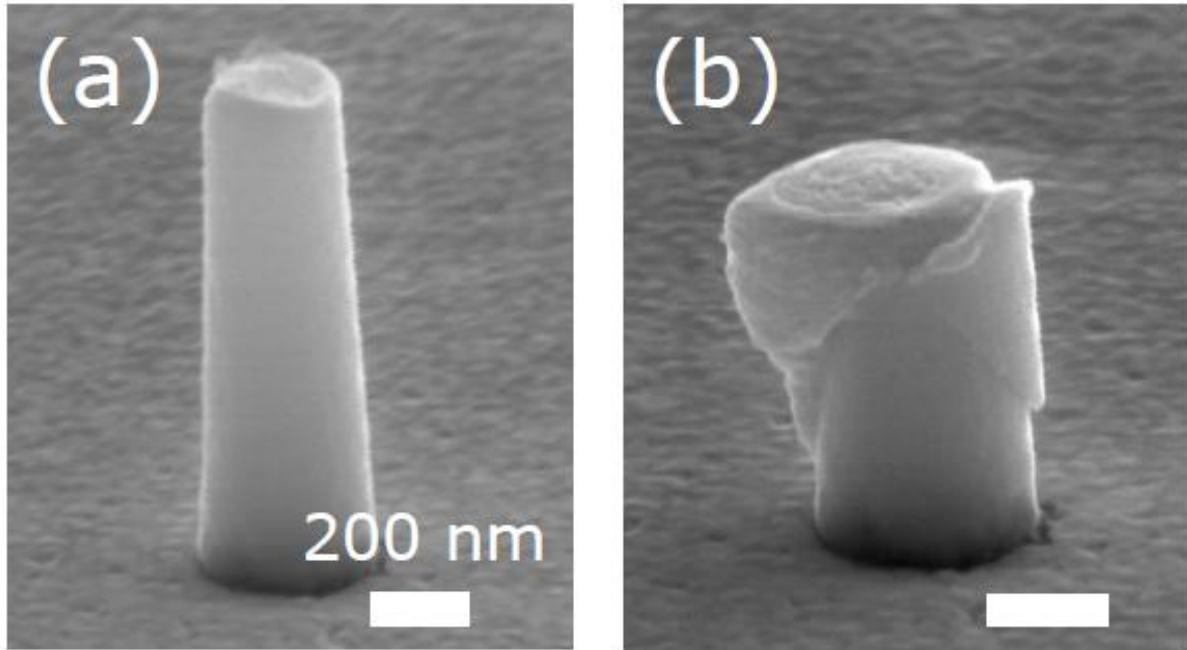


Figure 2.9: Pre and post compression SEM images of ~ 350 nm diameter tin nanopillars.

### 2.3.3 Strain Rate Sensitivity

Engineering flow stresses of tin nanopillars measured at 5.0 % nominal strain are plotted as a function of strain rate in Figure 2.10 (a). The data in this plot includes results from nanopillar compressions of three different diameters: 350 nm, 560 nm, and 920 nm. For the two largest nanopillar sizes of 560 nm and 920 nm, the results clearly show that the tin flow stresses are sensitive to the deformation rate. The data reveals that the material strength is low when the structure is deformed slowly. In contrast, the yield strength increases when the specimen is compressed at a fast strain rate. In order to show a clear trend of strain rate sensitivity, the average flow stress values of 560 nm and 920 nm diameter nanopillars are plotted in Figure 2.10 (b), where the error bars correspond to one standard deviation. Figure 2.10 (b) shows a noticeable increase in 920 nm diameter tin nanopillar strength from ~ 46 to 112 MPa when the strain rate increases from 0.0001 s<sup>-1</sup> to 0.01 s<sup>-1</sup>. Similarly, for the 560 nm diameter tin nanopillars, the data shows an increase from ~ 61 to 96 MPa for the same increase in strain rate.

The general relationship between the uniaxial strain rate and creep stress has been well documented and is displayed in Eq. (2.1). To compare the tin nanopillar strain rate sensitivity with the bulk samples from the previous studies, the data from Figure 2.10 (b) were fitted with Eq. (2.1). The stress exponent extracted from this curve fit is approximately 5.54 +/- 1.53, where the spread corresponds to one standard deviation. This value agrees with the single -crystal impression creep results reported from Chu and Li [42], with exponent values measured near room temperatures in the range of 4.4 to 5.0. The results indicate that the strain rate sensitivity of single-crystal tin nanostructures is similar to bulk.

Figure 2.11 shows the tin nanopillar engineering flow stress results measured at 5.0 % nominal strain plotted as a function of feature size. These structures were compressed at a constant strain rate of ~ 0.001 s<sup>-1</sup>. The figure also includes the average values from each nanopillar size where the error bars correspond to one standard deviation. The attained stresses at ~ 5.0 % engineering strain are approximately 72.8 +/- 36.3 MPa, 96.4 +/- 33.9 MPa, 131.5 +/- 39.1 MPa for 920 nm, 560 nm, and 350 nm diameter tin nanopillars respectively. As shown in Figure 11, tin nanopillars exhibit a size effect where reducing the

sample dimension produces stronger specimens. Since the nanopillars tested in this work were electroplated, rather than fabricated using standard focused ion beam (FIB) milling techniques, arguments of ion beam damage to the nanopillar cannot account for the increase in strength for small tin nanopillars. Similar size-dependent strengthening has been reported previously for metallic nanopillars fabricated in Ni ([11]-[14], Au ([15]-[20]), Cu ([21]-[24]), Mo ([4],[19],[25]-[29]). In A recent review by Uchic *et al.* [2] on the small-scale mechanical properties of metals, it was illustrated that single-crystalline metallic nanopillar specimens which exhibit yield strength size effects follow an empirical power-law relationship between the strength of the sample ( $\sigma$ ) and the nanopillar diameter ( $D$ ):

$$\sigma \propto D^{-\gamma} \quad (2.2)$$

The parameter  $\gamma$  is the power-law exponent. In their work, Uchic *et al.* showed that most size dependent strengthening data for nanoscale FCC single-crystalline metals, such as Ni, Au, Cu, and Al, could be collapsed onto a single line by plotting the normalized resolved shear effective stress versus pillar diameter [2]. The result of this normalization showed that a power-law exponent of  $\sim 0.6$  was seen for most FCC metals. Recently, the small-scale mechanical properties of body centered cubic (BCC) metals have also been explored in uniaxial compression and tension ([18]-[19],[26],[31],[28]-[29],[57]). It is interesting to note that the deformation characteristics and size effects observed for single-crystalline BCC nanopillars deviate from FCC specimens for reasons attributed to crystal structure ([18], [57]). For example, Kim *et al.* [27] showed that BCC tungsten, molybdenum, tantalum, and niobium have size effect power law exponents of -0.44, -0.44, -0.43, and -0.93 respectively, and Han *et al.* showed BCC vanadium has a size effect power law exponents of -0.79 [32]. These values are quite different from the FCC results summarized by Uchic *et al.*[2]. To compare the size dependence of BCT tin structure with the FCC and BCC specimens, flow stress data from Figure 2.11 were fitted with Eq. (2.2) and an exponent value of -0.572 +/- 0.114 was obtained, a value very close to the FCC power exponent of -0.6 observed by Uchic but not the BCC values. This suggests that even though tin has a different crystal structure (BCT versus FCC) the small-scale mechanical properties of BCT tin may operate by a similar size-dependent mechanism to FCC metals. One of the possible explanations of the similarity may be due

to the low melting temperature of tin at  $\sim 232$  °C. During deformation in ambient conditions, a greater number of slip systems are thermally activated in metals with low melting temperatures. According to a recent review on tin deformation mechanisms by Yang and Li [41], there can be as many as 12 possible activated slip systems in a tin crystal, which is similar to FCC crystals. In addition, it has been well documented that the BCT tin critical resolve shear stresses (CRSS) are very sensitive to temperatures. For example, Nagasaka [58] report that the CRSS of the tin (100)[010] slip system decreases nearly exponentially in the temperature range of 200 K to 320 K, with the CRSS values reduced from approximately 0.7 MPa to 0.2 MPa. The CRSS values for other tin slip systems, such as the  $(\bar{1}\bar{1}\bar{1})1/2[111]$  system, also exhibits near exponential temperature sensitivity. It requires roughly 4.6 MPa to shear this plane and direction at 200 K, but only 1 MPa near 320 K. The significant reduction of the CRSS values at room temperature in conjunction with the large number of thermally activated glide planes available for dislocation motion may also explain why the nanoscale deformation behaviour of BCT tin is similar to other FCC metals at nanoscale.

In addition to the low melting temperature of tin, a detailed inspection of a BCT tin unit cell reveals that it has a close resemblance of a FCC diamond structure [59]. In addition to the one atom at the center and eight atoms at the corners of the tin unit cell, there are four other atoms on four different faces. Therefore, a BCT tin unit cell contains four atoms with each atom having four nearest neighbours and can be interpreted as a distorted diamond cubic structure [59]. Therefore, the similarity between the strength size effect in BCT tin and FCC metals at the nanoscale is not unreasonable.

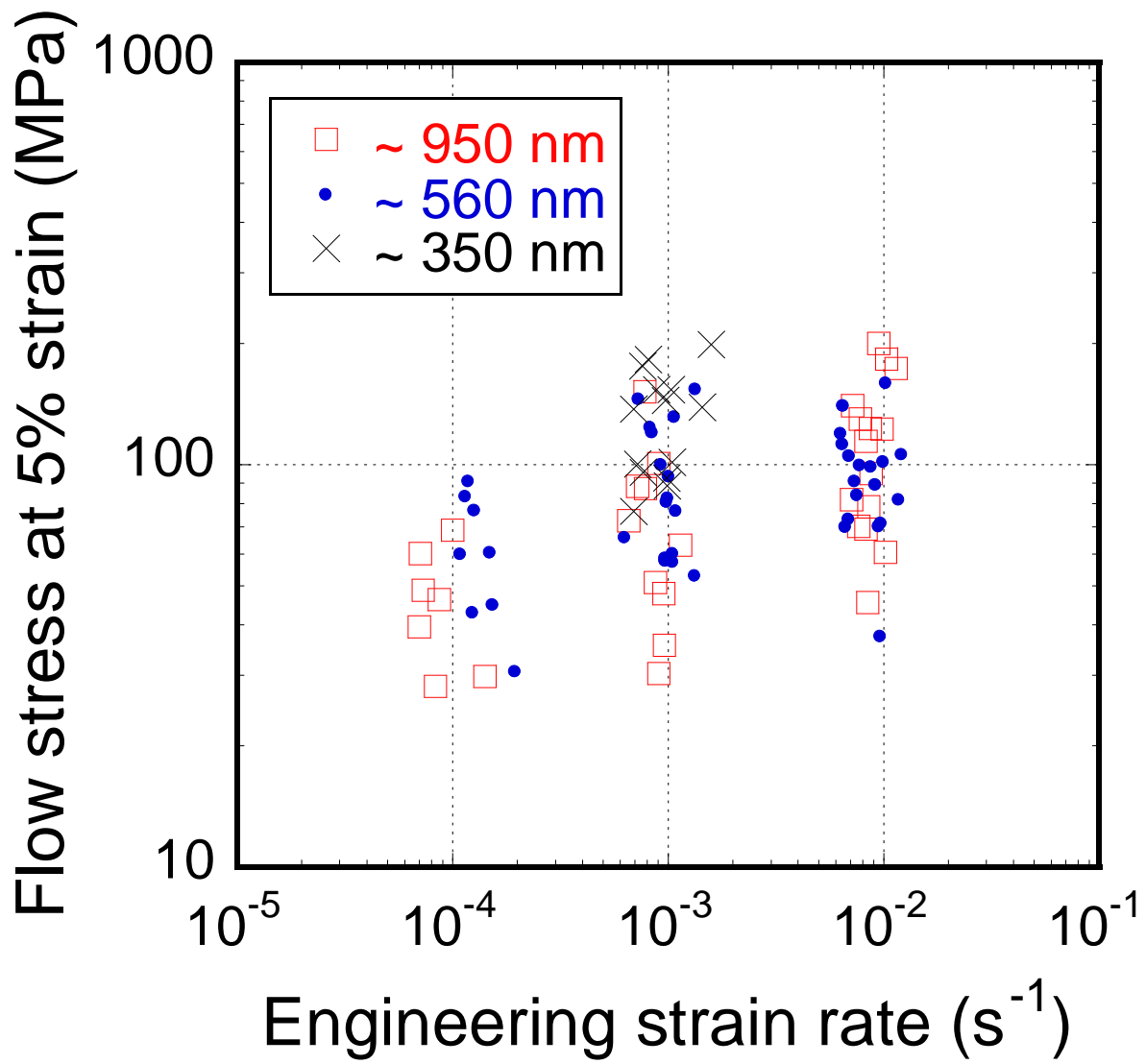


Figure 2.10: (a) Log – log plot of engineering flow stress measured at ~5% strain as a function of engineering strain rate for all tin nanopillars tested in this work.

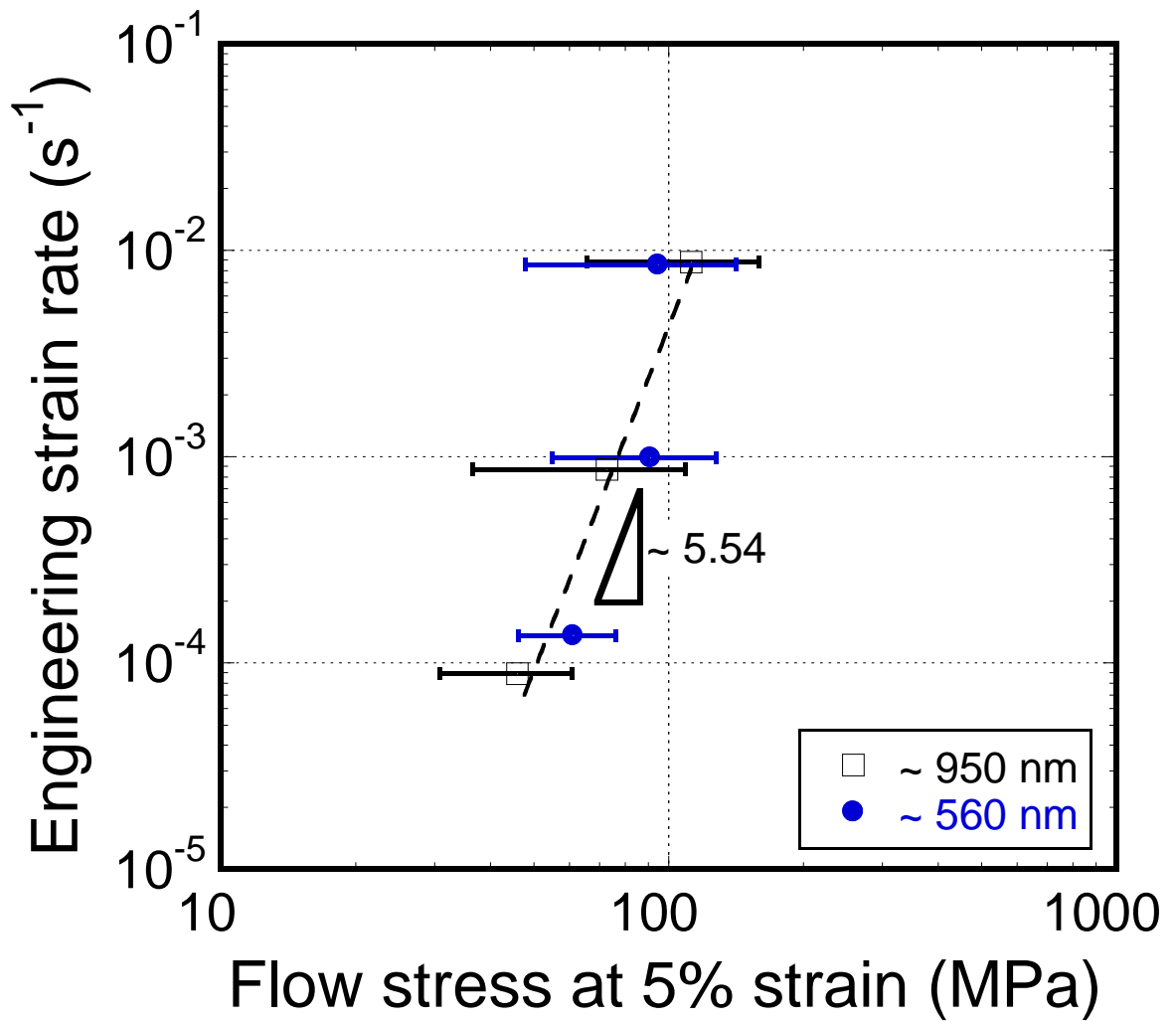
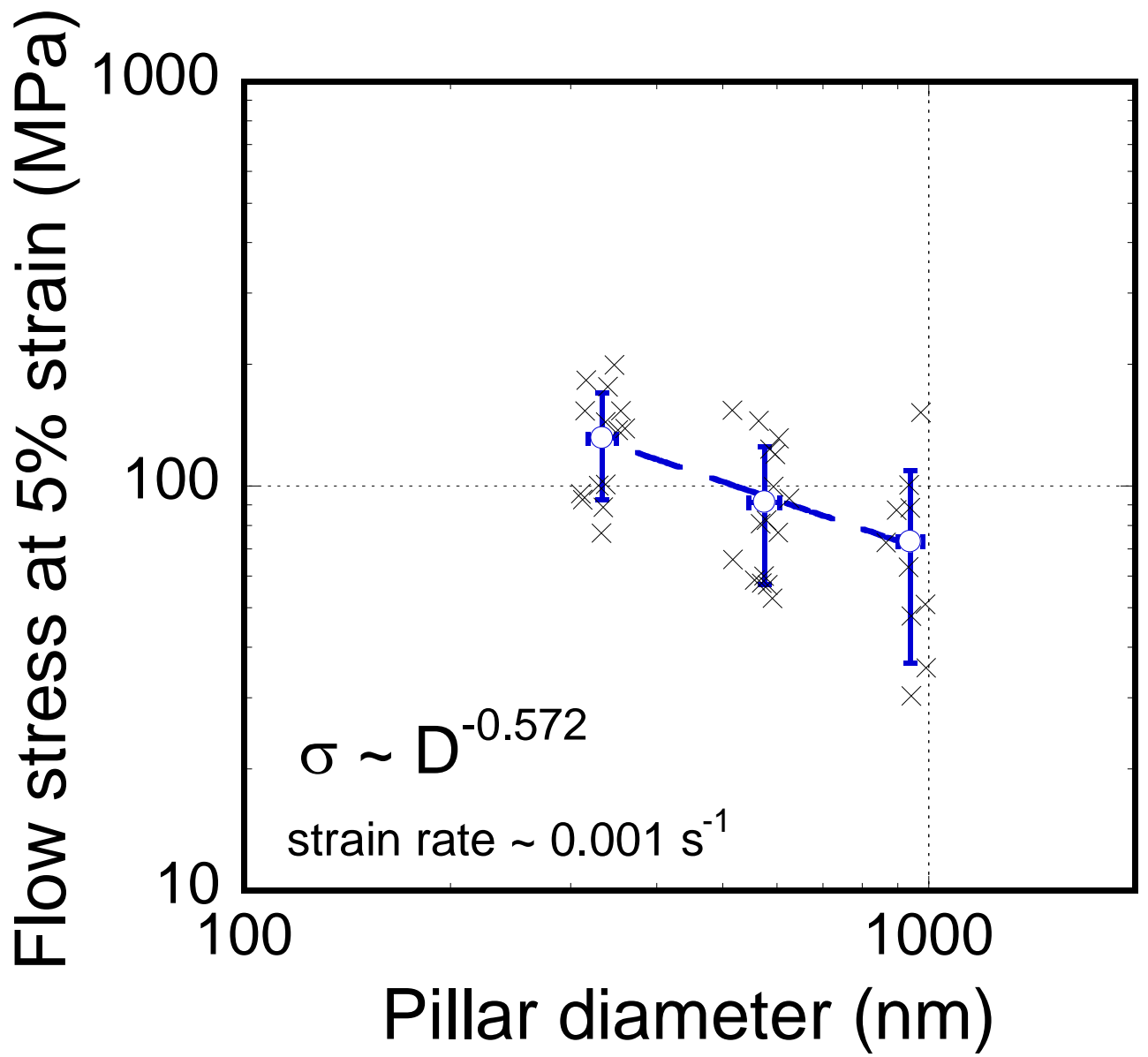


Figure 2.10 (b): Log – log plot of engineering flow stress measured at ~5% strain as a function of engineering strain rate for all tin nanopillars tested in this work.



### 2.3.4 $\mu$ SXRD Study of Deformed Tin Nanopillars

To understand the tin nanopillar deformation mechanisms in greater details,  $\mu$ SXRD techniques were used to characterize their microstructures and dislocation density after deformation. Figures 2.12 (a) and (b) show SEM micrographs of a tin nanopillar before and after compression to approximately 22.0 % engineering strain respectively. The strain rate used to compress this specimen was  $\sim 0.001 \text{ s}^{-1}$ . Crystallographic shear off-sets and lateral surface wrinkling/extrusion are both observed in the post compression SEM image. This is consistent with the deformation mechanisms observations in Figures 2.7, 2.8, and 2.9. The stress–strain data collected from uniaxial compression of this tin nanopillar is plotted in Figure 2.12 (c). The stress – strain behavior includes similar strain bursts to those illustrated previously in Figure 2.6. It is important to note that this particular pillar was only characterized by  $\mu$ SXRD after the compression test. No information was collected in the as-fabricated state. The  $\mu$ SXRD analysis of the deformed tin nanopillar again identified only one unique body-centered tetragonal (BCT) Laue diffraction pattern for the entire nanopillar volume, indicating the compressed nanopillar is single-crystalline. The Laue diffraction pattern indicates the compressed tin nanopillar is BCT with the plane normal to the vertical axis of the pillar close to the tin (204) plane. Two individual Laue diffraction spots of (204) and (105) were extracted from this pattern and plotted in Figures 2.12 (a) and (b), respectively. The shapes of these two Laue spots are fairly regular with circular geometry suggesting random distribution of dislocations due to the nanopillar deformation. Qualitatively, the Laue diffraction peaks of this deformed specimen are similar to the as-fabricated tin nanopillar shown in Figure 2.4 (a) and (b). Qualitative analysis of the (204) Laue diffraction peak in Figure 2.13 (a) were also conducted along the intensity traces at a particular  $\chi$  and along the  $2\theta$  axis. This profile was fitted with Lorentzian curves as shown in Figure 2.13 (c). The FWHM value of this peak broadening is approximately  $0.458^\circ$  for the compressed tin nanopillar. When compared with the peak broadening between as-fabricated and post compression spots shown in Figures 2.13(b) and 2.13 (c), the results show that there is an angular width difference of  $\sim 0.019^\circ$ . This variation is within the experimental error and resolution of the  $\mu$ SXRD

technique. The angular resolution in the  $\mu$ SXRD experiments is limited by the charge-coupled device (CCD) camera pixel size which translates to resolution limit of  $\sim 0.03^\circ$  in the Laue spot width measurement. No significant change in the peak broadening is expected here from the small crystal size, as well as the instrumentation from before to after the deformation. It is then also reasonable to propose that there is no significant change in the peak broadening due to random dislocation density associated with the nanopillar deformation. The Laue diffraction results discussed here suggest that the defect density in this tin nanopillar after compression is very similar to the as-fabricated tin nanopillar described in Figure 4. This may indicate that the nucleation and multiplication rates of dislocations during the uniaxial compression process are offset by the dislocation annihilation rate at the nanopillar surface. There is no significant increase or accumulation of dislocations in these small tin structures. Such a finding is similar to that reported earlier by Budiman et al. [53] in an ex-situ study of single crystalline gold nanopillars fabricated from by FIB milling, despite different crystal structures.

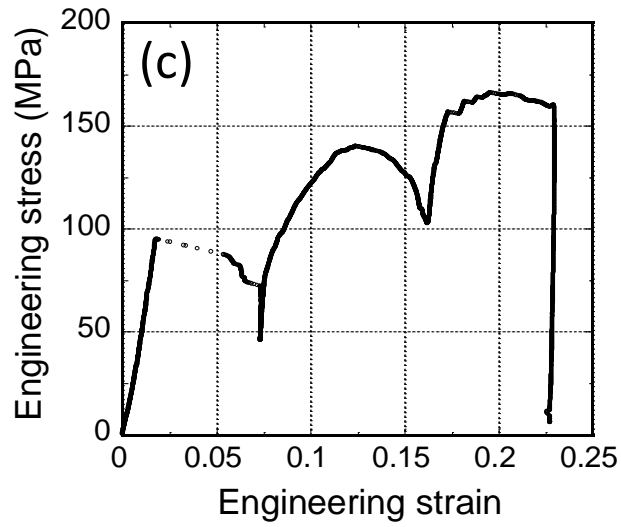
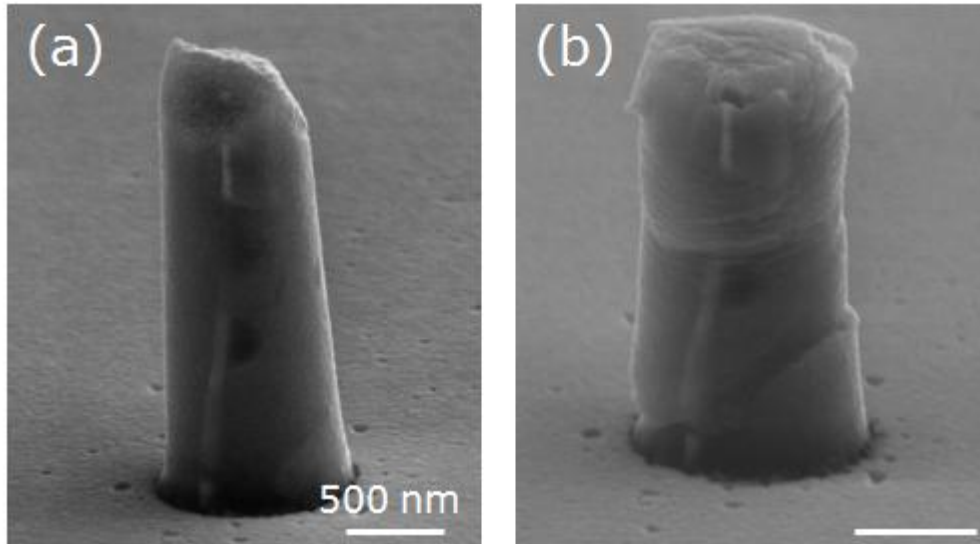


Figure 2.12: Representative quantitative  $\mu$ SXRD analysis of a  $\sim 950$  nm diameter tin nanopillar after uniaxial compression to  $\sim 22$  % engineering strain. Pre and post compression SEM images of the tin nanopillar are shown in (a) and (b) respectively, with the corresponding engineering stress – strain curve displayed in (c).

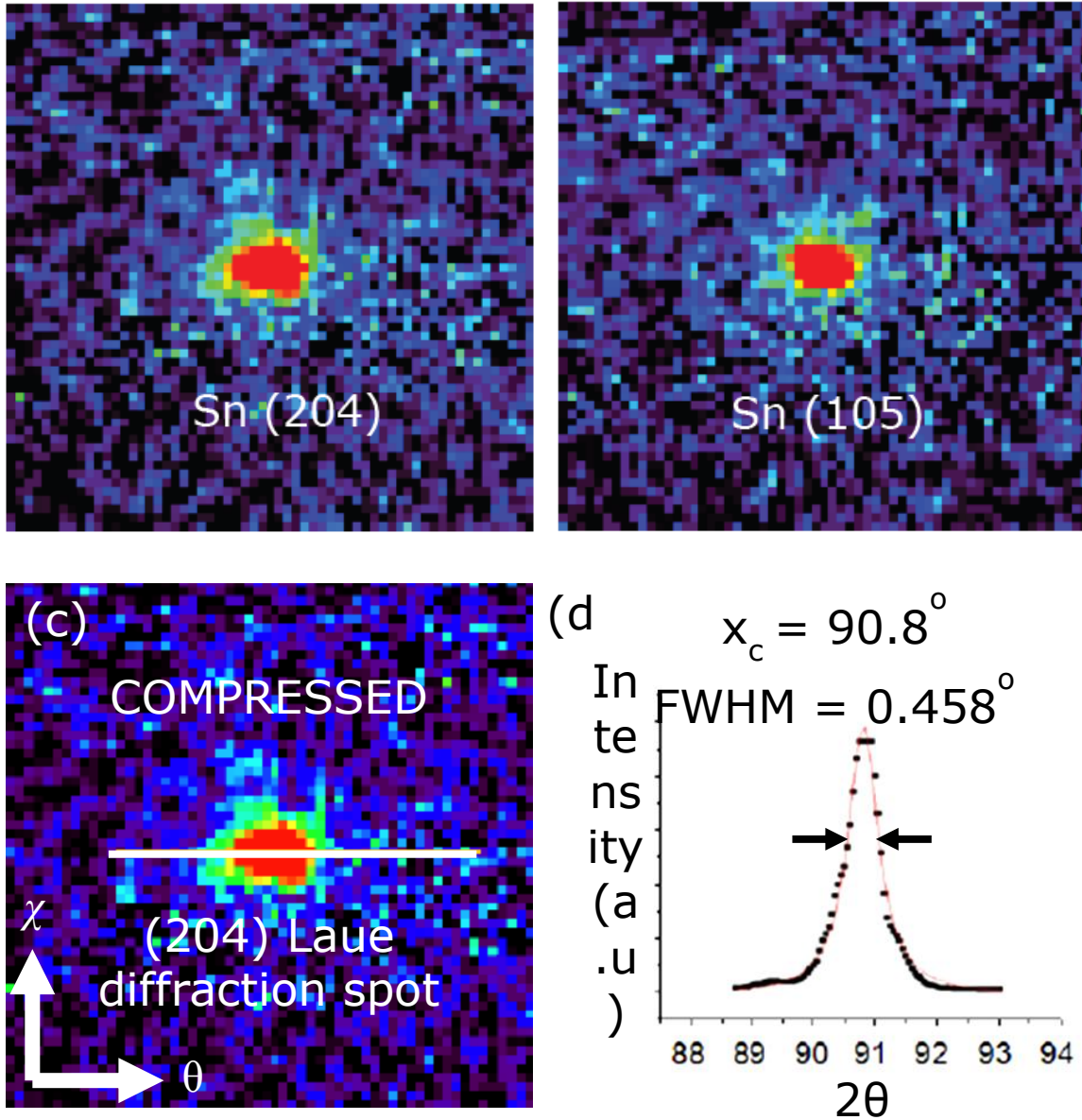


Figure 2.13: Representative quantitative  $\mu$ SXR analysis of a  $\sim 920$  nm diameter tin nanopillar after uniaxial compression to  $\sim 22\%$  engineering strain. Laue diffraction spots of (204) and (105) are shown in (a) and (b) respectively. The axes used for intensity measurements are illustrated in (c). The peak intensity of the (204) Laue diffraction spot (d) yields a FWHM of  $0.458^\circ$ .

## 2.4 Conclusions and Recommendations

In this chapter, the fabrication and integration techniques for the production of BCT tin nanopillars was presented. Pillars with diameters less than 100nm were successfully fabricated and tested. The studies on strain rate sensitivity and flow stress showed that tin nanopillars have a size effect similar to all other single crystal FCC metals that are studied under micro-compression. Finally, a non-destructive  $\mu$ SXRD microstructural characterization on a compressed pillar showed no drastic increase in dislocations. This suggests that the dislocation annihilation at the surface of the pillar dominates the rate of dislocation generation or multiplication within the pillar.

More than 300 tin nanopillars compressed in this work and the results show a wide scatter in the values of the flow stresses. This could be attributed to the different deformation mechanisms during compression and different initial pillar micro-structures (e.g. dislocation densities). Micro-structural characterization of all these pillars before and after compression tests would result in a more thorough understanding of the plastic deformation of this material in nanoscale.

## Chapter 3: Polycrystalline Bismuth Nanostructures

### 3.1 Background on Bi applications and Mechanical Properties

In this chapter, the mechanical properties of cylindrical bismuth pillars with nanoscale diameters and polycrystalline microstructures are presented.

The mechanical properties of bismuth have yet to be studied at the nanoscale. Due to its low melting temperature ( $\sim 272$  °C), bismuth and its alloys are particularly relevant as lead-free solders in the microelectronics industry ([60]-[62]). Since solders are typically part of load bearing structures in microelectronic packaging [60], the functionality and lifetime of such components are often associated with their mechanical reliability.

Bismuth is particularly interesting at the nanoscale due to its unique electronic properties which can vary between metallic, semimetallic, and semiconducting depending on sample size, geometry, and microstructure [63]. Therefore, knowledge of nanoscale bismuth deformation characteristics will play an important role in the future design of reliable bismuth-based lead-free solders and nanoelectronic devices.

Bismuth has a rhombohedra crystal structure and its space group is classified as  $R\bar{3}m$  with  $a = 4.736$  Å, and  $\alpha = 57^\circ 14'$  [64]. The shear modulus of this material is approximately 12.8 GPa [65]. In bulk, bismuth is relatively brittle when compared with other low melting temperature materials, such as indium, tin, and lead. In fact, it has been documented that bulk bismuth single-crystals cleave under uniaxial tensile stress along (111) or  $(11\bar{1})$  crystallographic planes [66]. The bulk-scale mechanical properties of bismuth specimens have been previously characterized in uniaxial compression ([67]-[68]). Das and Bever [67] performed compression tests on polycrystalline bismuth columns 9.5 mm long by 5 mm in diameter at strain rates of  $2.2 \times 10^{-2} \text{ s}^{-1}$ ,  $2.2 \times 10^{-3} \text{ s}^{-1}$ , and  $2.2 \times 10^{-4} \text{ s}^{-1}$ . These specimens contain grains with a cross-sectional area of approximately  $0.35 \text{ mm}^2$  per grain. It was demonstrated that flow stresses of bulk polycrystalline bismuth increase with the deformation rate at room temperatures. A wide range of steady

state high temperature ( $>0.5T_m$ ) creep results from polycrystalline metals have demonstrated that a general relationship exists between the strain rate ( $\dot{\epsilon}$ ) and creep stress ( $\sigma$ ):

$$\dot{\epsilon} = K\sigma^n \quad (3.1)$$

where  $K$  is a material constant that depends on diffusivity and elastic modulus [69]. The degree of strain rate sensitivity is commonly characterized by the stress exponent,  $n$ . By fitting the flow stress values (measured at  $\sim 5.0\%$  strain) reported by Das and Bever [67] for various strain rates with Eq. (3.1), the bulk polycrystalline bismuth stress exponent in ambient conditions was determined to have a value of 9.88. Otake et al. [68] evaluated the mechanical behaviors of bulk bismuth single-crystals under uniaxial compression. These samples were deformed with strain rates of  $8.5 \times 10^{-5} \text{ s}^{-1}$  and  $8.5 \times 10^{-4} \text{ s}^{-1}$ . They measured the critically resolved shear stress (CRSS) of bismuth single-crystals along two slip systems,  $(111)[\bar{1}\bar{1}0]$  and  $(001)[\bar{1}\bar{1}0]$ , over the temperature range of 77 to 538 K. The  $(111)[\bar{1}\bar{1}0]$  system is the primary slip system of bismuth at room temperature. In contrast with bulk polycrystalline bismuth, Otake et al. (68) showed that the CRSS of the two slip systems tested are strain rate sensitive only when the testing temperatures are below the critical temperature defined by Seeger's theorem [70]. Above this critical temperature, the strength of single-crystalline bismuth does not exhibit deformation rate sensitivity. For the slip systems  $(111)[\bar{1}\bar{1}0]$  and  $(001)[\bar{1}\bar{1}0]$ , the critical temperatures extracted from their results, are approximately 300 K and 460 K respectively. This indicates that the bismuth primary slip system is not expected to exhibit pronounced strain rate sensitivity in ambient conditions.

The electroplating solution chemistry and deposition parameters selected for this work generate a polycrystalline bismuth deposit with a wide distribution of grain sizes ranging from 0.1  $\mu\text{m}$  to 1  $\mu\text{m}$ .

Given the overlap between this distribution and the range of nanopillar diameters fabricated, the influence of feature size and grain size on the mechanical properties of nanoscale metals was observed.

The grain size produced by the electroplating process is independent of the nanopillar size. As such, the number of grains and the volume fraction of the grain boundaries within a bismuth nanopillar decreases as the nanopillar diameter decreases. Consequently, larger bismuth nanopillars produced in this work are

completely polycrystalline in nature, while the smaller nanopillars have microstructures approaching a single-crystalline state. Uniaxial compression results show that large bismuth nanopillars exhibit strain rate sensitivities and flow stresses that closely matches bulk polycrystalline bismuth nanopillars [67]. On the other hand, smaller bismuth nanopillars are significantly less sensitive to the deformation rate, a mechanical behavior characteristic of bulk bismuth single-crystals [68], yet display remarkably high strengths.

## 3.2 Experimental Methods

### 3.2.1 Pillar Fabrication

Similar to the tin nanostructures, bismuth nanopillars were fabricated with an electron beam lithography and electroplating method shown in Figure 2.1. Prepared nanopillars with diameters ranging from 130 nm to 1100 nm were subsequently characterized by uniaxial compression in a nanoindenter outfitted with a flat diamond tip. The strain rate sensitivity of these bismuth nanostructures was investigated by performing compressions at three different deformation rates:  $10^{-2} \text{ s}^{-1}$ ,  $10^{-3} \text{ s}^{-1}$ , and  $10^{-4} \text{ s}^{-1}$ .

Prior to bismuth electroplating, the patterned PMMA coated substrates underwent a 15 second O<sub>2</sub> plasma descum process using a reactive ion etcher (RIE) system at the Center for Integrated RF Engineering (CIRFE) lab at the University of Waterloo. The RIE operated at room temperature with a chamber pressure of 102 mTorr, plasma power of 20 W, and O<sub>2</sub> flow rate at 40 sccm. The nanopillar yield was significantly improved due to this process since the O<sub>2</sub> plasma descum removed residue or contaminants that may have remained in the exposed PMMA features. However, the O<sub>2</sub> plasma was not performed for the smallest exposed features in order to avoid excessive widening of the final nanopillar diameter. The O<sub>2</sub> plasma process was observed to have a negligible effect on the actual mechanical properties of bismuth nanopillar. The prepared wafer was diced into square 1 x 1 cm<sup>2</sup> chips with the patterned PMMA resist template in the chip center before electroplating.

Electroplating was used to deposit polycrystalline bismuth into the patterned PMMA resist template. The electroplating solution contained 1.3 M hydrochloric acid, 1.1 M glycerol (ultrapure HPLC grade, Alfa

Aesar), 0.3 M tartaric acid (99 % purity, Alfa Aesar), 0.2 M sodium chloride, and 0.2 M bismuth trichloride ( $\text{BiCl}_3$ , 98 % purity, Alfa Aesar). This solution was prepared one hour prior to use and was maintained at  $40^\circ\text{C}$  with constant mechanical agitation throughout the deposition process. The gold/titanium seed layer underneath the PMMA resist template acted as the cathode and an 11 mm diameter bismuth rod (99.99% purity, Alfa Aesar) was used as a soluble anode. Prior to each deposition, the bismuth rod was mechanically polished to remove surface contaminants and the native oxide layer. A Teflon backing and custom gold coated brass clips were used to mount the PMMA coated substrates in the solution and electrically interface with the gold/titanium cathode layer. Both electrodes were submerged 3 cm into the plating solution and separated by 3 cm from each other. The total cathode area, which included the patterned PMMA coated substrate, a blank  $1\text{ cm}^2$  gold/titanium coated silicon wafer chip, and the gold clips was maintained at approximately  $3.5\text{ cm}^2$ . For the electroplating process, a constant current density value of  $7.5\text{ mA/cm}^2$  was maintained. The target aspect ratio (height/diameter) was 4:1 and the deposition time was adjusted according to the desired nanopillar height. After electroplating, the PMMA resist was removed with acetone. All of the specimens were annealed in ambient conditions, corresponding to a homologous temperature of 0.55, for at least seven days prior to microstructure characterization and mechanical testing. This annealing period allows reduction of fabrication induced defects and grain growth to reach a steady state. Five different bismuth cylindrical structures with average diameters of approximately 130 nm, 230 nm, 540 nm, 840 nm, and 1100 nm were successfully fabricated.

### 3.2.2 Pillar Compression

The uniaxial compression tests of bismuth nanopillars were performed using an *in-situ* nanoindenter (Nanomechanics Inc, Knoxville, TN, USA) equipped with a custom diamond flat punch tip with a diameter of  $8\text{ }\mu\text{m}$ . To investigate the strain rate sensitivity of these bismuth nanostructures, three different target deformation rates were used:  $10^{-2}\text{ s}^{-1}$ ,  $10^{-3}\text{ s}^{-1}$ , and  $10^{-4}\text{ s}^{-1}$ . The strain rate was defined by the ratio between the constant prescribed displacement rate and the initial height of the nanopillar being tested.

### 3.3 Results and Discussion

Representative scanning electron microscopy (SEM) images of as-fabricated bismuth nanopillars with diameters ranging from 130 to 1100 nm are shown in Figures 3.1 (a) - (e). Figure 3.1 (a) reveals an image of an 1100 nm diameter specimen which clearly shows the polycrystalline nature of the electrodeposited bismuth. The grain boundaries are visible, as well as small voids on the nanopillar surface. From SEM analysis, the grain size appears to be well distributed from roughly 100 nm to grains on the same order as the nanopillar diameter (i.e. near 1  $\mu\text{m}$ ). The average grain size measured from SEM images of ten different 1100 nm diameter specimens was  $280.5 \pm 55.7$  nm. Figure 3.1 (b) shows a smaller nanopillar with diameter of 840 nm. Again, grain boundaries are visible on the sidewalls of this nanopillar.

However, the number of grains included in this specimen is less than the nanopillar shown in Figure 3.1 (a) which illustrates that the total number of grains which can be accommodated within a nanopillar reduces with size and the sidewalls of smaller nanopillars become progressively smoother as illustrated in Figure 3.1 (c) – (e).

Beyond SEM analysis, the microstructure of the 1100 nm diameter bismuth nanopillars were also characterized by using transmission electron microscopy (TEM). Individual bismuth nanopillars were sectioned and polished by using the focused ion beam (FIB) milling method [71]. The thinned bismuth nanopillar foils were then transferred to a TEM lift-out grid via Omniprobe nanomanipulator. Figures 3.2 (a) and 3.2 (b) reveal the bright field and dark field TEM images of a cross-sectioned bismuth nanopillar with diameter of 1100 nm. The grain boundaries were highlighted in Figure 3.2 (b) and show a large size distribution from roughly 100 nm to near 1  $\mu\text{m}$ . These images confirm the polycrystalline nature of the electroplated bismuth and also show that the nanopillar is dense without a significant amount of porosity. A few nanometer scale pores are observed in these figures; however, it is not clear that if they are artifacts produced during the FIB milling or intrinsic voids generated during the electroplating process. Additional TEM inspections also indicated that the bismuth nanopillar microstructure is well annealed with very few defects.

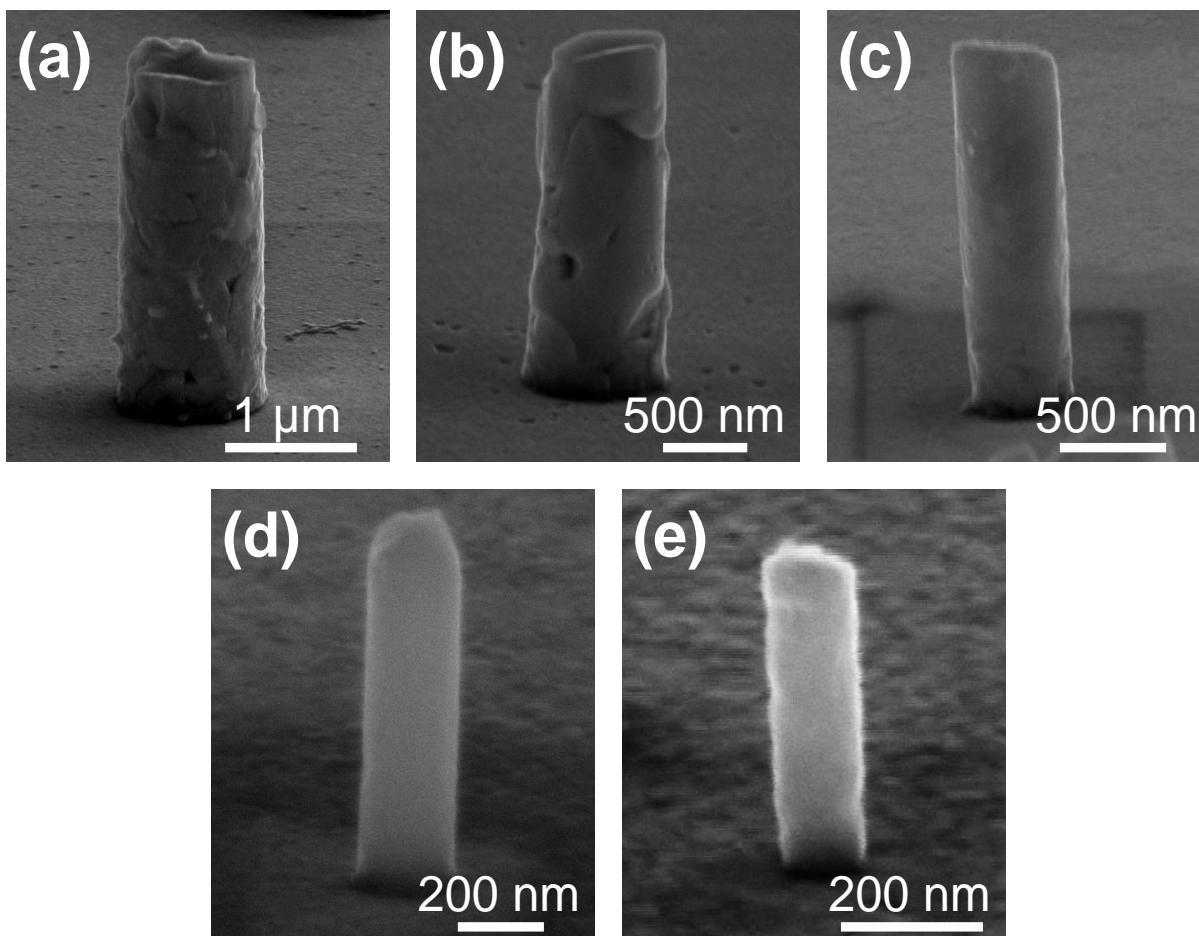


**Figure 3.1:** SEM images of as-fabricated bismuth nanopillars with diameters of (a) 1100 nm, (b) 840 nm, (c) 540 nm, (d) 230 nm, and (e) 130 nm. All SEM images taken at a 70° stage tilt.

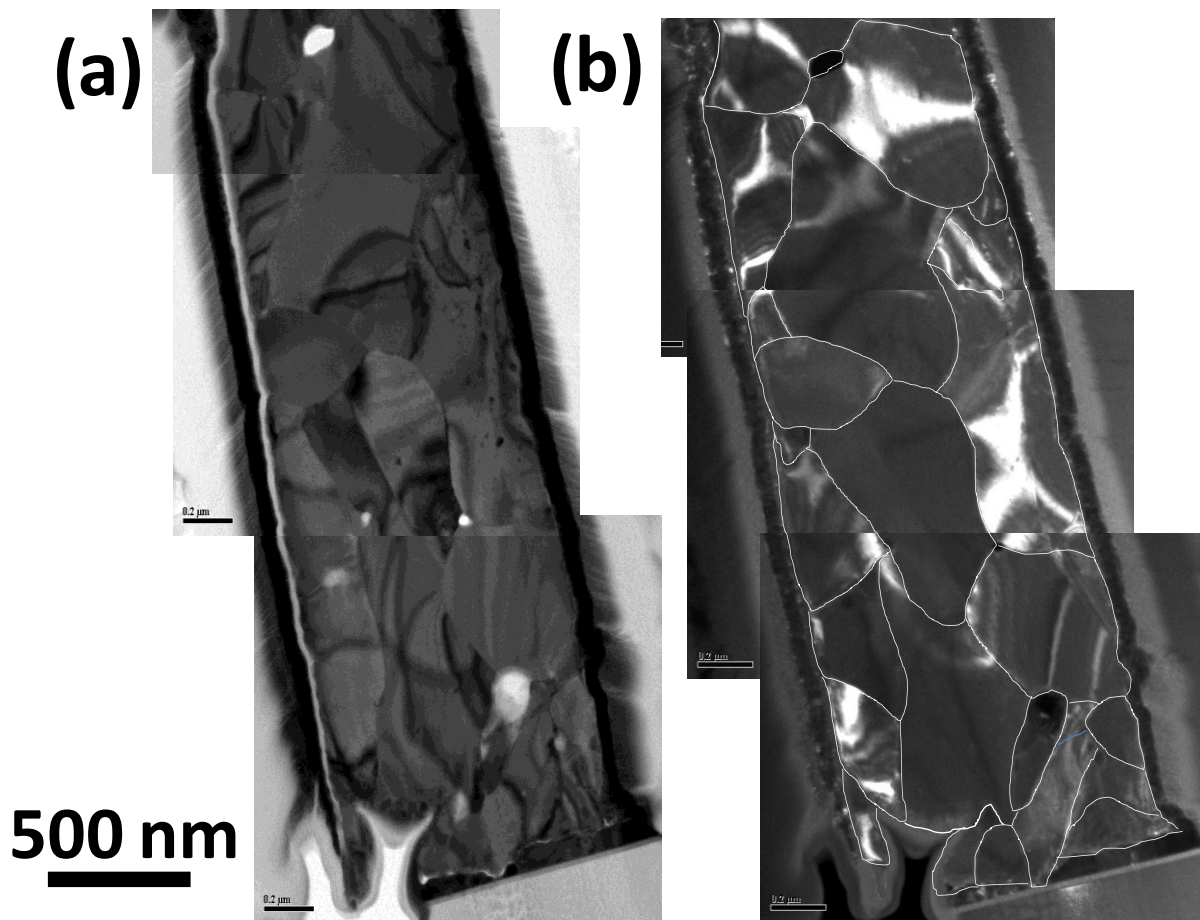


Figure 3.2: (a) TEM bright field image and (b) TEM dark field image of an 1100 nm diameter bismuth nanopillar. The grain boundaries of this nanostructure are highlighted in (b).

### 3.3.1 Stress-Strain Relationships and Size Effects

Figure 3.3 (a) to (e) shows representative engineering stress – strain curves generated from the uniaxial compression of bismuth nanopillars with diameters of 1100, 840, 540, 230, and 130 nm, respectively. All of these results were collected at a medium deformation rate of  $10^{-3} \text{ s}^{-1}$ . The figures reveal that for bismuth nanopillars with 1100 nm and 840 nm diameters, the stress – strain curves are generally smooth and display some strain hardening and softening behaviors. As the nanopillar diameter is reduced, the stress – strain behavior becomes much more stochastic and a higher frequency of displacement bursts is observed.

In order to fully understand the deformation mechanism of these small bismuth structures, all specimens were inspected by high-resolution SEM after uniaxial compression experiments. Figures 3.4 (a) to (e) display representative SEM images of deformed bismuth nanopillars with diameters of 1100 nm, 840 nm, 540 nm, 230 nm, and 130 nm respectively. For the compressed 1100 nm diameter nanopillar, Figure 3.4 (a) reveals that plastic strain is carried by the protrusion of grains from the sidewalls via grain boundary sliding and rotation. Interestingly, no discrete crystallographic slip lines are observed. Assuming the topographic features observed in Figure 3.4 (a) are a good representation of the overall deformation behavior, the mechanical deformation of 1100 nm diameter bismuth nanopillars appears to be dominated by grain boundary mediated mechanisms. Further examples of grain boundary mediated deformation in other 1100 nm diameter nanopillars are illustrated in Figure 3.4 (f). Again, plastic strain is carried by grain boundary activities, which are clearly visible in these deformed specimens. Figure 3.4 (b) shows a smaller bismuth nanopillar with diameter of 840 nm. In these slightly smaller specimens, grain boundary mediated deformation also appears to be the dominant deformation mode. In addition to grain boundary sliding and rotation, a small portion of the 840 nm diameter nanopillars also exhibited discrete crystallographic slip lines on the nanopillar surface. However, this deformation mode is very rare for the 840 nm diameter nanopillars. As the feature size is further reduced to 540 nm diameter bismuth nanopillars, discrete crystallographic slip lines are readily visible, as observed in Figure 3.4 (c). In contrast to the larger nanopillars, post-compression SEM analysis revealed that plasticity of 540 nm

diameter specimens is not governed by grain boundary mediated mechanisms. Instead, deformation is dominated by dislocation glide, which is confirmed by the presence of discrete crystallographic slip lines on the nanopillar surfaces. This suggests that a transition from grain boundary mediated deformation to dislocation glide as the dominant deformation mechanisms has occurred. Further examples to illustrate this transition are shown in Figure 3.4 (g). Evidence of deformation dominated by dislocation glide is also observed in 230 nm and 130 nm diameter bismuth nanopillars, as illustrated in Figures 3.4 (d) and (e), respectively. These features have the diameters smaller than the average grain size. Both specimens show crystallographic slip lines on the smooth specimen sidewalls, without any obvious grain boundary sliding or rotation.

The SEM images displayed in Figure 3.4 clearly show that grain boundary mediated deformation is the primary mechanism for 1100 nm and 840 nm bismuth nanopillars. In contrast, the deformation of bismuth nanopillars with 540 nm and smaller diameters is dominated by dislocation glide as revealed by the presence of crystallographic slip lines and without obvious evidence of grain boundary mediated deformation. The crystallographic slip lines observed in Figure 3.4 (g) are very similar to those ubiquitous with the deformation of virtually all other single-crystalline metals studied at the nanoscale ([11]-[20], [27]-[33]). This transition from grain boundary mediated deformation to dislocation glide may be attributed to the change in ratio of feature size to number of included grains. For large bismuth nanopillars that contain many crystals, the grain boundary area to volume ratio is very high. Therefore, the mechanical deformation is dominated by grain boundary mediated mechanisms because the CRSS is greater than the frictional stress between the grain boundaries. As the feature size is reduced, while the grain size distribution remains the same, the total number of included grains decreases, as well as the grain boundary area to volume ratio. Eventually, when the nanopillar diameter approaches the average grain size, the deformation will be localized to only a few grains or even a single grain. In this case, the nanopillar deformation will be dominated by dislocation glide along the active slip systems as in the case of single-crystals.

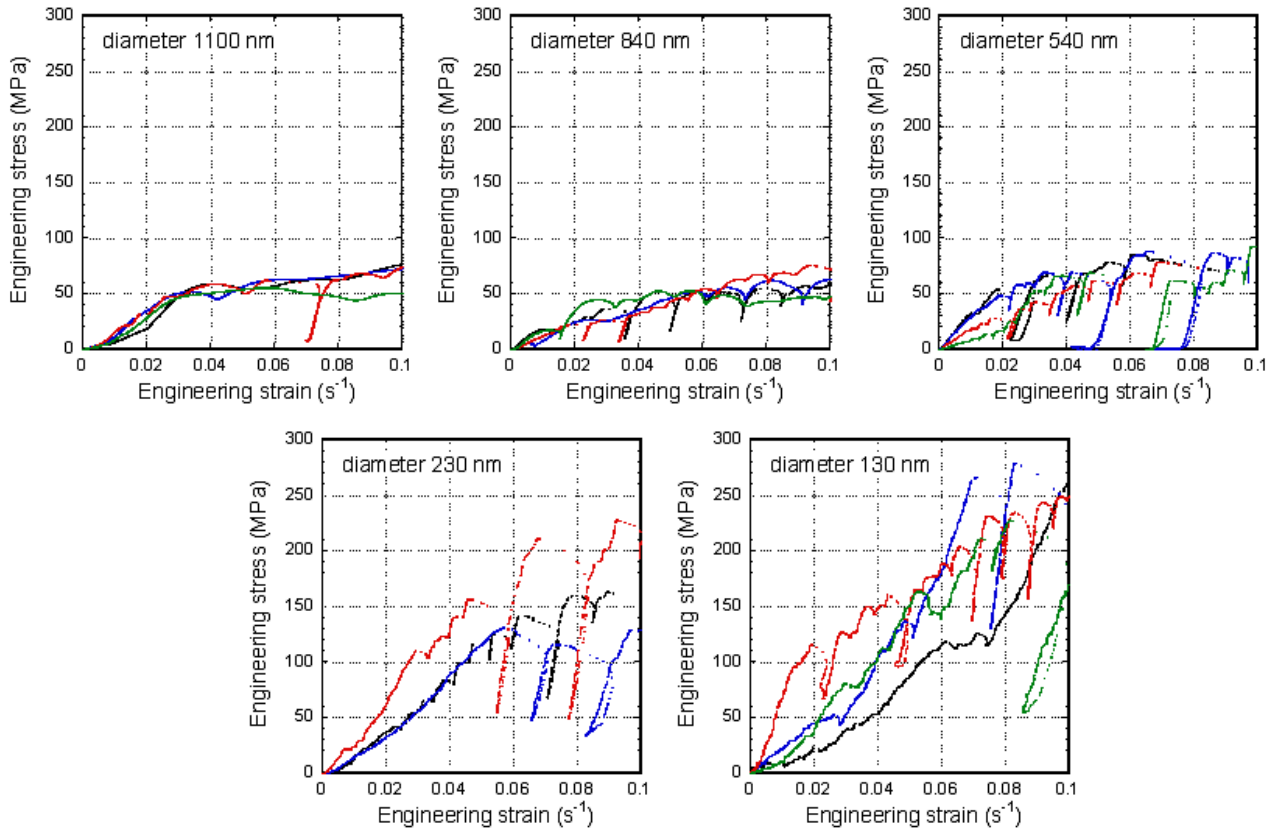
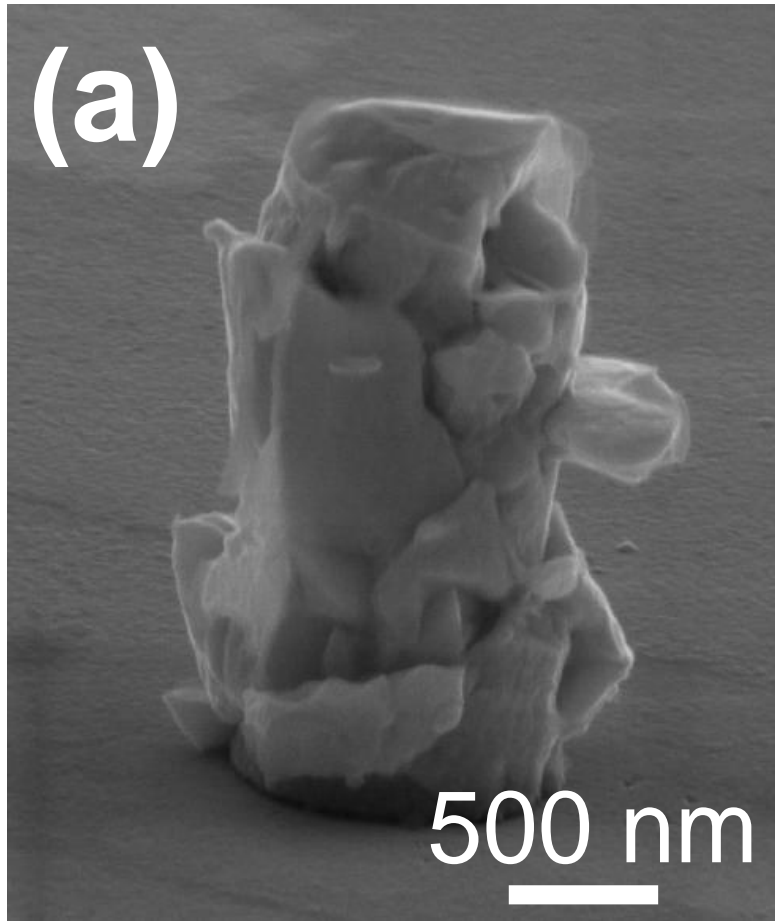


Figure 3.3: Representative engineering stress – strain curves for bismuth nanopillars. All specimens were deformed with a strain rate of  $10^{-3} \text{ s}^{-1}$

The engineering flow stresses measured at 5.0 % engineering strain for all bismuth nanopillars successfully compressed in this work are plotted as a function of strain rate in Figure 3.5. Figures 3.5 (a) and 6 (b) show that the 1100 nm and 840 nm diameter bismuth nanopillars display low strengths when compared with smaller specimens. The data also reveals that these specimens exhibit clear strain rate sensitivity, with faster deformation rates leading to higher mechanical strength. In contrast, the flow stresses of 540 nm diameter bismuth nanopillars, shown in Figure 3.5 (c), is nearly in-sensitive to strain rate. Interestingly, this change in deformation rate sensitivity coincides with the transition of nanopillar deformation mechanism from grain boundary mediated deformation to dislocation glide, as revealed previously by the post-compression SEM analysis. The average strengths of 540 nm diameter specimens are also slightly higher than the larger two sizes. Moving further to 230 nm diameter nanopillars results plotted in Figure 3.5 (d), it is clear that the strain rate sensitivity is virtually non-existent and the average strengths are now much greater than the larger nanopillars. Figure 3.5 (e) reveals the flow stress results of the 110 nm diameter structures which indicate these specimens are the strongest bismuth nanopillars tested in this work.

To quantify the size-dependent strain-rate effect described above, the average engineering flow stresses from Figure 3.5 are re-plotted in Figure 3.6 (a) and fitted with Eq. (3.1). The error bars shown in this plot correspond to one standard deviation. The stress exponents extracted from the flow stress show that 1100 nm and 840 nm bismuth nanopillars have stress exponent values of 12.10 and 10.83 respectively. These values are closely matched and indicate that a similar deformation mechanism is operating in these two different sized specimens. Remarkably, the strain rate sensitivity of the largest two nanopillar sizes are also comparable with the bulk polycrystalline data published by Das and Bever [67], which is also plotted in Figure 3.6 (a). These polycrystalline bismuth rods were tested in uniaxial compression yield a stress exponent of 9.88 when the data is fitted with Eq. (3.1) and bulk polycrystalline bismuth results match closely with those of 1100 nm and 840 nm diameter nanopillars.



**Figure 3.4: Post-compression SEM images of (a) 1100 nm, (b) 840 nm, (c) 540 nm, (d) 230nm, and (e) 130 nm diameter bismuth nanopillars. Additional post-compression SEM images of (f) 1100 nm and (g) 540 nm diameter specimens to illustrate the transition in deformation mechanism from grain boundary mediated deformation to deformation dominated by dislocation glide. All SEM images taken at a 70° stage tilt.**

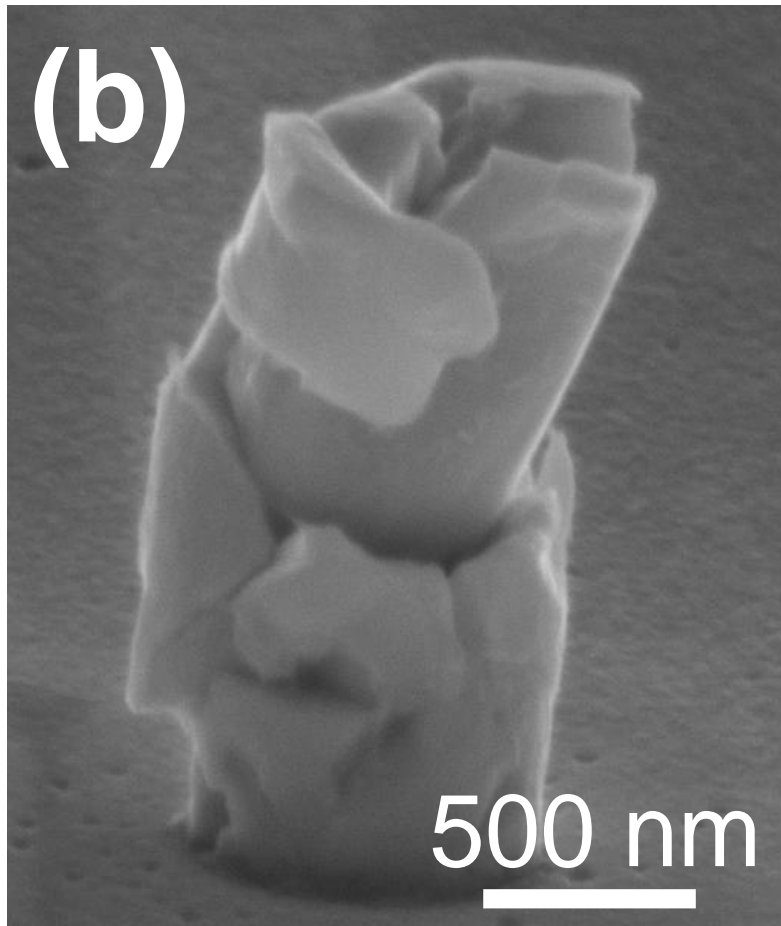


**Figure 3.4:** Post-compression SEM images of (a) 1100 nm, (b) 840 nm, (c) 540 nm, (d) 230nm, and (e) 130 nm diameter bismuth nanopillars. Additional post-compression SEM images of (f) 1100 nm and (g) 540 nm diameter specimens to illustrate the transition in deformation mechanism from grain boundary mediated deformation to deformation dominated by dislocation glide. All SEM images taken at a 70o stage tilt.

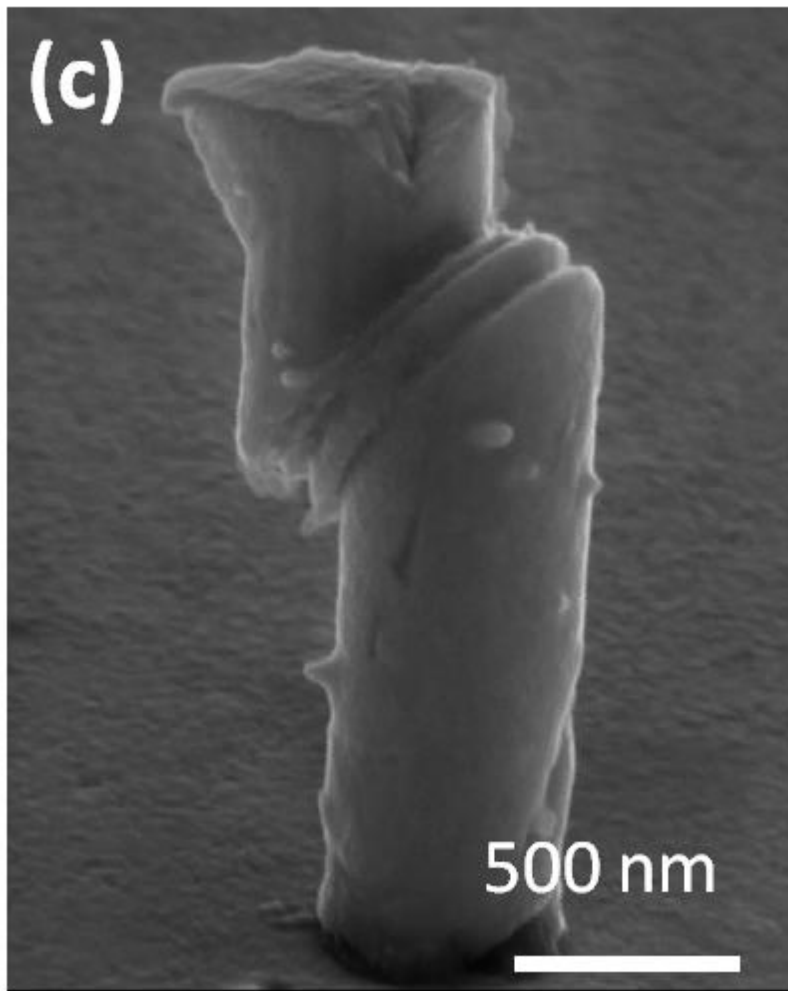


**Figure 3.4:** Post-compression SEM images of (a) 1100 nm, (b) 840 nm, (c) 540 nm, (d) 230nm, and (e) 130 nm diameter bismuth nanopillars. Additional post-compression SEM images of (f) 1100 nm and (g) 540 nm diameter specimens to illustrate the transition in deformation mechanism from grain boundary mediated deformation to deformation dominated by dislocation glide. All SEM images taken at a 70o stage tilt.

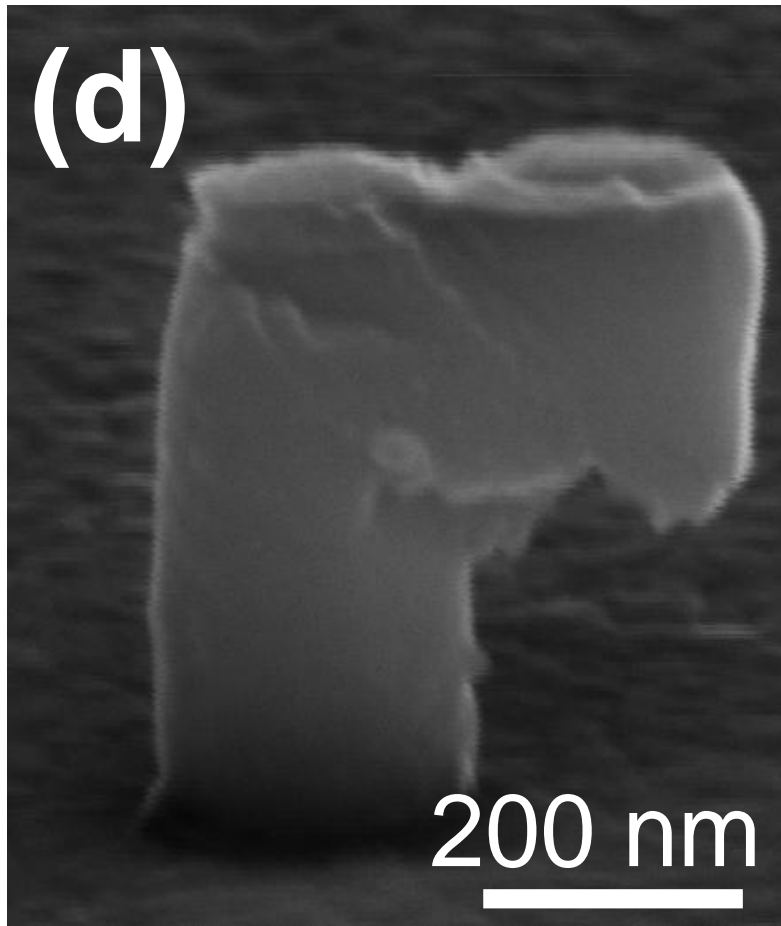


**Figure 3.4:** Post-compression SEM images of (a) 1100 nm, (b) 840 nm, (c) 540 nm, (d) 230nm, and (e) 130 nm diameter bismuth nanopillars. Additional post-compression SEM images of (f) 1100 nm and (g) 540 nm diameter specimens to illustrate the transition in deformation mechanism from grain boundary mediated deformation to deformation dominated by dislocation glide. All SEM images taken at a 70o stage tilt.

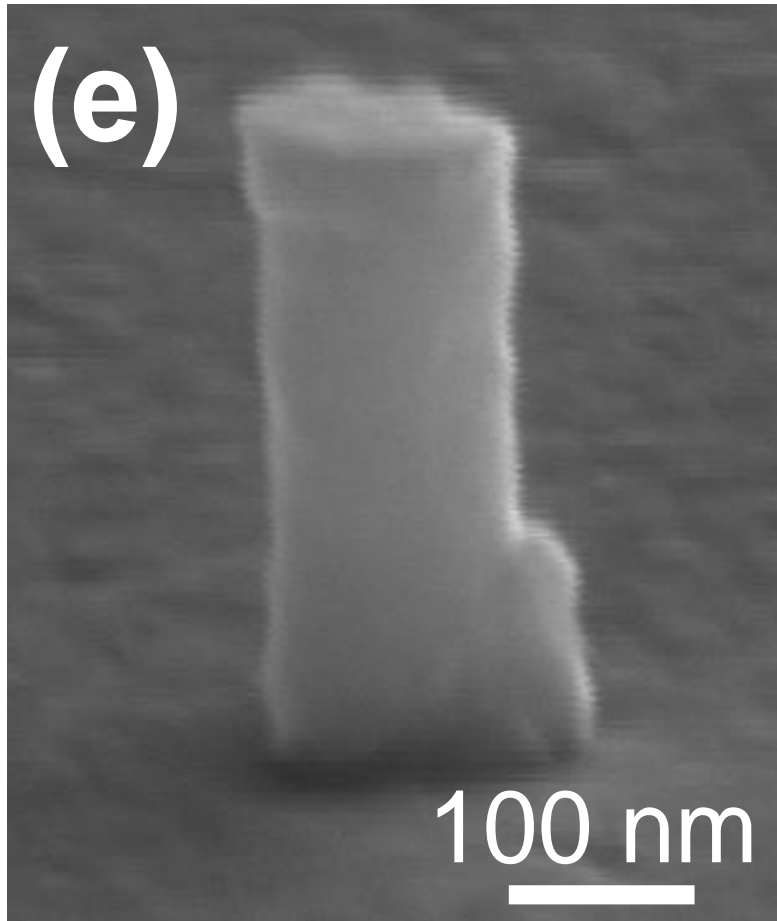


**Figure 3.4: Post-compression SEM images of (a) 1100 nm, (b) 840 nm, (c) 540 nm, (d) 230nm, and (e) 130 nm diameter bismuth nanopillars. Additional post-compression SEM images of (f) 1100 nm and (g) 540 nm diameter specimens to illustrate the transition in deformation mechanism from grain boundary mediated deformation to deformation dominated by dislocation glide. All SEM images taken at a 70o stage tilt.**

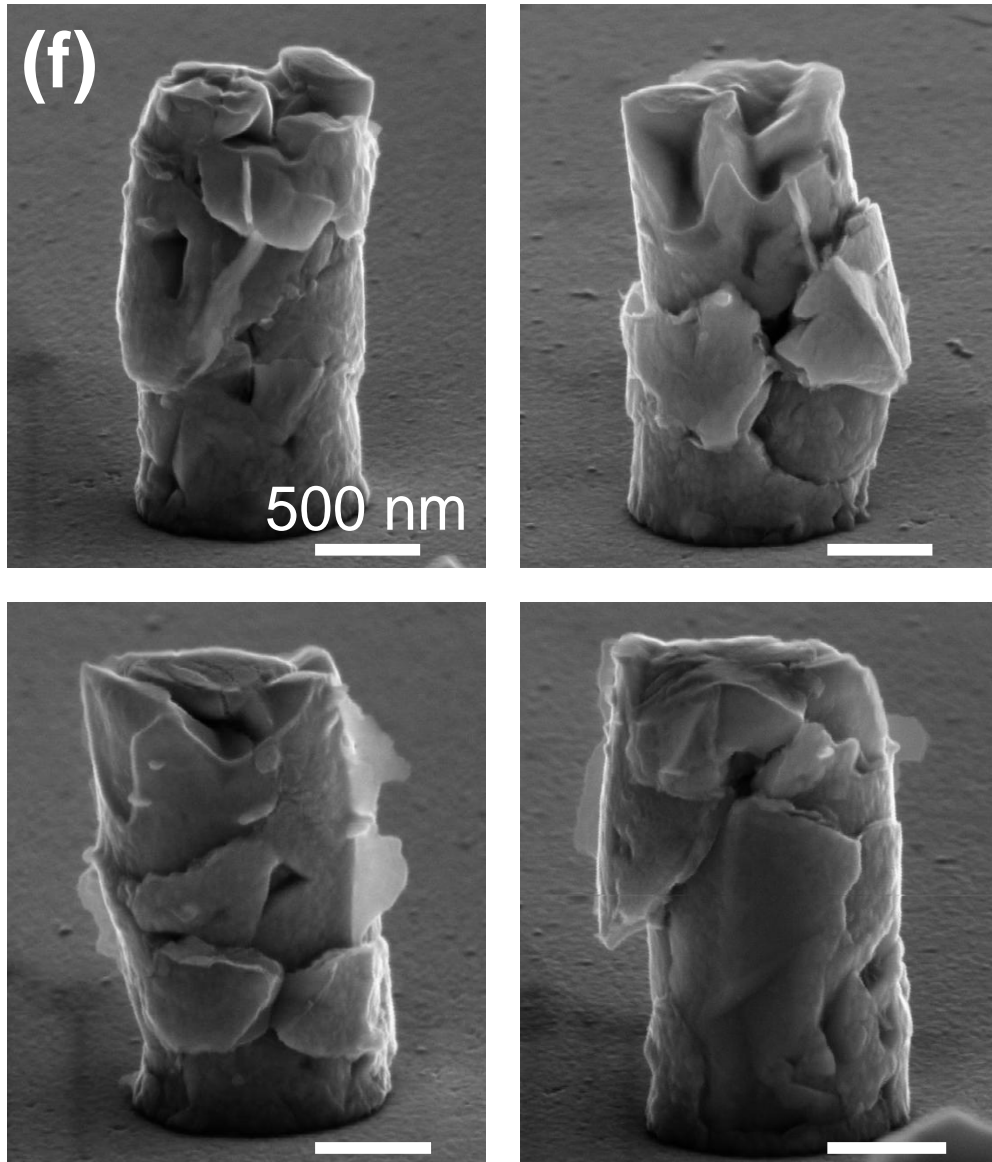


Figure 3.4: Post-compression SEM images of (a) 1100 nm, (b) 840 nm, (c) 540 nm, (d) 230nm, and (e) 130 nm diameter bismuth nanopillars. Additional post-compression SEM images of (f) 1100 nm and (g) 540 nm diameter specimens to illustrate the transition in deformation mechanism from grain boundary mediated deformation to deformation dominated by dislocation glide. All SEM images taken at a 70o stage tilt.

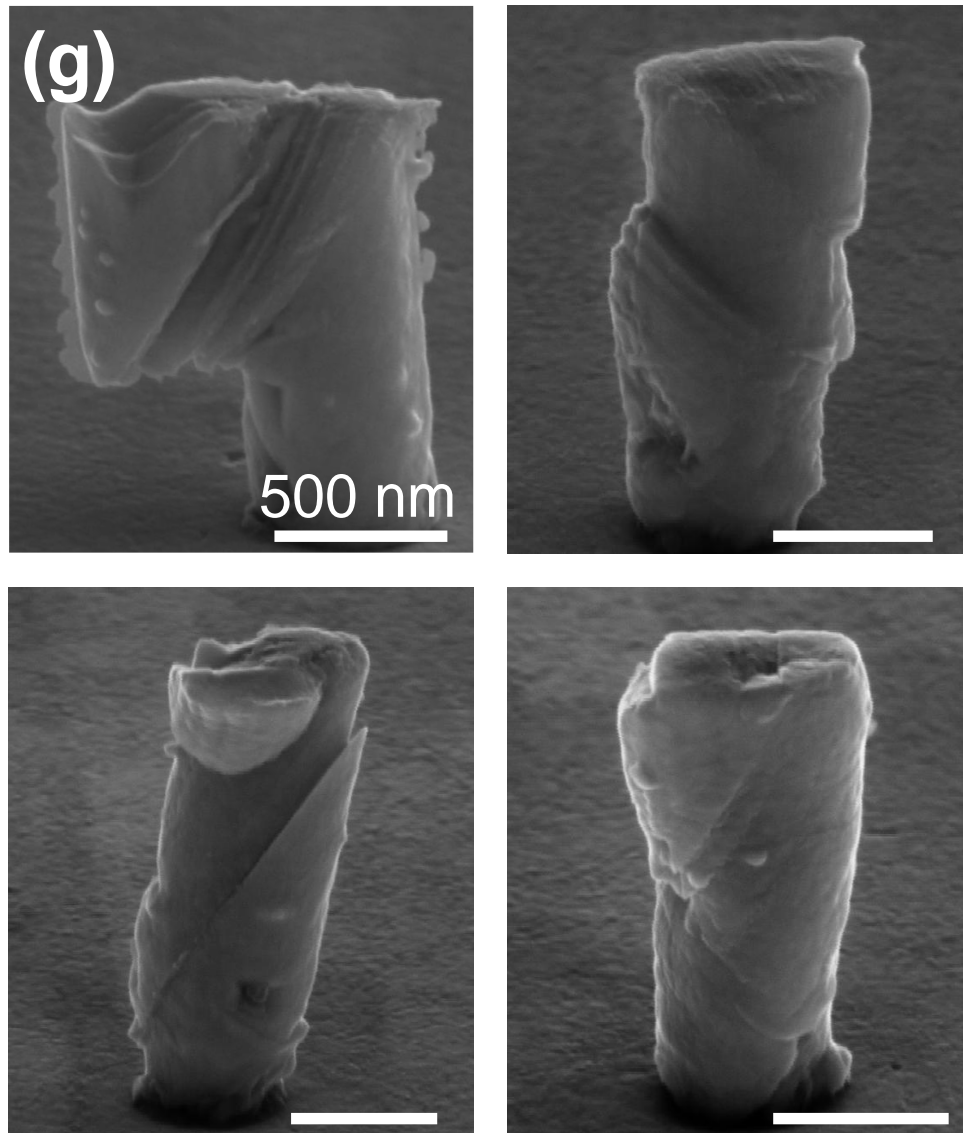


Figure 3.4: Post-compression SEM images of (a) 1100 nm, (b) 840 nm, (c) 540 nm, (d) 230nm, and (e) 130 nm diameter bismuth nanopillars. Additional post-compression SEM images of (f) 1100 nm and (g) 540 nm diameter specimens to illustrate the transition in deformation mechanism from grain boundary mediated deformation to deformation dominated by dislocation glide. All SEM images taken at a 70o stage tilt.

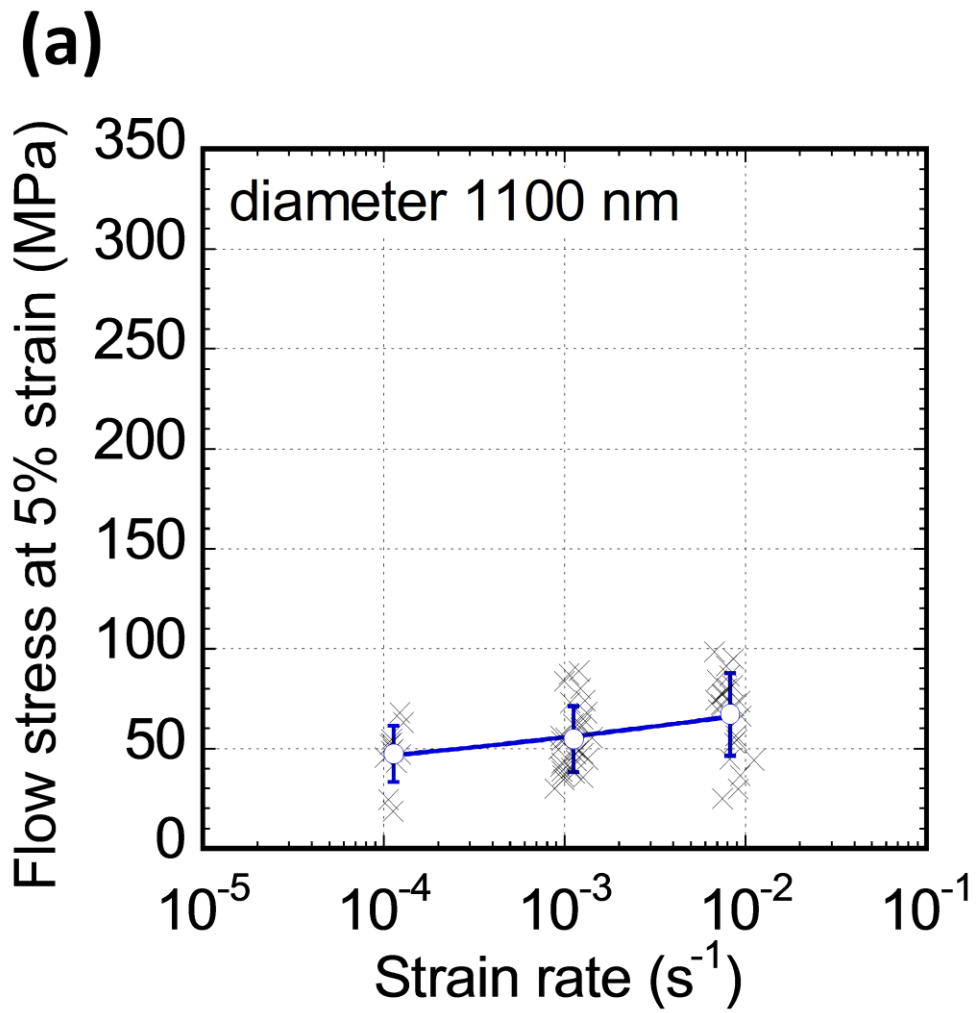


Figure 3.5: Log – log plots of engineering flow stress measured at 5.0 % strain as a function of engineering strain rate for (a) 1100 nm, (b) 840 nm, (c) 540 nm, (d) 230nm, and (e) 130 nm diameter bismuth nanopillars. The average flow stress values are indicated by blue circles with error bars indicating one standard deviation.

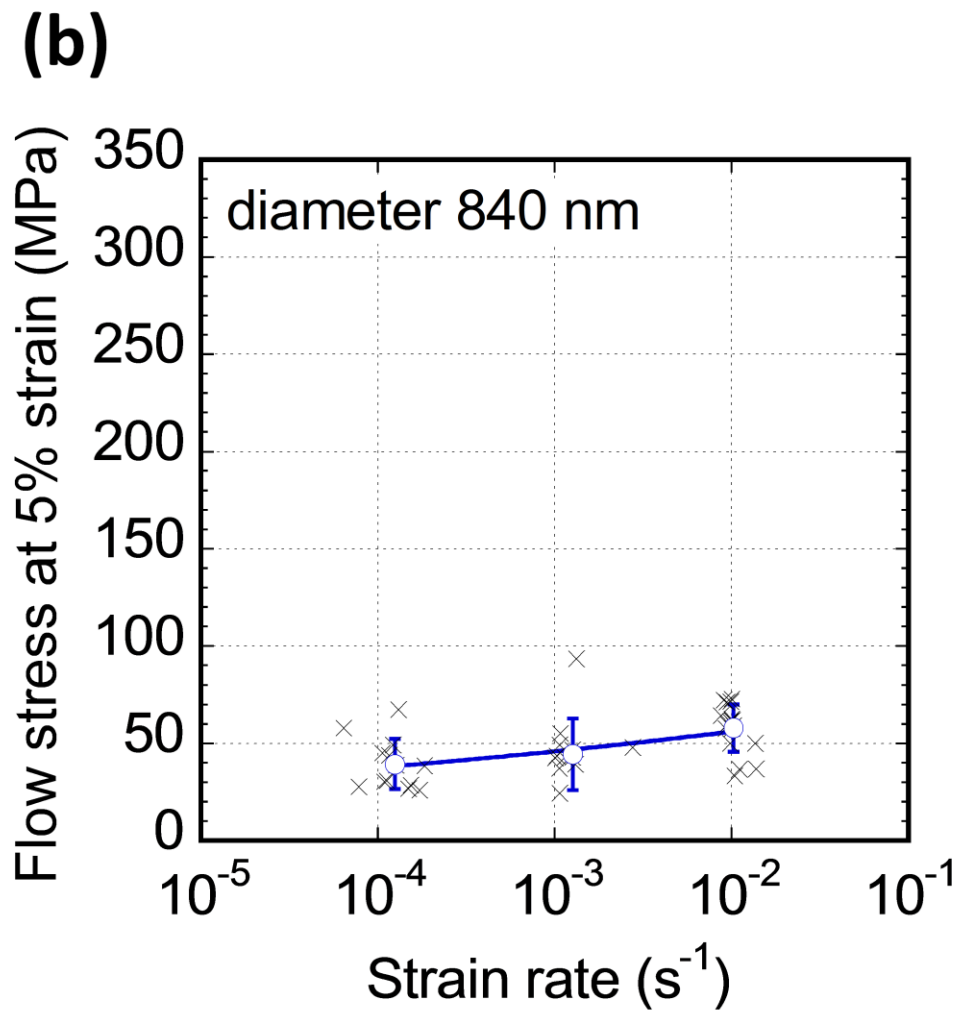


Figure 3.5: Log – log plots of engineering flow stress measured at 5.0 % strain as a function of engineering strain rate for (a) 1100 nm, (b) 840 nm, (c) 540 nm, (d) 230nm, and (e) 130 nm diameter bismuth nanopillars. The average flow stress values are indicated by blue circles with error bars indicating one standard deviation.

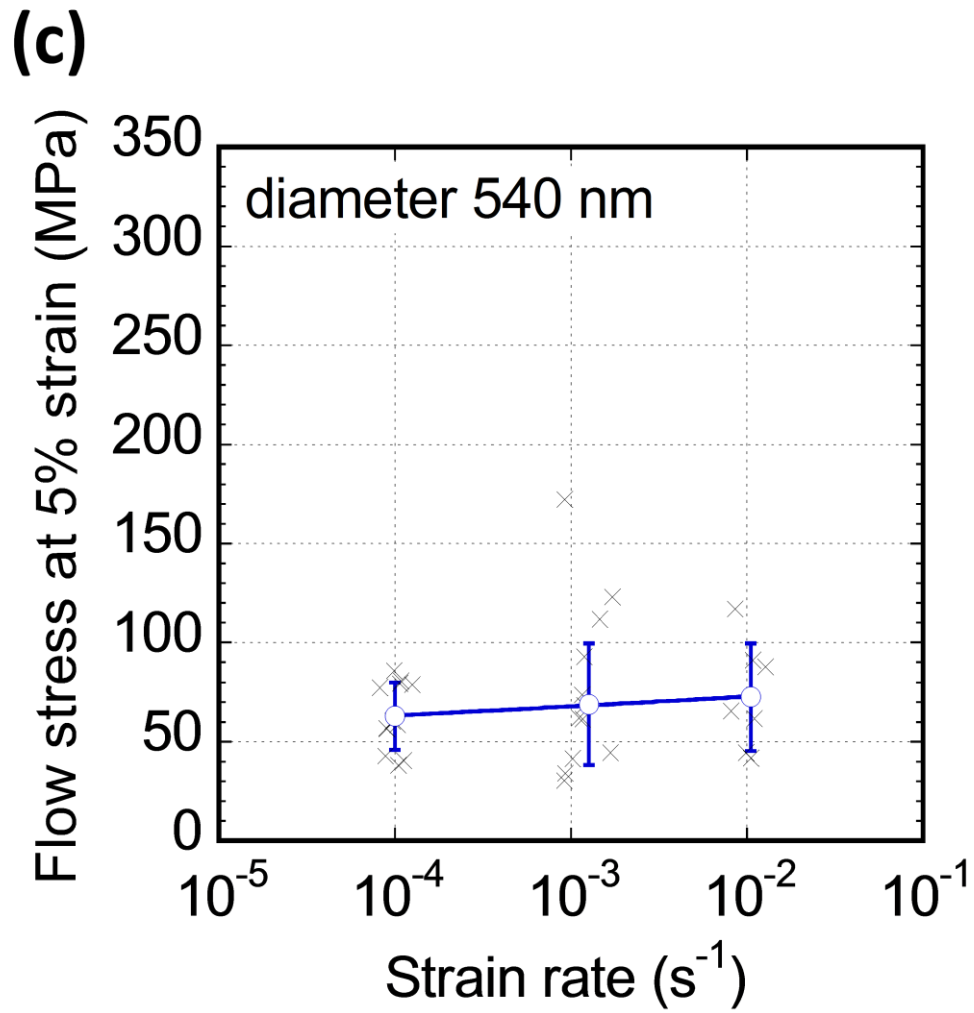


Figure 3.5: Log – log plots of engineering flow stress measured at 5.0 % strain as a function of engineering strain rate for (a) 1100 nm, (b) 840 nm, (c) 540 nm, (d) 230nm, and (e) 130 nm diameter bismuth nanopillars. The average flow stress values are indicated by blue circles with error bars indicating one standard deviation.

**(d)**

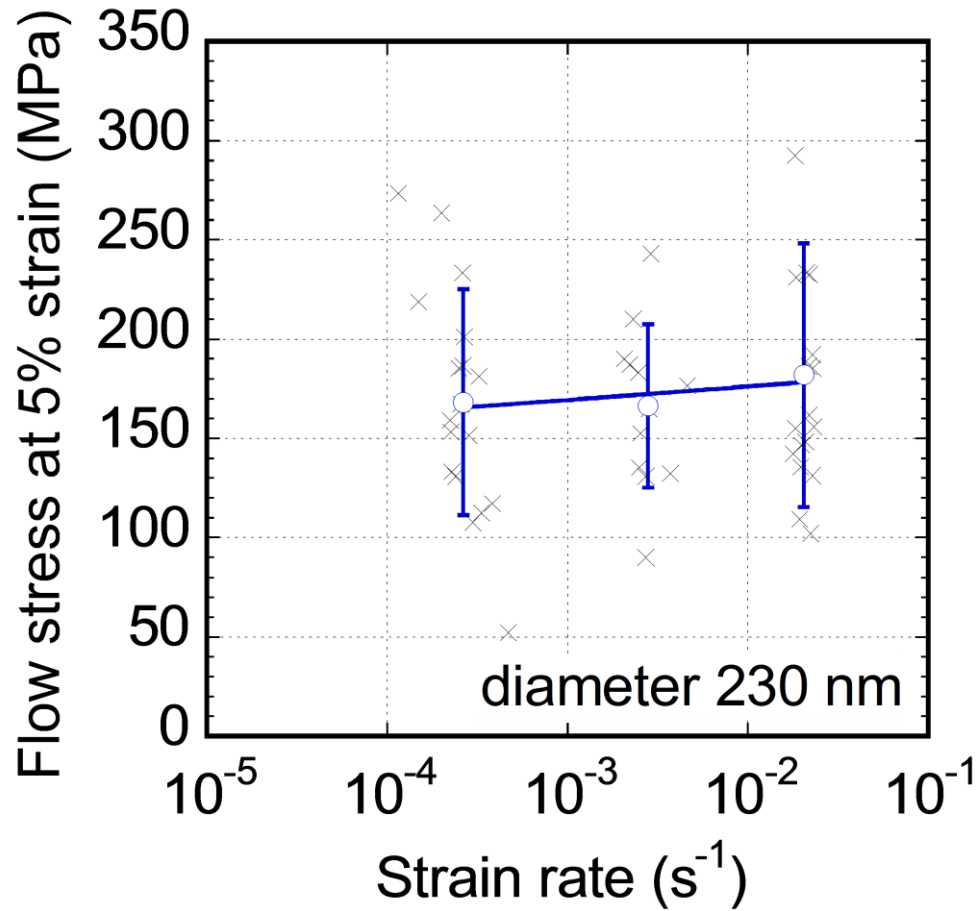


Figure 3.5: Log – log plots of engineering flow stress measured at 5.0 % strain as a function of engineering strain rate for (a) 1100 nm, (b) 840 nm, (c) 540 nm, (d) 230nm, and (e) 130 nm diameter bismuth nanopyllars. The average flow stress values are indicated by blue circles with error bars indicating one standard deviation.

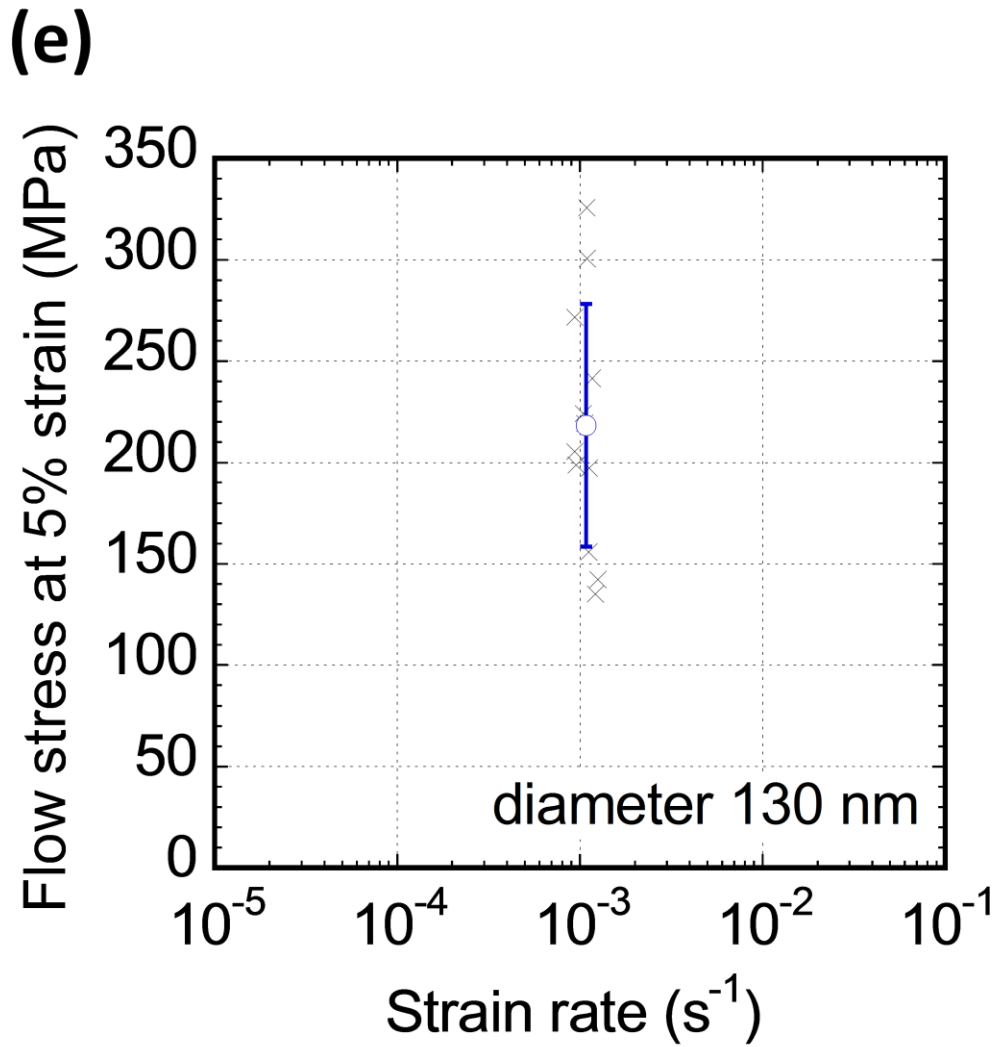


Figure 3.5: Log – log plots of engineering flow stress measured at 5.0 % strain as a function of engineering strain rate for (a) 1100 nm, (b) 840 nm, (c) 540 nm, (d) 230nm, and (e) 130 nm diameter bismuth nanopillars. The average flow stress values are indicated by blue circles with error bars indicating one standard deviation.

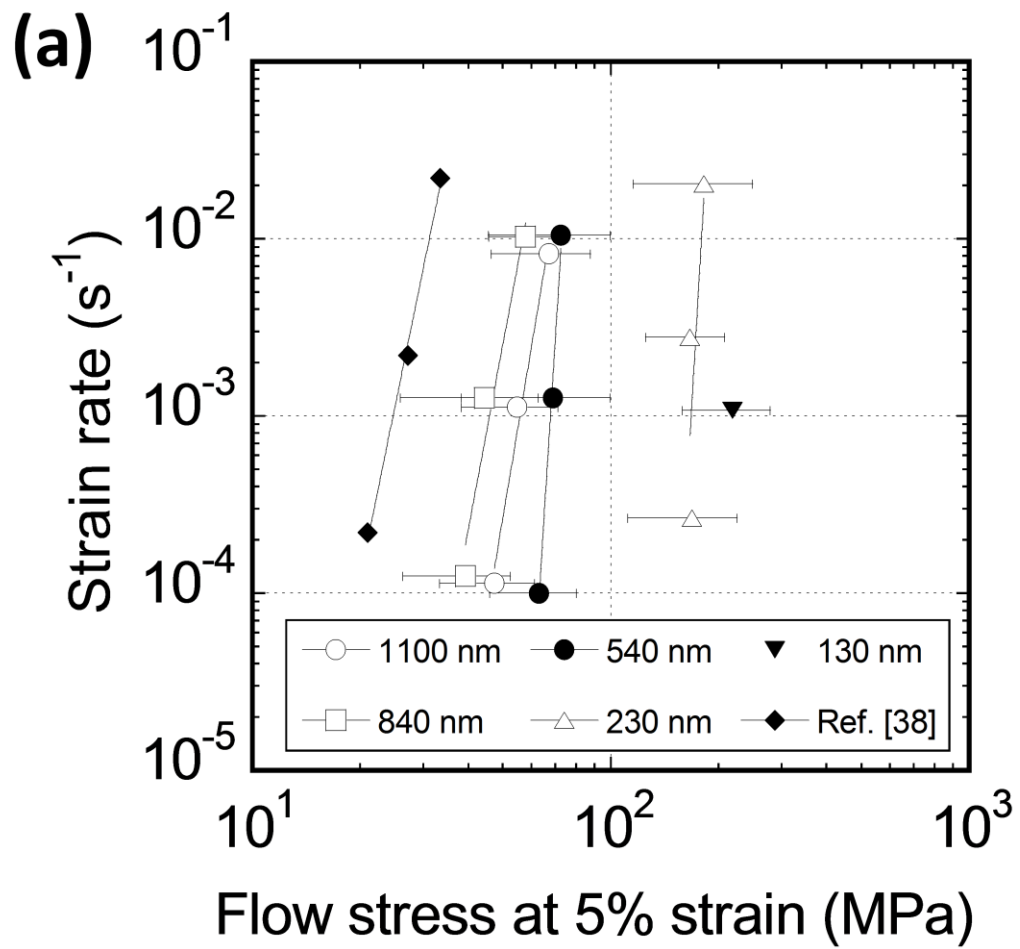


Figure 3.6: (a) Log – log plot of averaged engineering strain rate as a function of engineering flow stress measured at 5.0 % strain and (b) linear plot of engineering flow stress measured at 5.0 % engineering strain as a function of nanopillar diameter. (c) Log-log plot of engineering flow stress measured at 5.0 % engineering strain for 540 nm, 230 nm, and 130nm diameter nanopillars. The error bars indicate one standard deviation

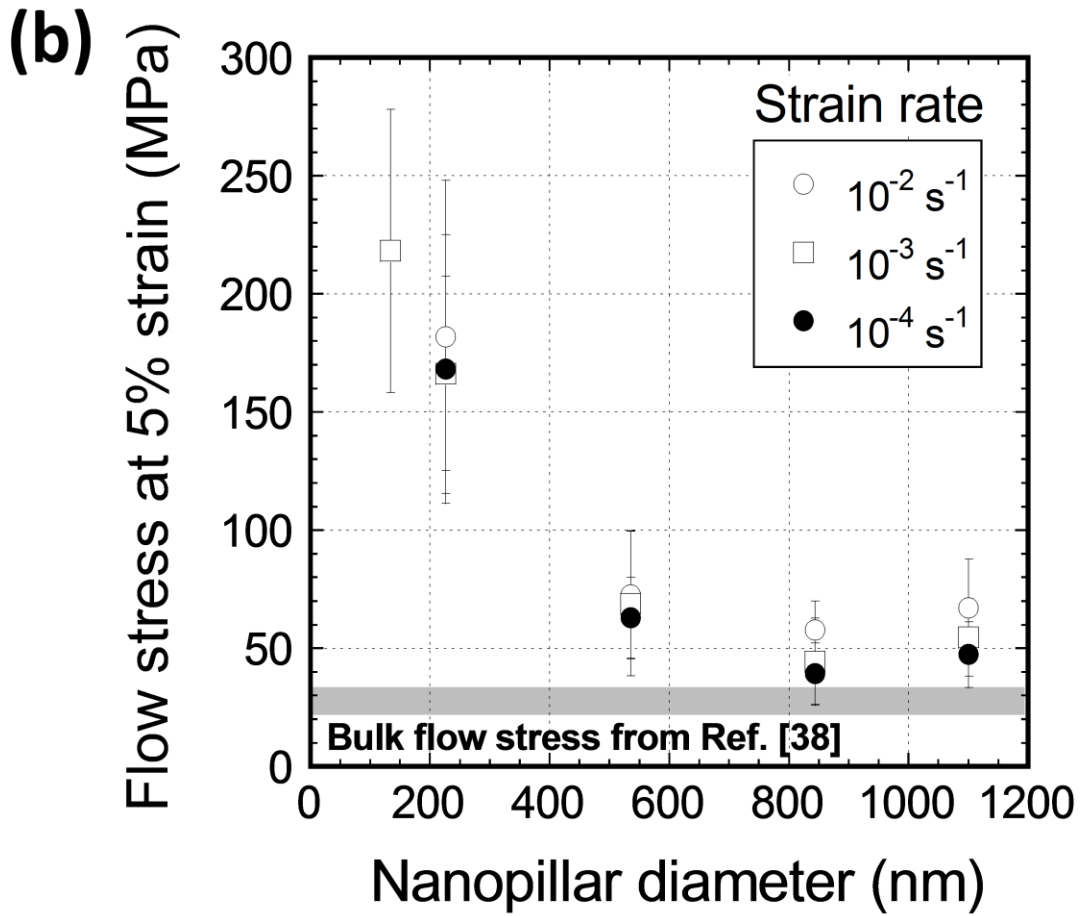


Figure 3.6: (a) Log – log plot of averaged engineering strain rate as a function of engineering flow stress measured at 5.0 % strain and (b) linear plot of engineering flow stress measured at 5.0 % engineering strain as a function of nanopillar diameter. (c) Log-log plot of engineering flow stress measured at 5.0 % engineering strain for 540 nm, 230 nm, and 130nm diameter nanopillars. The error bars indicate one standard deviation

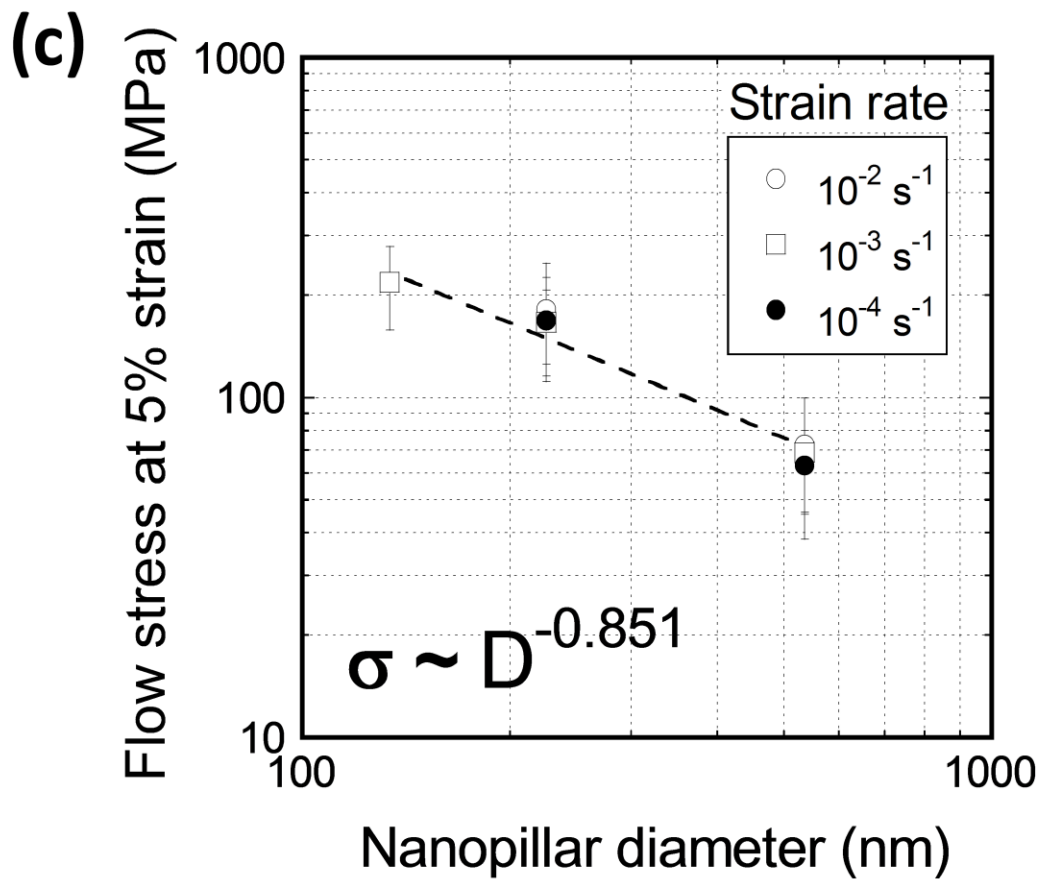


Figure 3.6: (a) Log – log plot of averaged engineering strain rate as a function of engineering flow stress measured at 5.0 % strain and (b) linear plot of engineering flow stress measured at 5.0 % engineering strain as a function of nanopillar diameter. (c) Log-log plot of engineering flow stress measured at 5.0 % engineering strain for 540 nm, 230 nm, and 130nm diameter nanopillars. The error bars indicate one standard deviation

The stress exponents calculated for smaller bismuth nanopillars with diameters of 540 nm and 230 nm are 32.25 and 34.57, respectively. These values are significantly larger than the stress exponents calculated for 1100 nm and 840 nm diameter nanopillars discussed above, as well as the bulk polycrystalline bismuth [67]. As seen from Eq. (3.1), larger stress exponent values indicate decreasing strain rate sensitivity, where a value approaching infinity is completely insensitive to deformation rate.

The large stress exponent values for the smaller bismuth nanopillars suggest that a reduction in feature size has significantly diminished the influence of deformation rate. A lack of strain rate sensitivity in bulk bismuth single-crystals was also observed by Otake *et al.* [68]. Their results showed that the CRSS of bismuth primary slip system(111)[110] is insensitive to the deformation rate at temperatures greater than  $\sim 300$  K. Hence, the results of the strain rate analysis suggest that the 540 nm and 230 nm diameter bismuth nanopillars deform by a similar mechanism as bulk bismuth single-crystals. The previous postcompression SEM analysis demonstrated that reducing the bismuth nanopillar size from 840 nm to 540 nm in diameter was accompanied by a transition from grain boundary mediated deformation to deformation which is dominated by dislocation glide. As such, the lack of strain rate sensitivity observed in 540 nm and 230 nm diameter specimens may be explained by an increase in the ratio of grain to feature size and the resulting transition in dominant deformation mechanism. Therefore, it is reasonable to suspect that the strain rate sensitivity of smaller bismuth nanopillars will be similar to the singlecrystal deformation behavior. The effects of grain boundary mediated deformation on strain rate sensitivity were also observed in other metals. Mayo and Nix [72] performed a nanoindentation creep test on pure tin polycrystalline specimens. Their data showed that the strain rate sensitivity measured when the indentation contact area includes grain boundaries is  $\sim 44$  % greater than those results obtained when the indentation was localized within a single grain.

The size-dependent deformation mechanism in bismuth nanopillars observed here highlights the importance of identifying the actual operating deformation mechanisms in any material prior to establishing conclusions on nanoscale mechanical properties. For example, variations in the strain rate sensitivity exhibited by metallic nanopillars may not be necessarily the result of dislocation dynamics.

Interplay between grain size and feature size – i.e. a grain size effect – may also contribute to the change in the mechanical response during compression tests. This is particularly important for specimens with polycrystalline or nanocrystalline microstructures. Figure 3.6 (b) shows the average engineering flow stresses measured at 5.0 % engineering strain as a function of bismuth nanopillar diameter. The 1100 nm and 840 nm diameter bismuth nanopillars exhibit strengths which are comparable to each other and only slightly greater than the bulk polycrystalline value [67]. In the case of 540 nm diameter nanopillars, the average flow stresses are slightly greater than the larger specimens. There are two possible explanations for this observed increase in mechanical strength. Firstly, reduced sidewall roughness in 540 nm bismuth nanopillars significantly eliminates the presence of stress concentrators which can weaken the nanopillar. Figures 3.1 (a) and 3.1 (b) clearly show the 840 nm and 1100 nm diameter nanopillar consist of a large amount of grain boundaries which cause small voids on the nanopillar surface. These surface features can act as stress concentrators and reduce the mechanical strength of the structure. For smaller nanopillars with diameter of 540 nm, Figure 3.1 (c) shows the number of grain boundaries contained within the structure is greatly reduced and the nanopillar surface is much smoother. The elimination of stress concentrating surface topography will most likely increase the structural strength of the bismuth structures. Alternatively, the change in dominate deformation mechanism exhibited by the 540 nm diameter nanopillars may also be responsible

for the increased strength. It is reasonable to assume that in the case of deformation dominated by dislocation glide, the effect of nanopillar surfaces will yield a similar size-effect as seen in the compression of single-crystalline metallic nanopillars (i.e. smaller is stronger) ([11]-[33]). This idea is further supported by the flow stresses of 230 nm and 130 nm diameter nanopillars, which are considerably stronger than bulk polycrystalline bismuth. Moreover, it is clear that a progressive size effect in the strength of bismuth nanopillars 540 nm in diameter and smaller exists like in virtually all other studies of single-crystalline cubic metals at the nanoscale. As shown in chapter 1, in a recent review by Uchic *et al.* [2] on the nanoscale mechanical properties of metals, it was illustrated that singlecrystalline metallic nanopillars which exhibit yield strength size effects follow an empirical power-law relationship

between the strength of the sample ( $\sigma$ ) and the nanopillar diameter ( $D$ ):

$$\sigma \propto D^{-\gamma}$$

(3.2)

where the parameter  $\gamma$  is the power-law exponent. In their work, Uchic *et al.* showed that most size dependent strengthening data for nanoscale face centered cubic (FCC) single-crystalline metals (i.e. Ni, Au, Cu, and Al) could be collapsed onto a single line by plotting the normalized resolved shear effective stress versus pillar diameter and the result of this normalization yielded a power-law exponent of -0.6. In the case of rhombohedral bismuth nanopillars with diameters 540 nm and smaller, flow stress data from Figure 3.5 (b) were fitted with Eq. (3.2) and the power-law exponent value of -0.851 was obtained, as shown in Figure 3.5 (c).

### 3.4 Conclusions

Compared to the studies in chapter 2 on tin single crystal nanopillars, the electroplated Bismuth nano pillars showed a polycrystalline structure in the case of the larger pillar sizes allowing a study on the size effects and strain rate sensitivity of a polycrystalline nanostructure. Bismuth showed two types of size effect. First due to a reduction in the number of grains (i.e. lower grain boundary area to pillar volume), and therefore a change in the dominant deformation mechanisms from grain boundary sliding to dislocation processes within a grain, the larger pillar sizes (1100nm and 840nm) were lower in strength than the smaller sizes. When the pillar reaches a diameter near the grain size, and the entire pillar consists of a single grain, the pillars exhibit a deformation similar to that seen in single-crystals mediated by dislocation processes and therefore show another size effect where the pillar strength increases as a function of pillars size due to dislocation processes mostly attributed to dislocation starvation.

## Chapter 4: Nano-crystalline Palladium

### 4.1 Background on Nanocrystalline Metals and Pd Applications

Palladium is the least dense and lowest melting temperature metal among the platinum group metals (PGMs). It has an FCC crystal structure with a high melting temperature of 1828.05 K.

In macro scale, with a great increase in surface area, palladium is used as a sensor to monitor hydrogen at very low concentrations by adsorption [73].

With a similar density to that of Silver and because of its light weight, palladium is also used extensively as a jewellery metal [74]. In the electronic industry, palladium is a cheaper replacement of gold for the electro plating of the electronic components [74]. Palladium and palladium based alloys are known to be used for dental crowns and bridges in dentistry [74]. Finally, due to its compatibility with human tissue, palladium is used for the treatment of cancer (most commonly prostate cancer) in the medical industry [75].

In this chapter, using the fabrication methods presented in previous chapters, nanocrystalline palladium nanopillars were fabricated and characterized. A nanocrystalline material is a material with an average grain size of less than 100nm [76]. TEM images show average grain sizes of 20nm or less for these fabricated pillars.

In bulk scale, a polycrystalline material deforms with the movement of dislocations and their pile up and interactions at grain boundaries which impede the motion of dislocations. By decreasing the grain size, the number of piled up dislocations can be minimized and would lead to higher energies needed to deform the material. It is simply easier for a dislocation to move within a rather ordered grain than through a disordered grain boundary from one grain to another. This results in a great strengthening effect in nanocrystalline materials compared to their bulk counterparts. The Hall Petch effect is a well known relation between the yield stress ( $\sigma_y$ ) and grain size( $d$ ) of a material based on this concept:

$$\sigma_y = \sigma_0 + \frac{k_y}{\sqrt{d}}$$

where  $\sigma_0$  and  $k_y$  are material specific constants. Based on this relation, materials should become stronger as the grain diameters decreases. However, several studies of nanocrystalline materials with grain sizes smaller than 100nm have shown to not follow this relation. At nanoscale, smaller grain sizes seem to results in a decrease in the strength of the materials and this is known as the Inverse Hall Petch effect. So there exists a critical grain size after which the Hall petch effect will invert, and the strength of the material will stay constant or even decrease.

The palladium nanopillars prepared using the electroplating method described in this work were nanocrystalline with a grain size of less than 20nm.

There are several theoretical and experimental studies of nanocrystalline material in bulk scale. However, when it comes to the deformation of material with nanoscale dimensions the behaviour of material has shown to be different. Nanopillars are surface dominated structures and made up of a limited of number grains, with limited sources for plasticity. Therefore their deformation behaviour is expected to differ from that of bulk nanocrystalline material. Although there has been a vast amount of research on single crystal nanopillar deformation, there has been very little experimental work done on the deformation of polycrystalline nanopillars, with only some studies on Ni and Cu ([77]-[78]). This is merely due to the difficulty in the preparation of bulk nanocrystalline material. Greer et al. studied the deformation of 60nm grained Ni nanopillars and found that the pillar strength decreases with a decrease in pillar diameter (i.e. the Nickel nanopillars softened as the pillar size decreased). This size effect differs from the previously presented size dependant strengthening of single crystal and polycrystalline metals including the ones presented in chapter 2 and 3 ([11]-[20], [78]).

Properties of bulk scale palladium nanocrystals prepared using other methods such as physical vacuum deposition method [79] and inert gas condensation [80], have been studied however there is no literature on the fabrication, or the study of mechanical behaviour of nanocrystalline palladium at nano and micro scale using this method.

The deformation mechanisms of nanocrystalline metals, including Pd are mostly limited to MD simulations ([81]-[83]); there is not much experimental work done on the plastic deformation of these

metals. Due to the nano-sized near perfect crystals, the operation of dislocation sources is very limited and therefore other deformation mechanisms are expected to cause the plastic deformation of these metals. It is believed that the grain boundary structures of nanocrystalline metals are very disordered thereby requiring high energies for dislocation movement between grains.

The studies of Birringer on the elastic properties of nanocrystalline palladium and copper found that these metals yield at stresses 10-15 times than those in coarse-grained annealed metals [84]. Nieman et al. were among the first to test the tensile properties of nanocrystalline metals where they observed a yield stress ~7 times greater than a bulk palladium sample with large grain sizes [84].

Grain boundary diffusion creep is also known to be a dominant mechanism in the deformation of nanocrystalline materials. Based on a review by D. Wolf, it seems to be accepted in the literature that the deformation in nanocrystalline material is dominated by dislocation processes up to a certain grain size. In the literature, at a grain size of about 30 nm, the deformation mechanism of nanocrystalline material transits from dislocation processes to grain boundary processes. After this critical size, a softening effect is seen where as the grains get smaller, the material yield strength and flow stresses decrease. As mentioned previously, the inverse Hall-Petch effect is a term associated with this size effect.

## **4.2 Experimental Methods**

Palladium nanopillars were prepared using the same electron beam lithography and electroplating techniques mentioned in previous chapters. A palladium electrolyte purchased from Technology Without Limits Inc. was used to deposit nanocrystalline palladium into the patterned PMMA resist template. This solution was maintained at 22°C with constant mechanical agitation throughout the deposition process. The gold/titanium seed layer underneath the PMMA resist template acted as the cathode and a platinized titanium metal rod was used as a soluble anode. The total cathode area, which included the patterned PMMA coated substrate, and a blank 1 cm<sup>2</sup> gold/titanium coated silicon wafer chip, was kept at 1 cm<sup>2</sup>. For the electroplating process, a constant current density value of 18 mA/cm<sup>2</sup> was maintained. The target aspect ratio (height/diameter) was 3:1 and the deposition time was adjusted according to the desired

nanopillar height. After electroplating, the PMMA resist was removed with acetone. Three different palladium cylindrical structures with average diameters of approximately 140 nm, 240 nm, 550 nm were successfully fabricated. The uniaxial compression tests of palladium nanopillars were performed using an *in-situ* nanoindenter (Nanomechanics Inc, Knoxville, TN, USA) equipped with a custom diamond flat punch tip with a diameter of 8  $\mu\text{m}$  similar to the methods mentioned in previous chapters. To investigate the strain rate sensitivity and the possible size effects of these fabricated pillars, each pillar size was compressed at 3 nominal strain rates.

### 4.3 Results and Discussion

#### 4.3.1 Fabricated Pillar Structures

Palladium pillars with different diameters and height to diameter aspect ratios were fabricated using the methods explained in the previous sections. Figure 4.1 shows SEM images of the fabricated nanopillars with diameters  $\sim 490\text{nm}$ ,  $\sim 220\text{nm}$  and  $\sim 125\text{nm}$ . The average height to diameter ratios of the pillars studied for compression were kept under 3 to avoid buckling. Buckling seemed to be a more apparent issue in the micro-compression of high-strength material. Some  $\sim 125\text{nm}$  Pillars were fabricated with aspect ratios up to 10 and the mechanical behaviour of these pillars were also studied to determine the buckling load of these pillars. Details of this study are presented in chapter 6.

The microstructure of a 500 nm diameter palladium nanopillar was also characterized using transmission electron microscopy (TEM). An individual palladium nanopillar was sectioned and polished by using the focused ion beam (FIB) milling method [71]. The thinned palladium nanopillar foil was then transferred to a TEM lift-out grid via an omniprobe nanomanipulator. Figures 4.2 (a)-(b) reveal the bright field and dark field TEM images of a cross-sectioned palladium nanopillar with a diameter of 500 nm. As it can be seen in figure 4.2-(b), only a few number of grain boundaries can be identified based on this TEM study however these images confirm the polycrystalline nature of the electroplated palladium, and show the few identified grains are of nanometer size. This TEM study was done only on the 500nm pillar size and since

the plating conditions were kept constant for each pillar size, it is reasonable to assume that all fabricated pillars have the same grain size and are nanocrystalline. However, more TEM studies need to be done to confirm this.

Compared to the single crystal pillars, where the pillar top forms based on the crystal structure, the palladium nanocrystalline pillars grow in a uniform manner with flat top surfaces. This makes them suitable for microcompression tests by minimizing the non-uniform stress distributions during the initial contact of the pillar and the nanoindenter.

### 4.3.2 Stress-Strain Relationships

The engineering stress versus the engineering strain results were extracted from the load-displacement outputs of the indenter. Figure 4.3 shows 3 representative curves from the compression of 500 nm palladium nanopillars with an average height to diameter ratio of 2.5. Several pillars were compressed and the attained flow stress at 8% strain was extracted for each pillar. By an analysis of post compression SEM images, pillars that had buckled during the compression tests were eliminated from the results. The average value of the flow stress at 8% strain for the 15 remaining good data points compressed at a strain rate of  $0.001 \text{ s}^{-1}$  was  $\sim 1.97 \pm 0.315 \text{ GPa}$  showing the reproducibility of the data.

In bulk, the strength of nanocrystalline metals are expected to be much higher than that of polycrystalline metals with coarse grains based on the Hall Petch effect. As seen from a representative stress-strain curve for the 500nm nanopillars, these pillars attain a strength of about  $\sim 1.97 \pm 0.315$  which is much higher than any value seen in the literature. Early studies by Nieman et al. showed a yield strength  $\sim 7$  times greater for bulk nanocrystalline Pd than annealed coarse grained Pd which has a tensile yield strength of  $\sim 40 \text{ Mpa}$  ([84]-[85]). Sanders also studied the tensile properties of nanocrystalline palladium and was able to reach a yield strength 10-15 times larger than the course grained palladium. For bulk scale nanocrystalline palladium with grain sizes from 10-100nm, the tensile stress at 0.2% strain was reported to be 250 MPa [84]. Although this attained value is much higher, in another study, Sanders argues that these values are still lower than the expected values and are not compatible with the extrapolation of

coarse-grain Hall-Petch data to the nanocrystalline regime. Sanders relates this to the imperfections in sample preparations and shows that a compressive yield strength in the orders of 1 GPa can be reached for palladium and Cu nanocrystalline specimens [86]. The attained strength of the palladium nanopillars prepared by electroplating method is slightly higher than the values obtained by Sanders which can be attributed to near zero impurity or flaw in these nanosized pillars.

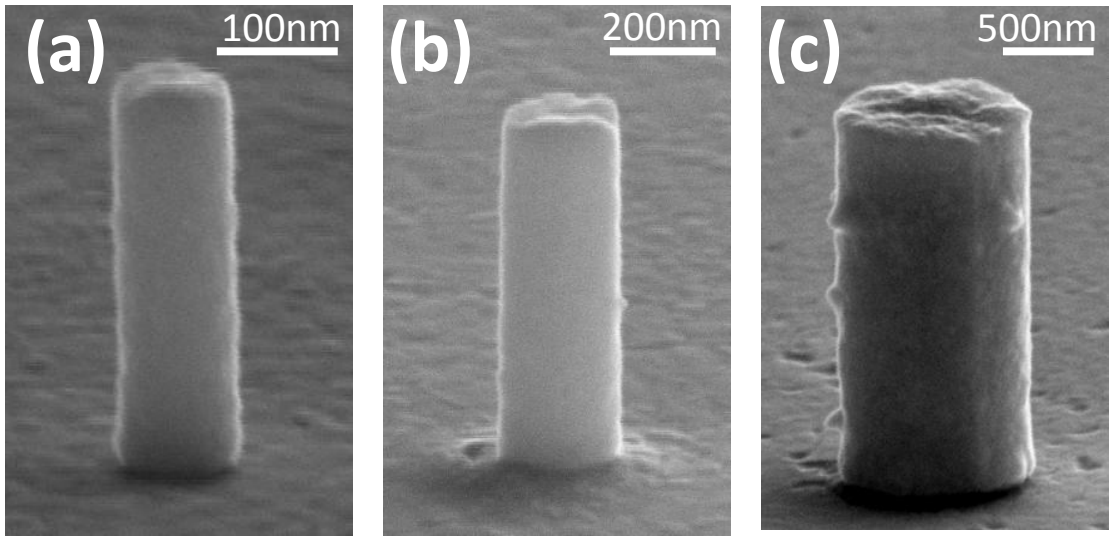


**Figure 4.1:** SEM images of as-fabricated palladium nanopillars with diameters of (a) 120, (b) 240 nm, (c) 540 nm. All SEM images taken at a 70° stage tilt

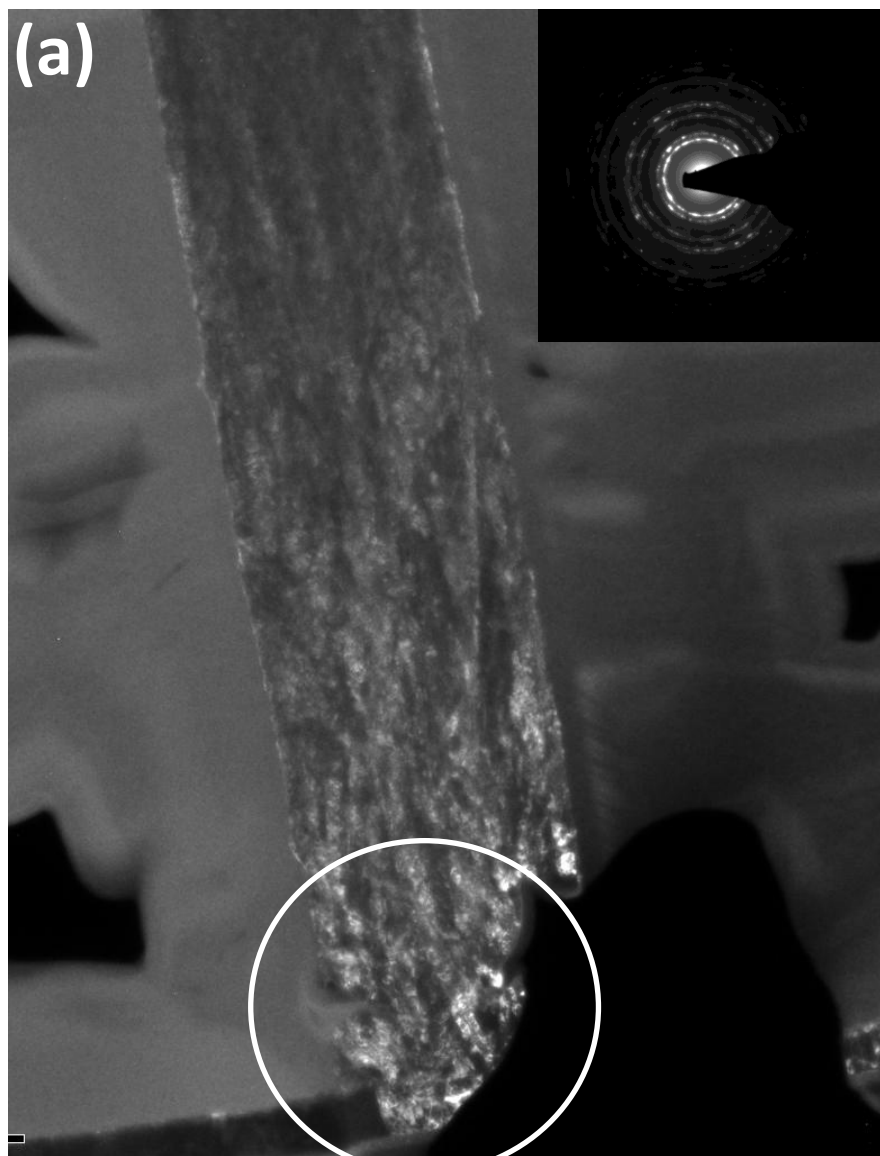


**Figure 4.2:** (a) TEM dark field image of the full length of a ~520 nm palladium nanopillars along with diffractoin pattern. (b) Dark field high magnification image of a section of the palladium nanopillar (c) Dark field high magnification image of a section of the palladium nanopillar

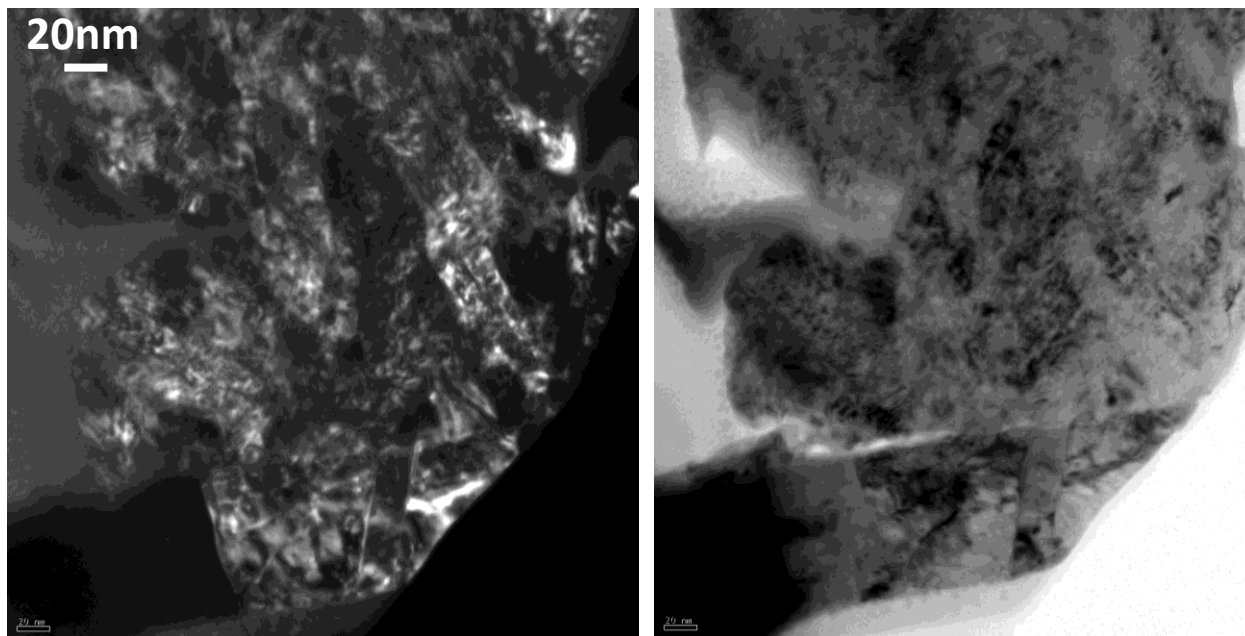


**Figure 4.3: (a) TEM dark field image of the full length of a ~520 nm palladium nanopillars along with diffractoin pattern. (b) Dark field high magnification image of a section of the palladium nanopillar (c) Dark field high magnification image of a section of the palladium nanopillar**

### 4.3.3 Strain Rate Sensitivity

In the previous chapters, we showed that a relation exists between the flow stress ( $\sigma$ ) and the strain rate ( $\dot{\epsilon}$ ) at which the nanopillars are compressed which can be explained with a power law fit:

$$\dot{\epsilon} = K\sigma^n$$

where  $K$  is a material constant that depends on diffusivity and elastic modulus [69], and  $n$  is the stress exponent. The value of  $n$  for single crystal material was similar to the stress exponent in bulk scale deformation in the case of Sn and In single crystals (refer to chapters 2 and 6). For nanocrystalline material in bulk scale, based on simulations ([87]-[89]) and some experimental work, the strain rate sensitivity of the stress ( $m = 1/n$ ) is expected to be much higher than their coarse grained counterparts.

Wei et al. studied the role of grain boundary sliding and diffusion in the control of strain rate sensitivity of nanocrystalline materials for various grain sizes [90]. Their study shows that this increase in strain rate sensitivity is also a function of strain rate and is only true for lower strain rates ( $<10^{-4}$ /s in the case of nc Cu). Their results show that for a fixed grain size for nanocrystalline Cu, the strain rate sensitivity increases rapidly for strain rates less than  $10^{-6}$ /s due to primarily GB diffusion and sliding deformation mechanisms. For strain rates between  $10^{-6}$ /s and  $10^{-4}$ /s, GB creep and grain interior plasticity contribute to the deformation and therefore the strain rate sensitivity increase is at a lower rate. Finally, the results show that at strain rates above  $10^{-2}$ /s, the primary dislocation mechanism is “dislocation controlled plasticity in grain interiors” where the deformation is strain rate insensitive.

Due to limitations in the load controlled nanoindenter tool that was used for the compression tests, we were not able to study the deformation of the 500nm Pd nanopillars at strain rates lower than  $10^{-3}$ /s. For the 3 strain rates higher than  $10^{-3}$ , the results shown in figure 4.4 indicate that the flow stresses extracted from the compression tests at different strain rates are very similar with a low strain rate sensitivity of  $\sim m = 0.068$  - i.e. the flow stress is nearly independent of the strain rate. These results agrees with the simulation [87] and experimental data [91] for nanocrystalline Cu with an average grain

size of 30nm which showed that at higher strain rates ( $>10e-3/s$ ) grain interior plasticity is the dominant deformation mechanism rather than grain boundary sliding (which is argued to be dominant deformation mechanism in nc material).

#### 4.3.4 Size Effect

In the microcompression single crystals, an inverse relation was seen between the pillar diameter and pillar strength. However, the results for nanocrystalline palladium show a different trend. As it can be seen in figure 4.5, a softening effect is seen with a decrease in pillar diameter. The strength of a nanocrystalline palladium nanopillar drops from  $\sim 1.97$  GPa for a 500nm pillar to  $\sim 713$  MPa for a 100nm pillar. Representative stress-strain curves for pillars of different diameters shown in figure 4.6 also verify this size effect. This decrease in strength was also seen by Greer et al. in the microcompression of nanocrystalline Nickel nano pillars with an average grain size of 60nm.

In Chapters 1 and 2, it was shown that in a single crystal nano pillar, the existence of free surfaces mediated the dislocation starvation process resulting in an increase in pillar strength with an increase in pillar surface area to volume ratio. In nanocrystalline material however, since dislocation processes are not the dominant mechanisms, it is reasonable to assume that surfaces will act as defects and features that are on the surfaces of a pillar can act as stress concentrators which could result in a reduction of the pillar strength. As the pillar size reduces, the ratio between the area of the cylindrical pillar and its volume increases (this ratio is  $\sim 2.67/r$  for a cylinder with a constant height to diameter ratio of 3). Also, the free surfaces on the nanopillar structure may activate deformation mechanisms that are not seen in the bulk scale deformation of nanocrystalline metals.

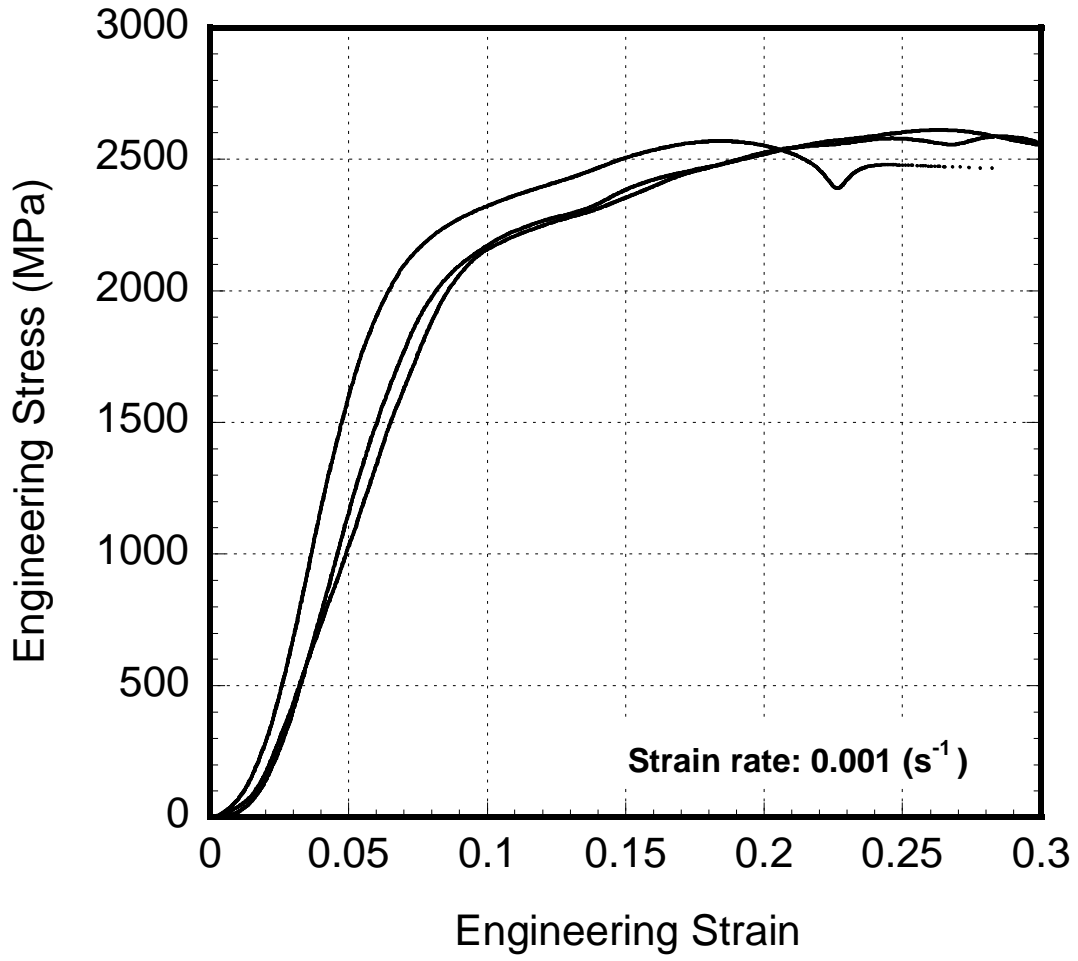


Figure 4.4: Engineering Strain vs. Engineering Stress for 540 nm Palladium nano-pillars under compression (b) SEM images of 240 nm Palladium nano-pillars going through plastic deformation before (left) and after (right) compression

**(b)**

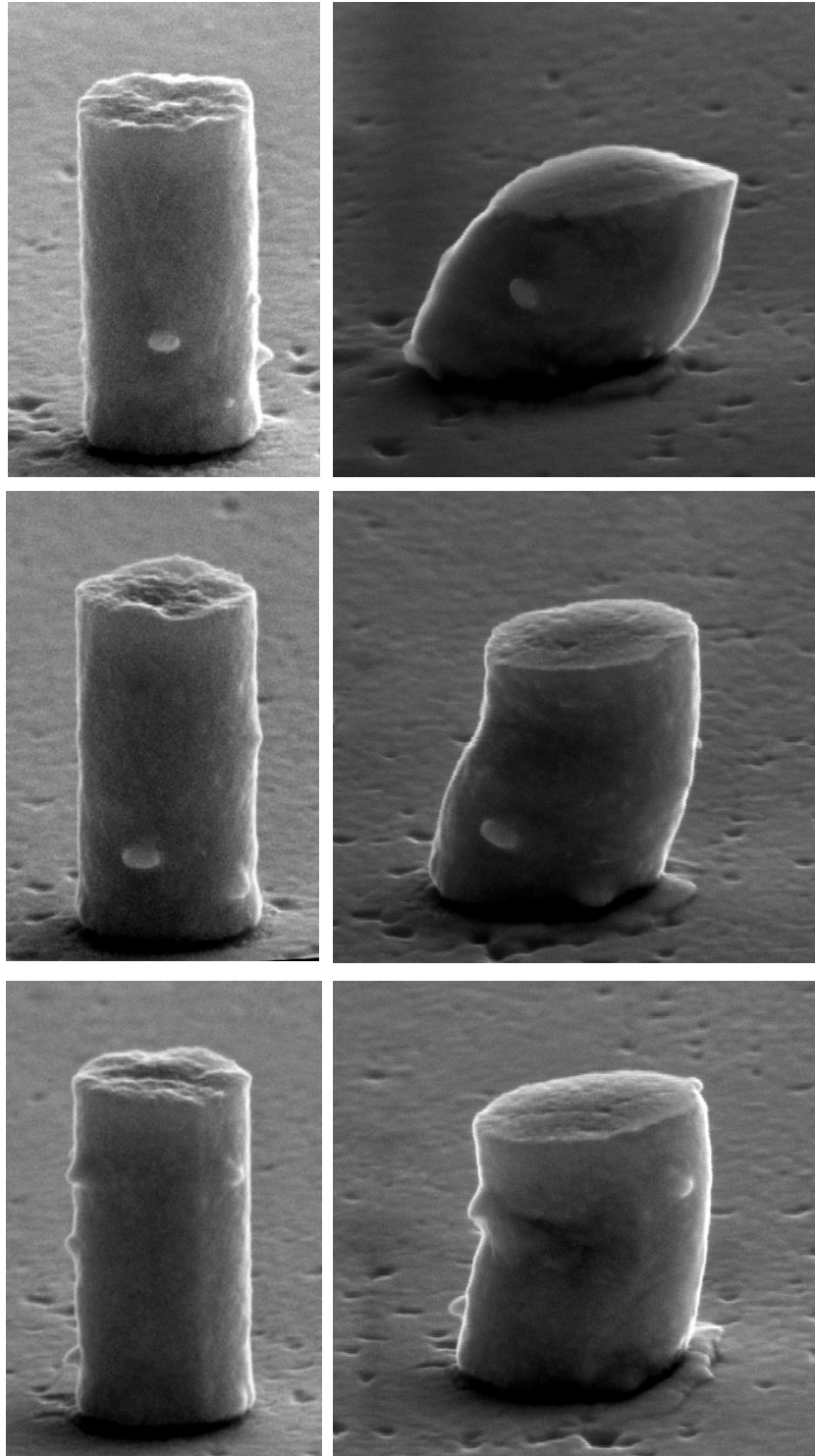


Figure 4.5: Engineering Strain vs. Engineering Stress for 550 nm palladium nano-pillars under compression (b) SEM images of 240 nm Palladium nano-pillars going through plastic deformation before (left) and after (right) compression

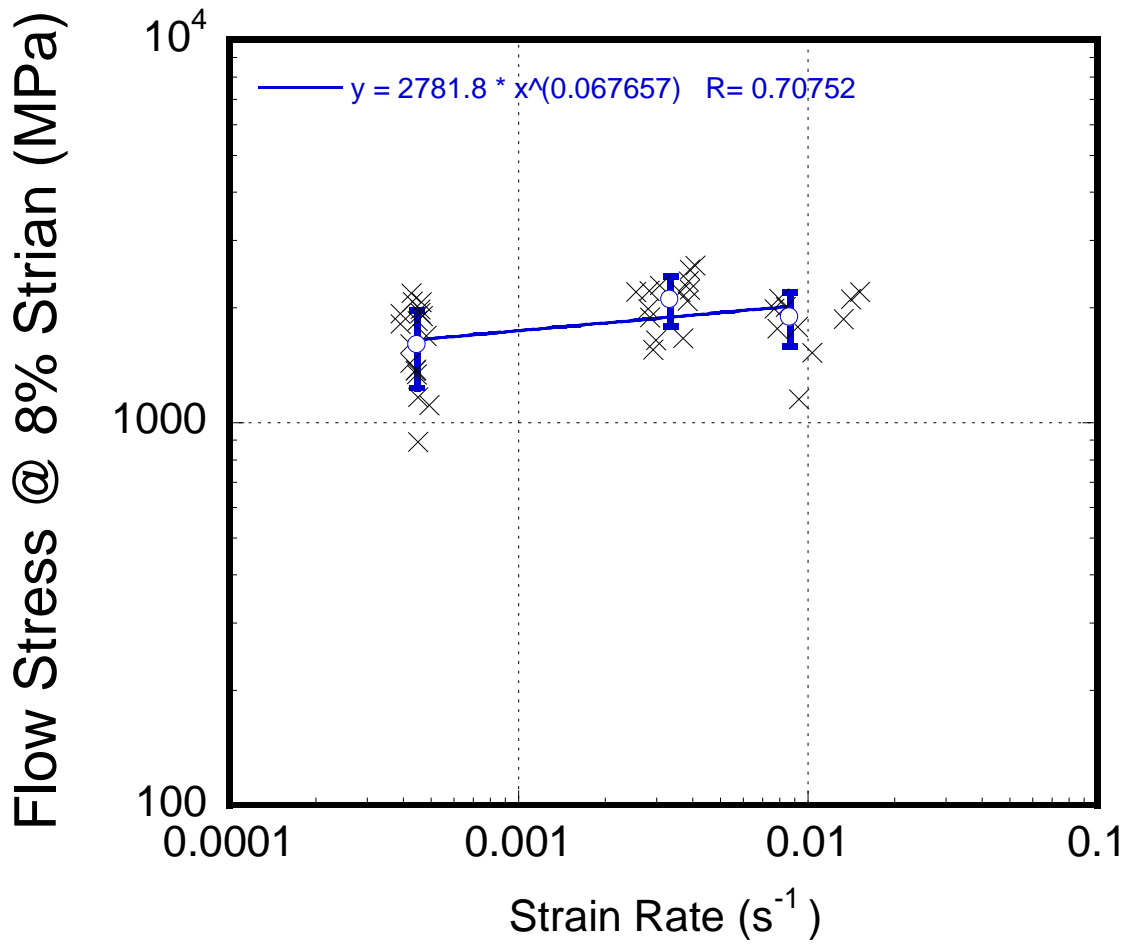


Figure 4.6: log-log plot of Flow Stress measured at 8% Strain for 550 nm Pd nanopillars as a function of strain rate. Strain rate sensitivity  $\sim m=0.68$

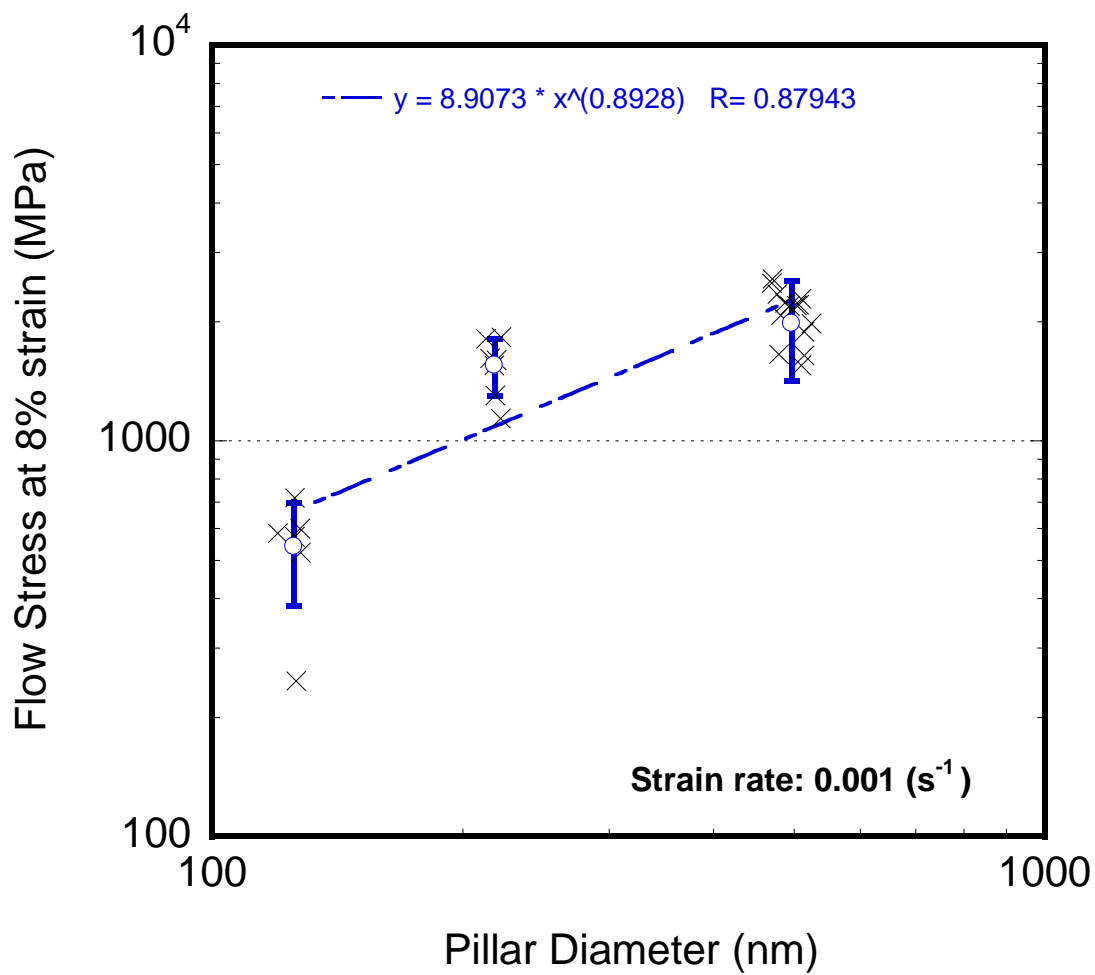


Figure 4.7: Log-log plot of engineering flow stress measured at 8.0 % engineering strain for 550 nm, 240 nm, and 120nm diameter Pd nanopyllars. The error bars indicate one standard deviation.

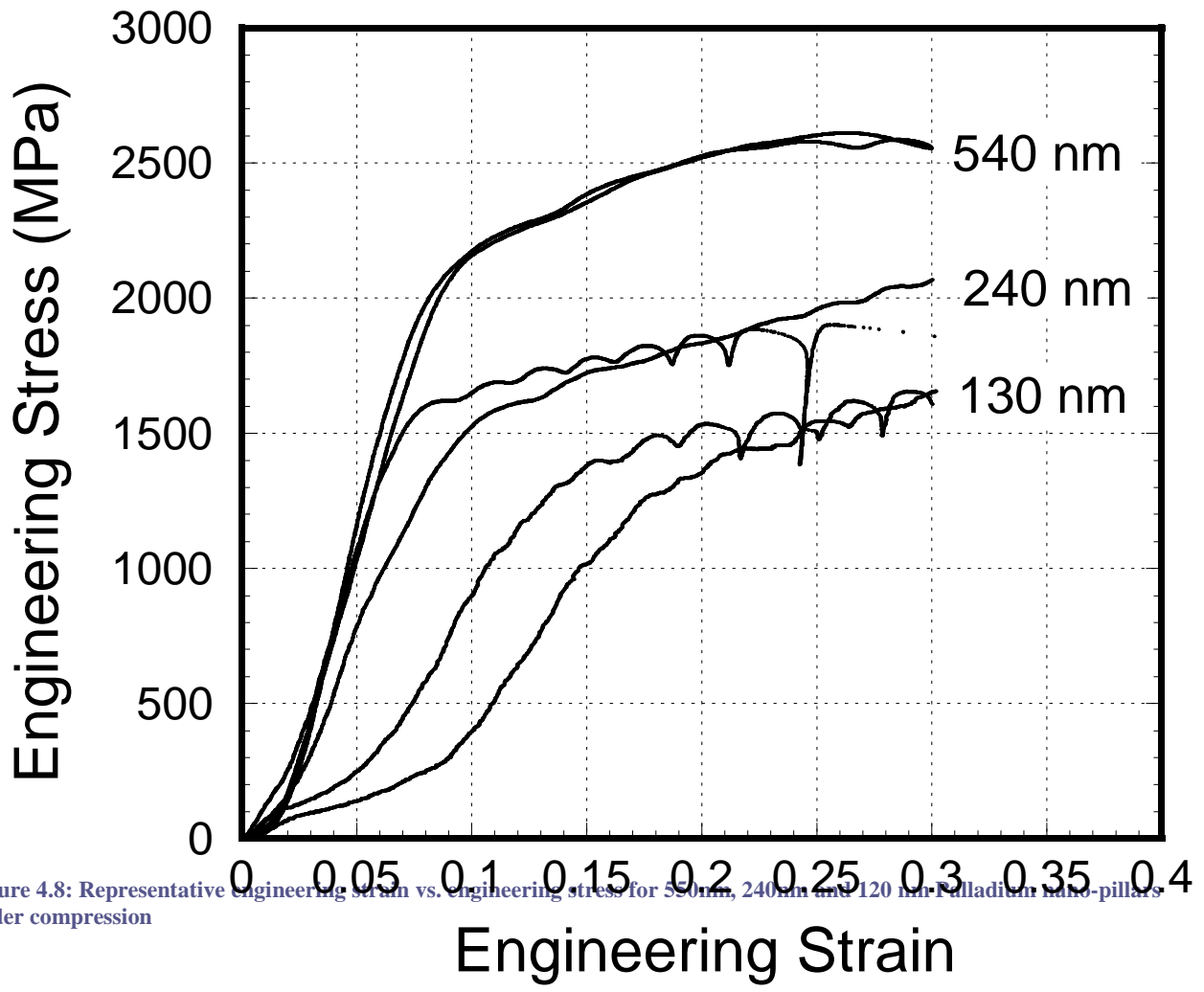


Figure 4.8: Representative Engineering Strain vs. Engineering stress for 540 nm, 240 nm and 120 nm Palladium nano-pillars under compression

#### 4.3.5 Conclusions and Recommendations

Incredibly high strength palladium nanopillars with nanocrystalline structures were fabricated and tested under uniaxial compression. The results showed that unlike the studied single crystal nano pillars under compression, palladium nanocrystalline metals show no increase in the flow stress of the pillars as the pillar dimensions gets smaller. In fact, an inverse size effect is seen where smaller pillars deform more easily and at lower stresses. Plastic buckling was severe even for shorter pillars with height to diameter aspect ratios of less than 3.

Since these palladium nanopillars exhibit high strengths, it is important to account for the errors that would be associated with the elastic deformation of the substrate prior to the start of the deformation of the pillar. This was less of an issue for low strength Sn and Bi nanopillars on gold substrate but should be considered for future studies on this material.

## Chapter 5: Indium Nanostructures: A Sophisticated Behavior under Micro-compression

### 5.1 Background

In this chapter, the mechanical properties of indium in sub-micron and nano-scale are studied under the uniaxial compression of indium nano pillars. Indium has a low melting temperature of 156°C corresponding to a homologous temperature of 0.7 in ambient conditions. At room temperature, indium crystallizes in the faced centered tetragonal (FCT) structure with  $c/a = 1.075$  which is only slightly different from that of an FCC structure [92]. There is evidence that at room temperature, the most densely packed planes are (001) and (101) [92].

Using the electroplating method, we were able to fabricate 1.25x1.25 mm arrays of pillars of diameters 0.12-1 $\mu$ m, each 10  $\mu$ m apart. Through tests on more than 200 pillars of each size, we were able to analyse the data with a great degree of confidence and we observed an inverse relationship between the pillar diameter and flow stress. Previous studies of indium nanopillars showed no size effect [33]; this can be due to the fact that the real region where the size effect becomes apparent was not reached in those studies [33]. This size effect was mainly seen in pillars of diameters less than 450nm. The strain rate dependency of the flow stress of the nanopillars was also studied as a function of pillar diameter by pillar compressions at 3 different strain rates.

In the study of materials in nanoscale, what is interesting is that in most of the materials tested, even at pillar sizes of less than 200nm, although a size effect is seen, the strength of the pillars are nowhere near theoretical strength even though it is highly unlikely of high dislocation populations to exist in such small volumes.

In the literature, only molybdenum pillars grown by directional solidification of an NiAl-Mo composite were seen to yield at shear stresses of  $G/26$  which is the range expected for theoretical strength ( $G/30$  to  $G/10$ ). In most studies, the test specimens were fabricated through FIB milling and even if the section of the bulk material from which the pillar was milled was dislocation free, near surface dislocations will be induced after the exposure to high energy Ga ions [4].

Here, we show that most pillars of sizes 240-140nm fabricated are either dislocation free and yield at theoretical strength, or become dislocation free during the compression test through a phenomenon known as “mechanical annealing”. This could be used to study the strengths required to deform a perfect indium single crystal.

## 5.2 Experimental Methods

Similar to Sn, Bi and Pd nanopillars presented in Chapters 2,3 and 4, indium nanopillars were fabricated using the EBL and electroplating technique. Electroplating was chosen as a replacement for the FIB methods used in previous works to eliminate surface damage effects, often associated with nanopillar fabrication techniques.

The final pillars were fabricated by the electrodeposition of indium metal into the hole pattern template. Prior to electrodeposition, the resist templates underwent a 15s oxygen plasma descum process at room temperature, 102 mTorr chamber pressure, an oxygen flow rate of 40 sccm and a plasma power of 20W using a reactive ion etcher at the University of Waterloo’s center for integrated RF engineering. This step was added to increase the hydrophilicity of the pore interior thereby increasing the homogeneity of the electroplating.

The electroplating process was performed using the conductive Ti/Au layer as the cathode, and a high purity indium metal slab as a soluble anode submerged in to a sulfamate based plating bath purchased from the Indium Corporation of America. The experiment was set up so that the cathode and anode were placed 1 inch apart, both submerged into 20 mL of the plating solution which was held at room temperature and was mechanically stirred during the process. The conditions for the electrodeposition was an initial  $10\text{mA}/\text{cm}^2$  current pulse for 3 seconds which created an indium seed layer, no more that 20% of the final pillar height. The current was then decreased to conduct the electroplating at  $1\text{mA}/\text{cm}^2$  for different plating times based on pillar diameter and desired height. Finally, the PMMA resist was etched off by soaking the samples in acetone for 30 minutes.

Using the above conditions, a yield of 100% was achieved for different sample sizes and the final chips

consisted of 15625 pillars located in a 125x125 square array with a distance of 10  $\mu\text{m}$  between pillars.

Four pillar sizes were fabricated using the above process, and the final pillar diameters were  $\sim 140\text{nm}$ ,  $\sim 240\text{nm}$ ,  $\sim 560\text{nm}$  and  $\sim 1070\text{nm}$ . Among these samples, several pillars were investigated using a scanning electron microscope and pillars with a uniform cylindrical structure and a diameter to height aspect ratio of  $\sim 2-3$  were selected and mapped for uniaxial compression tests. Based on simulation results by H. Zhang, this aspect ratio of  $\sim 2-3$  does not exhibit stress misreading due to plastic buckling. Elastic Euler buckling is also not a concern in these experiments since it will not occur even for soft pillars for aspect ratios below 25 [5]. The samples were annealed at room temperature for a period of 2 weeks prior to compression.

As in the case of Sn, Bi and Pd, the silicon chips with the pillar arrays were then mounted onto a flat stub using a lacquer; a lacquer was used in order to ensure that there is no lateral movement of the sample during the compression test and also to ensure the alignment of the pillars and the nano indenter. The compression tests were performed on a nanoindenter (NanoIndenter G200, Agilent Technologies Inc.) at the Nanomechanics Laboratory at the University of Waterloo. The indenter functioned at Dynamic Contact Mode (DCM) and was equipped with a custom made diamond  $8\mu\text{m} \times 8\mu\text{m}$  flat punch indenter tip. All pillar sizes were compressed uniaxially, at 3 different nominal engineering strain rates:  $0.01^{-1}$ ,  $0.001^{-1}$ ,  $0.0001^{-1}$ . This strain rate is defined by the ratio of the constant pillar length change (or displacement rate) to the initial pillar height. Note that the indenter controls the load with a proportional feedback control system, to keep the displacement rate constant. A proportional gain of  $6\text{e-}3$  was experimentally evaluated to optimize the control algorithm. The actual displacement versus time is plotted in figure 5.1 for data taken from the indenter for compression tests with constant displacement rates ranging from  $0.2 - 20 / \text{s}$  which shows a reliable control of the displacement rate by the indenter. The achievement of controller stability after a strain burst was key for indium compression tests where several strain bursts were seen.

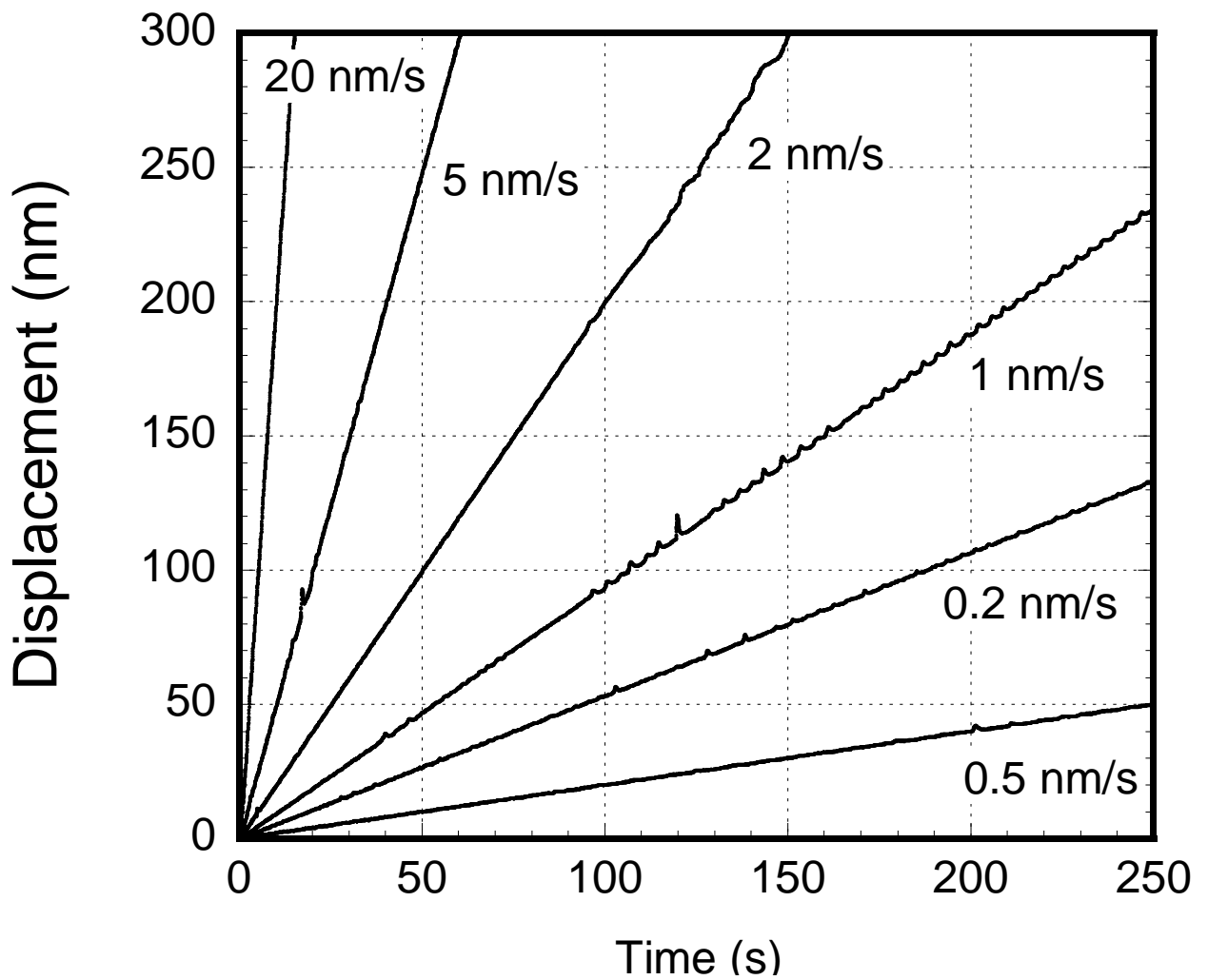


Figure 5.1: Time-Displacement plot showing constant displacement rates during the compression tests ranging between 0.2-20 nm/s

### 5.3 Results and Discussions

Figure 5.2 shows the final fabricated pillar with diameters ranging from  $0.14 - 1.07$ . Figure 5.3 shows a cross sectional FIB cut of these pillars indicating that these pillars are solid. The results of the compression tests were compared as the compressive flow stress of the nanopillars at 5% engineering strain for two strain rates. Previous studies of nanopillars present flow stresses at various engineering strains (ranging from 2 – 10%) [2]. When finding the value of strain at which the data was analyzed, we took into consideration the taper at the top of the pillars and found a saturation point on the stress strain curve for which the data could be trusted. The data extracted from 2-8% strain were plotted and compared (not presented here) and the data for  $\sim 4-8\%$  were within the plastic region for each pillar size and so 5% data was used for the analyses [2].

#### 5.3.1 Strain Rate sensitivity (Stress Exponent)

Figure 5.4 shows the average flow stress at 5% nominal strain at three different strain rates for various pillar sizes, where the error bars correspond to standard deviation. As seen in this plot, there is a clear relationship between the pillar compression strain rate, and the flow stress for all different pillar sizes. This relationship is seen in terms of an increase in pillar strength with an increase in strain rate. Generally, flow stress is known to be a function of strain rate and temperature. Previous nanoindentation creep experiments by Lucas and Oliver [93] on indium single crystals have shown a general relationship between strain rate ( $\dot{\epsilon}$ ) and stress ( $\sigma$ )

$$\dot{\epsilon} = K\sigma^n$$

Where  $K$  is a constant related to material properties (diffusivity and elastic modulus) and the power law exponent  $n$  is known as the stress exponent. This stress exponent is usually used to characterize the deformation behaviour or more specifically, the dynamic dislocation behaviour of the crystal [94].

To compare our results with previous bulk experiments on indium, the flow stresses at 5% strain in figure 5.4 were fitted separately for each pillar size using a power-law fit. As shown on the plot, the stress exponent calculated from the average data is  $\sim 4.7-5.5$  for different pillar sizes. This is very close to the

values measured from nanoindentation tests by Lucas and Oliver which shows a value of 5-7 for single crystal indium and falls in the range expected for dislocation creep [93].

J. Weertman also presents the creep rate of indium versus stress at various temperatures for a bulk indium sample [95]. His data for experiments at 301 – 304 *K* was extracted and plotted along with our data at room temperature ~295 *K* shown also on figure 5.3. The shift in stresses to the left of the x axis for our data indicates a clear size effect between the bulk data obtained by Weertman and our data starting at 1 $\mu$ .

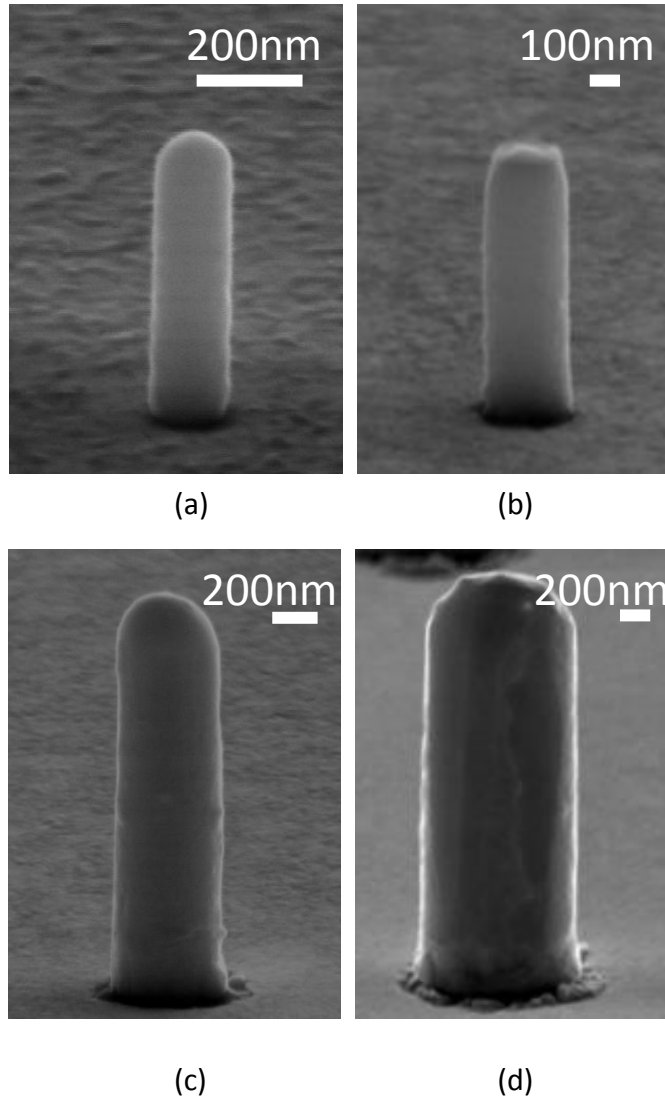


**Figure 5.2:** SEM images of Fabricated (a) 120 nm (b) 240 nm (c) 560 nm and (d) 1020 nm diameter indium nanopillar

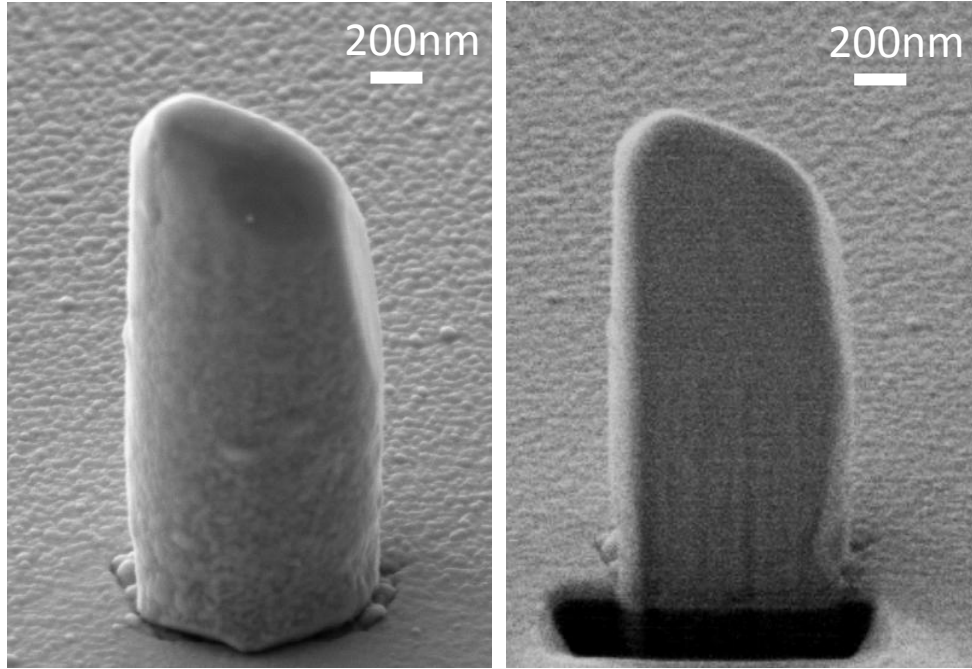


**Figure 5.3: FIB cross sectioned indium nano pillar (a proof of pillar solidity)**

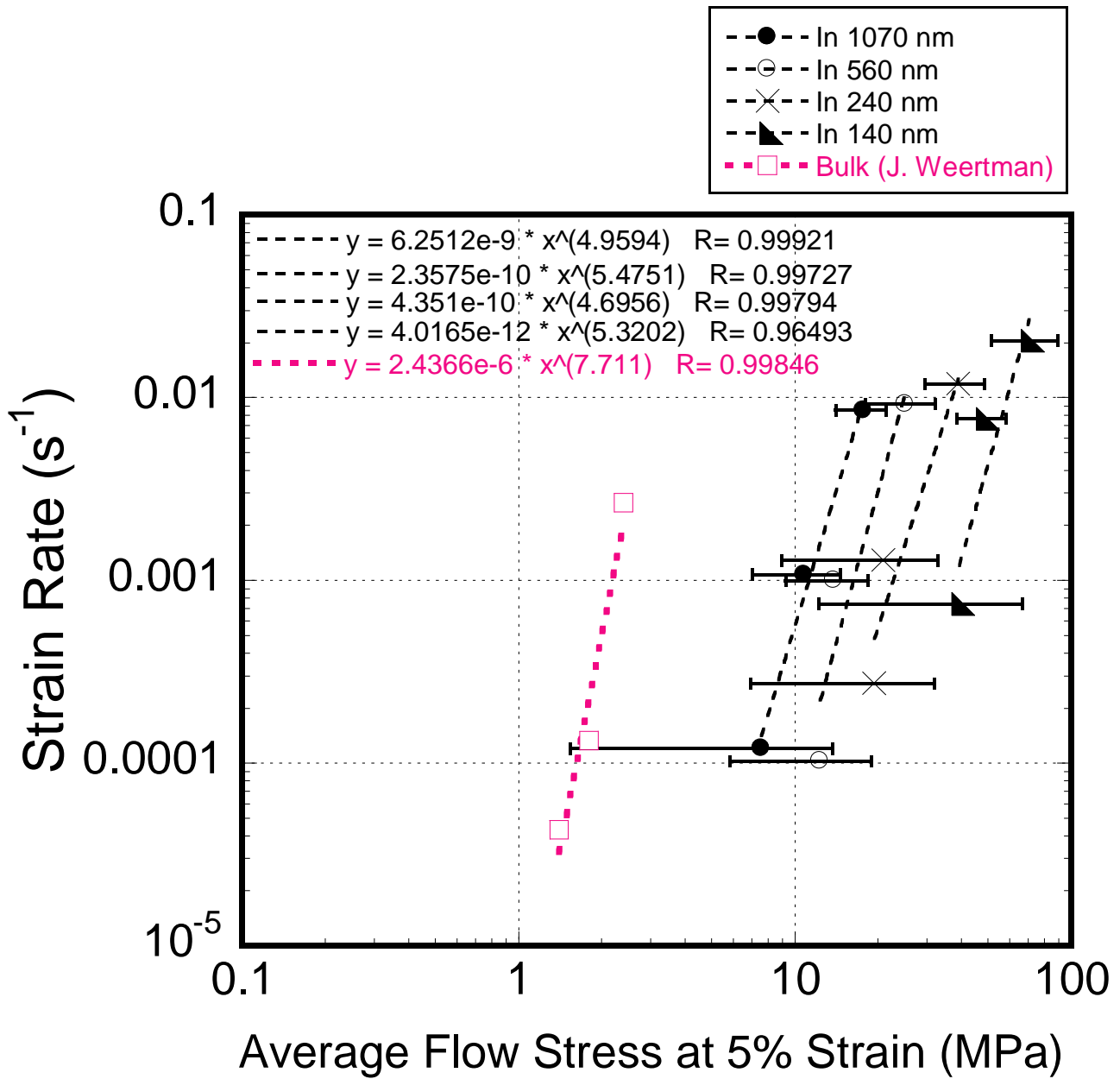


Figure 5.4: Strain rate as a function of Average flow stress at 5% strain for pillar diameters ranging from 140-1070nm- error bars correspond to standard deviation.

### 5.3.2 Size Effect

All studies on single-crystalline FIB-fabricated ([11]-[33]) and electroplated ([16], [23]) nanopillars have shown an inverse relationship between pillar diameter ( $D$ ) and flow stress ( $\sigma$ ). The data was fitted with a power law:

$$\sigma \propto D^{-\gamma}$$

According to a review by Uchic et al, other studies have shown a power law exponent of -0.61 to -0.97 for various FCC metals. Indium nanopillars showed a clear size effect when entering the range of pillars with diameters less than 450 nm. Various plots are presented to indicate this size effect. Figure 5.5 shows the flow stress at 5% strain for all pillar diameters at two strain rates; a significant difference in strength is seen between the 1.070  $\mu\text{m}$  and the 140nm pillars. The flow stresses at 5% strain for one strain rate  $0.01 \text{ s}^{-1}$  were plotted in Figure 5.6 (a) and a power-law fit was used to fit a curve through the average values of flow stress as a function of pillar diameter. This yielded a power law exponent of  $\sim\gamma = -0.55$  which indicates that indium shows a similar result to that of most single crystal FCC metals [2]. Figure 5.6 (b) shows a linear plot of flow stresses of indium nanopillars vs pillar diameter. Finally, representative stress-strain curves have been presented in figure 5.7 along with pre and post compression images in figure 5.8 (a)-(d) also showing this size effect.

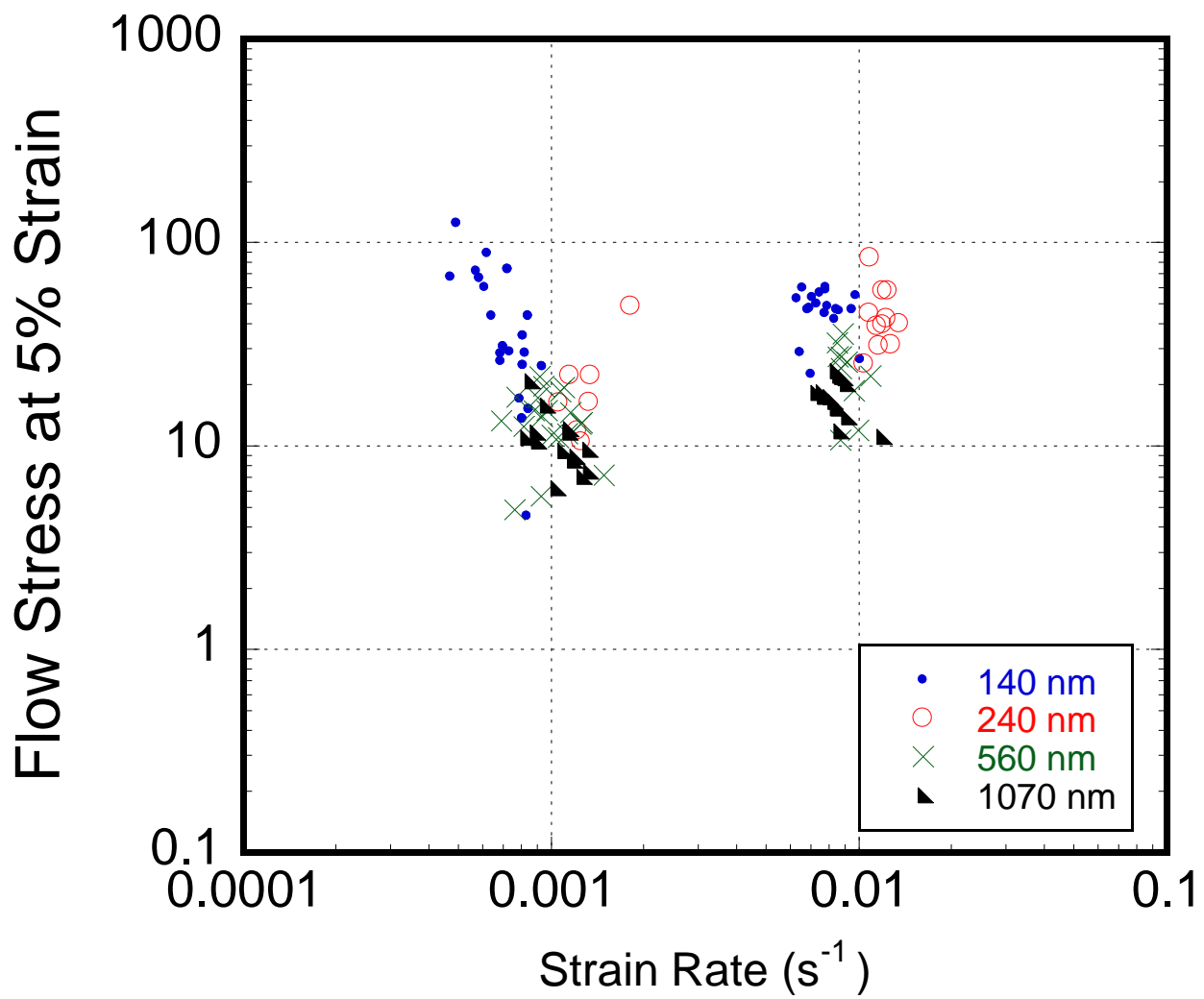


Figure 5.5: Flow Stresses measured at 5% Strain for two strain rates ( $\sim 0.001 \text{ s}^{-1}$  and  $\sim 0.01 \text{ s}^{-1}$ ) and pillar diameters ranging from 140-1070nm

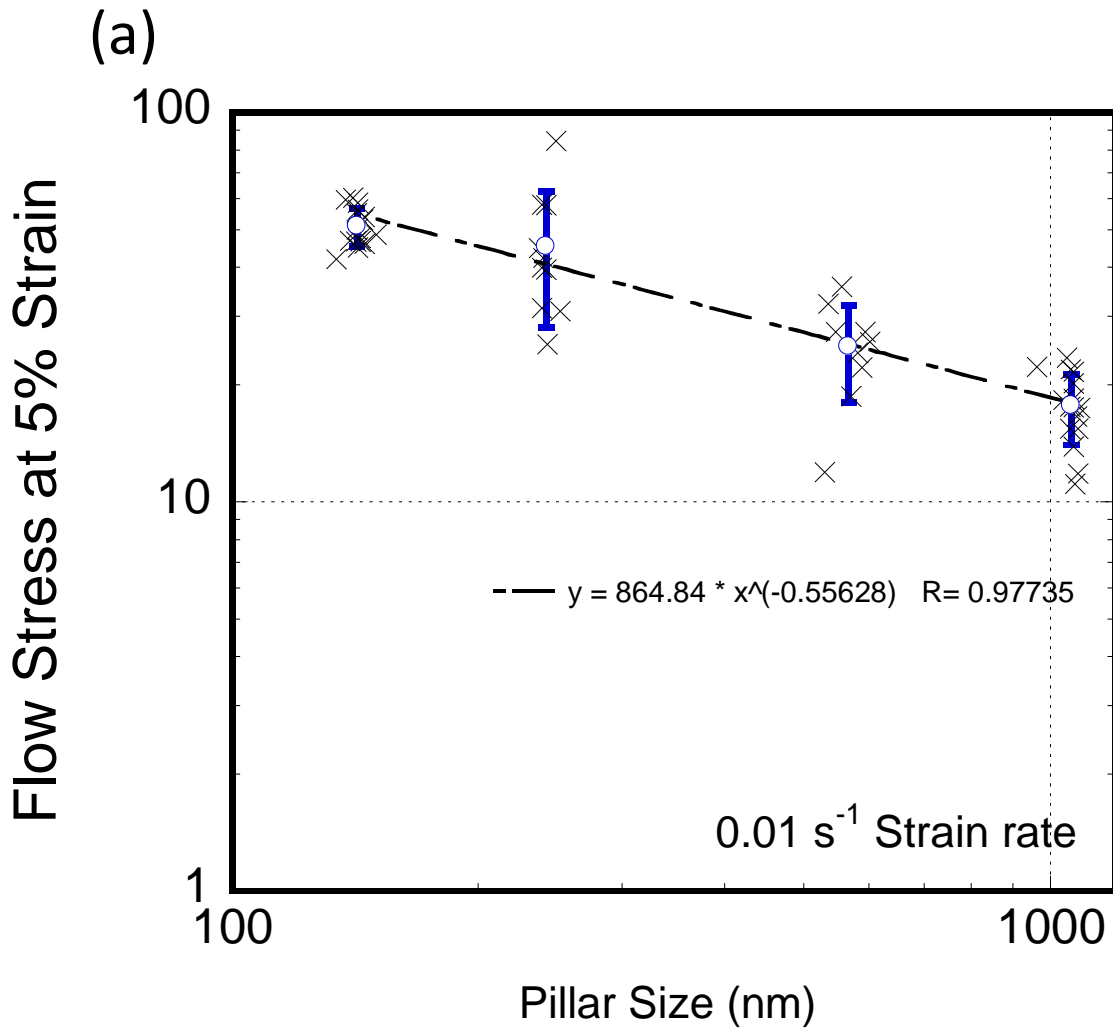


Figure 5.6: (a) log-log plot of Flow Stress at 5% Strain as a function of Pillar diameter (b) linear plot of Flow Stress at 5% Strain as a function of Pillar diameter

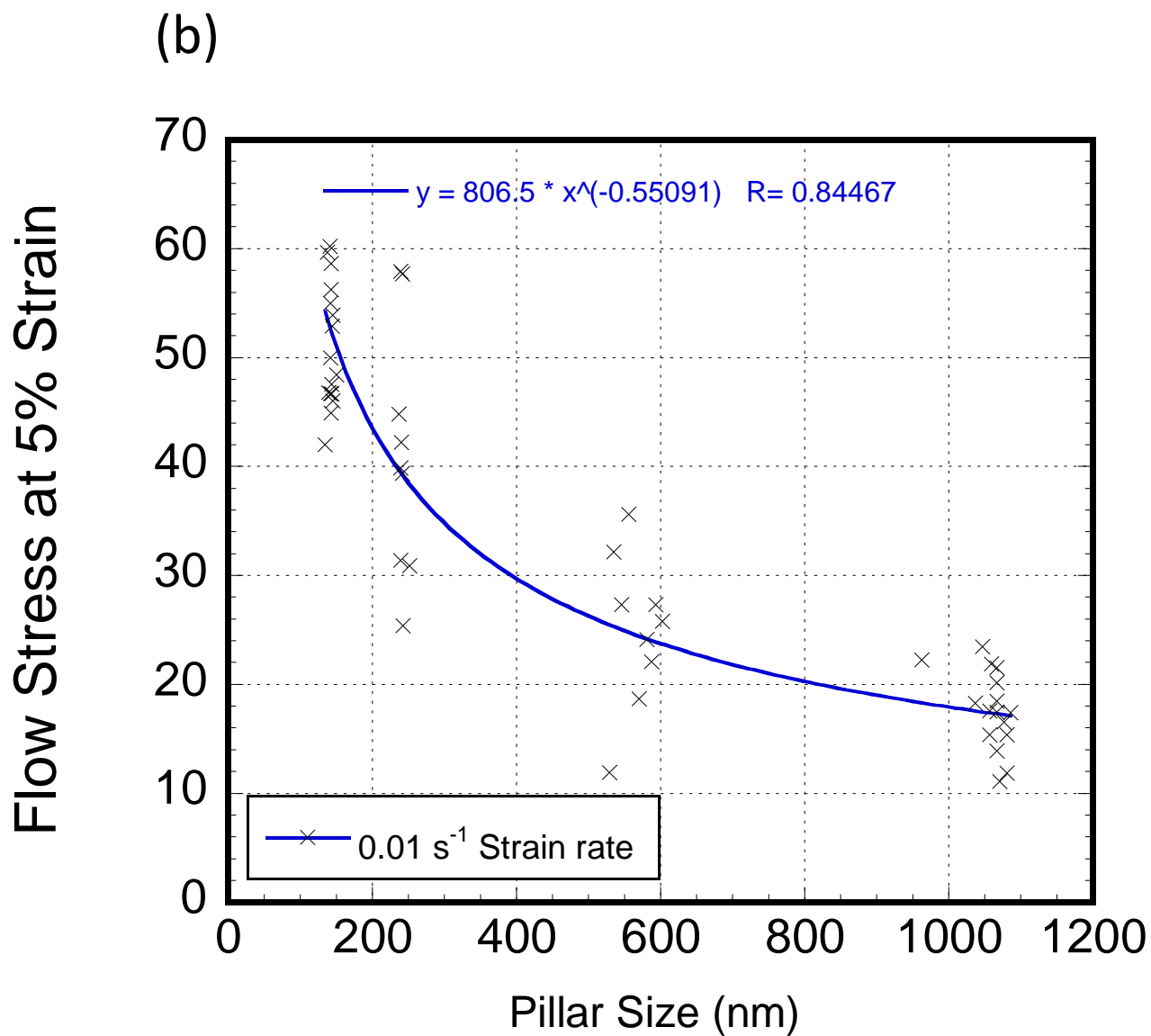


Figure 5.6: (a) log-log plot of flow stress at 5% strain as a function of Pillar diameter (b) linear plot of flow stress at 5% Strain as a function of Pillar diameter

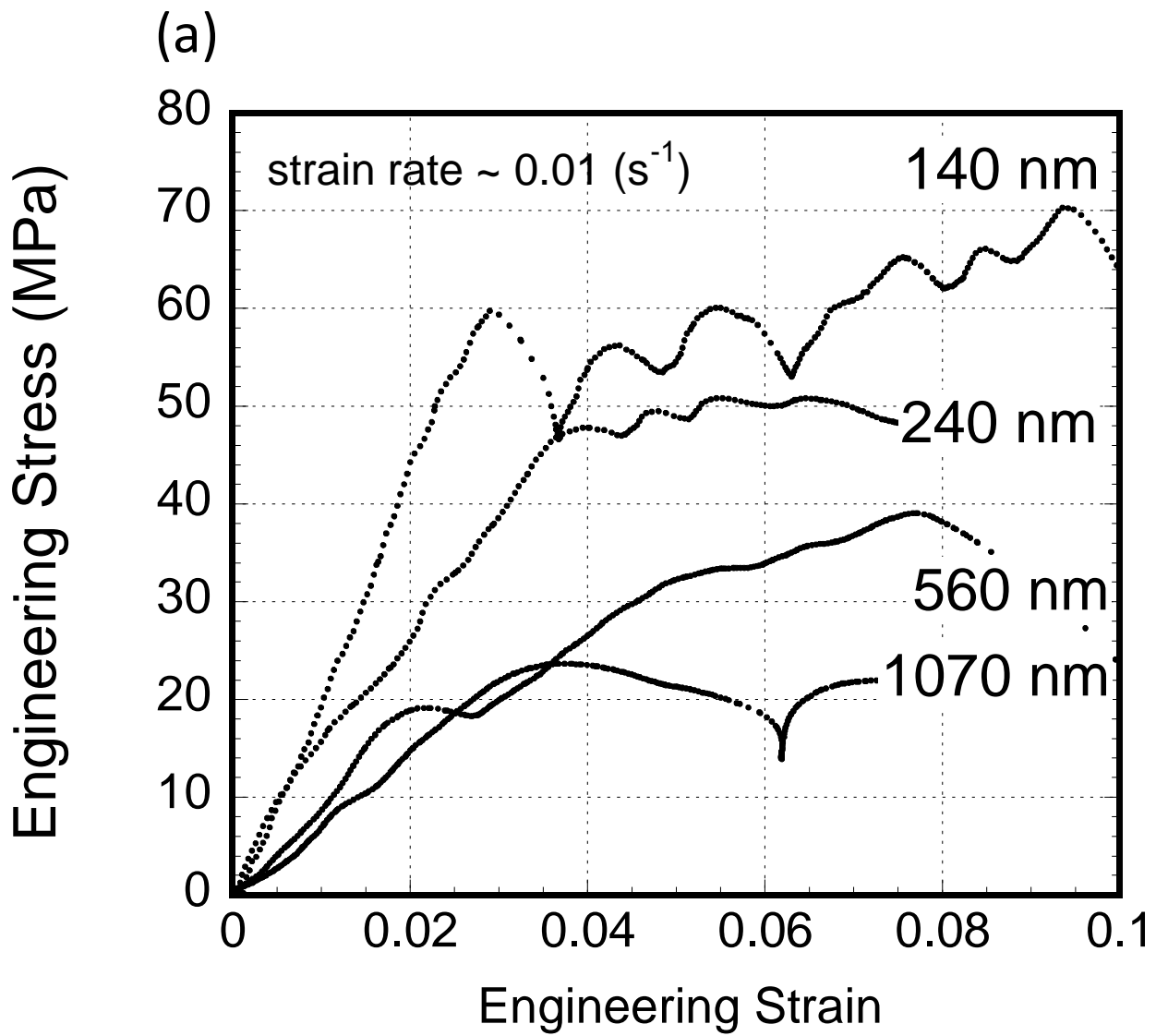


Figure 5.7: Engineering stress vs. engineering strain for 4 different pillar sizes

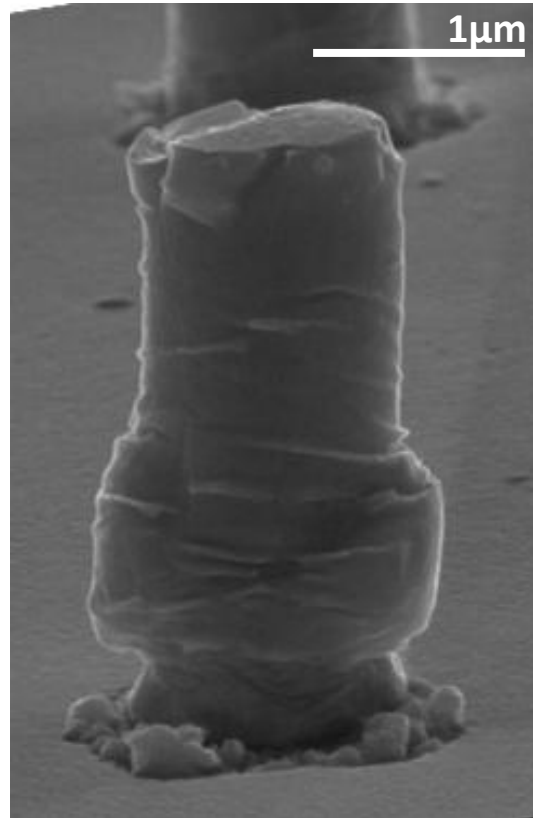
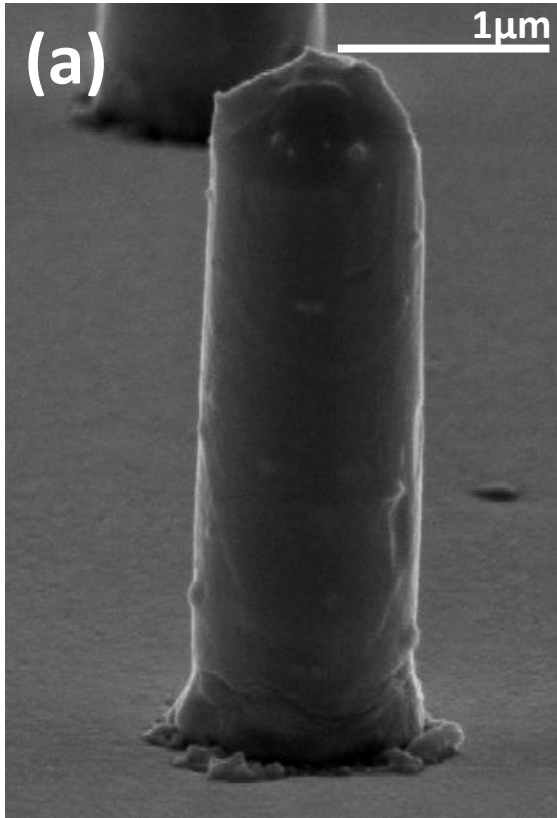


Figure 5.8: SEM images of (a) 1070 nm, (b) 560 nm, (c) 240 nm (d) 120 nm indium nanopillars before (left) and after (right) compression

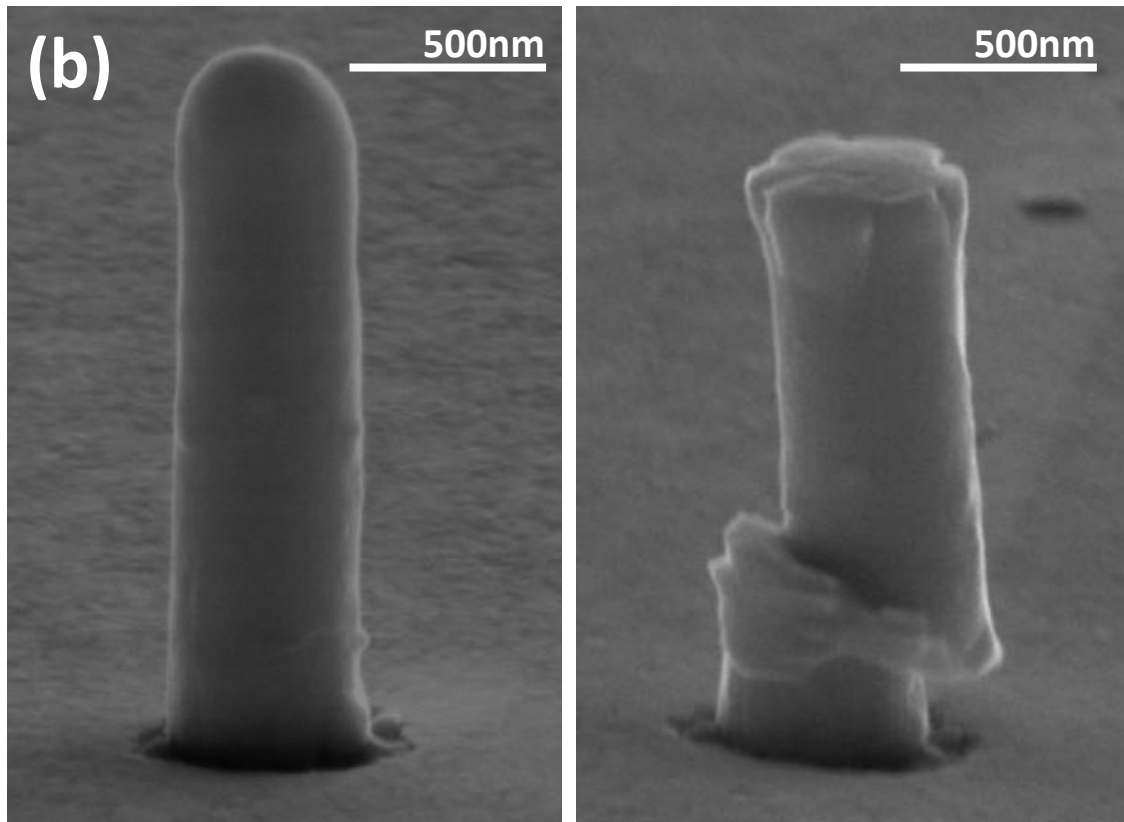


Figure 5.8: SEM images of (a) 1070 nm, (b) 560 nm, (c) 240 nm (d) 120 nm indium nanopillars before (left) and after (right) compression

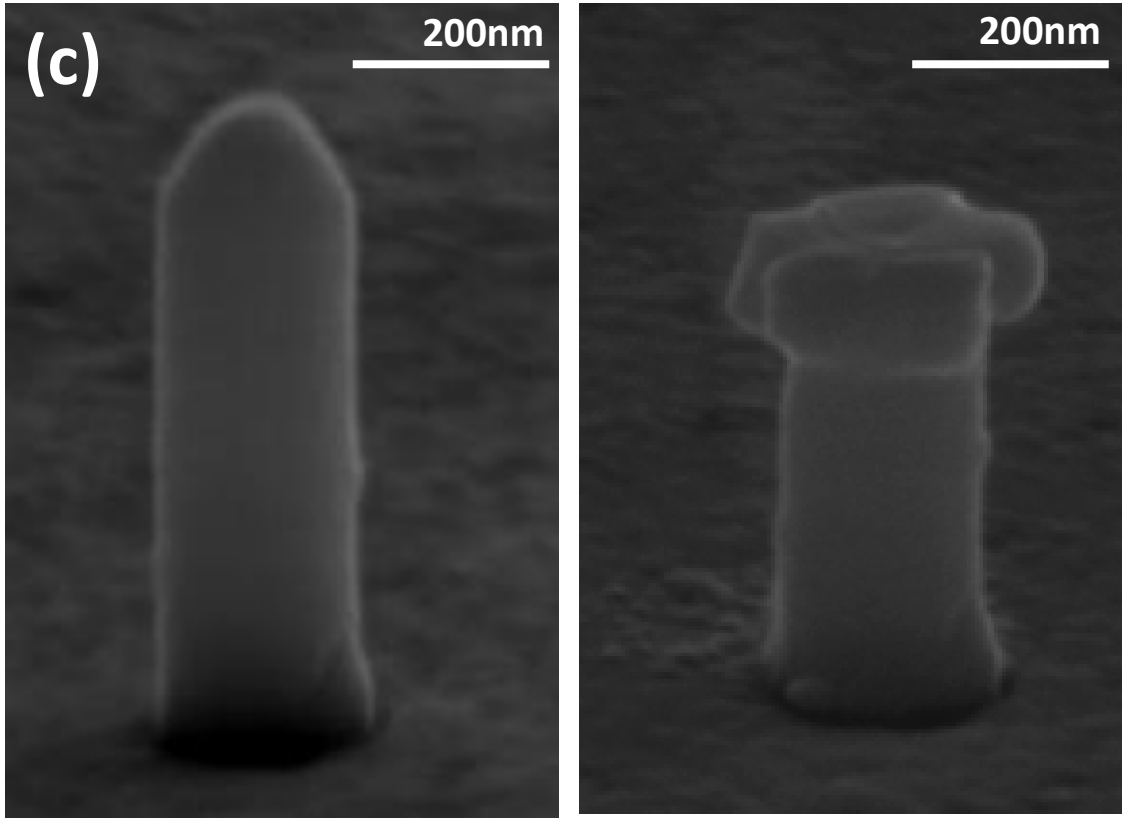


Figure 5.8: SEM images of (a) 1070 nm, (b) 560 nm, (c) 240 nm (d) 120 nm indium nanopillars before (left) and after (right) compression

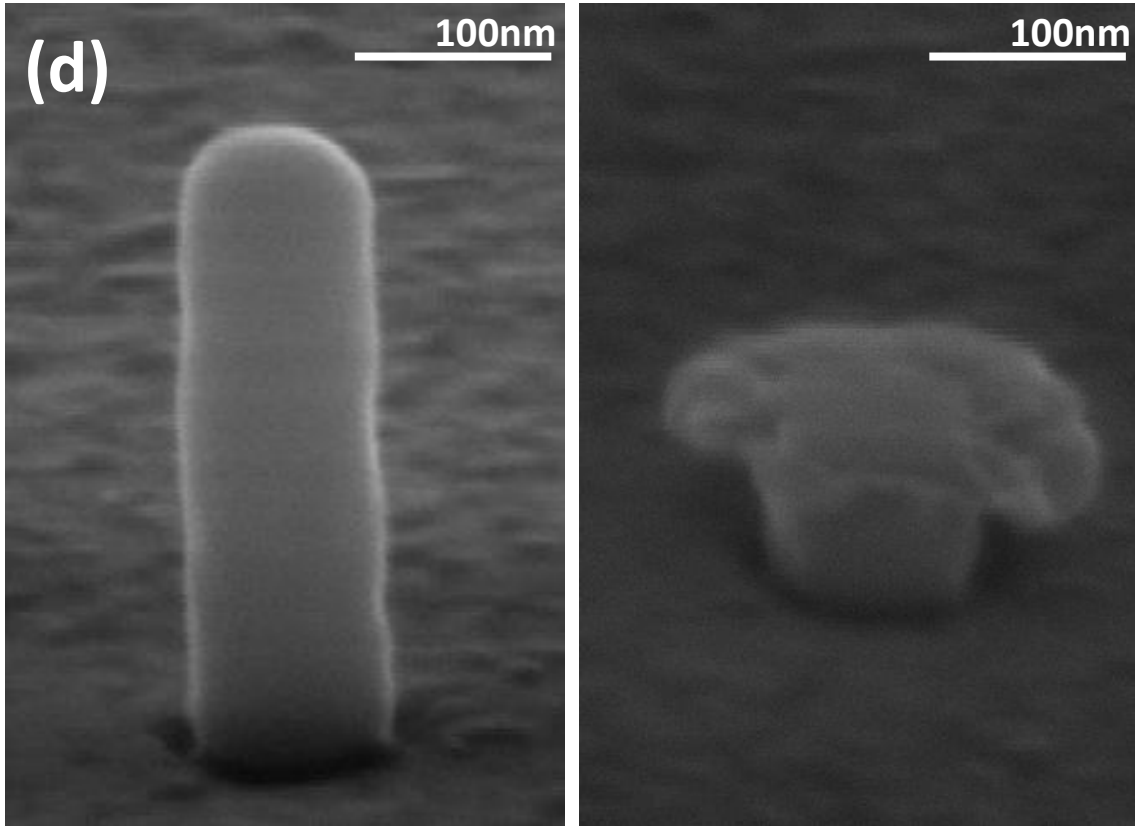


Figure 5.8: SEM images of (a) 1070 nm, (b) 560 nm, (c) 240 nm (d) 120 nm indium nanopillars before (left) and after (right) compression

### 5.3.3 Reaching Theoretical Strength

In addition to the size effect explained in the previous section, another size related strengthening is seen in the pillars. Some of the fabricated pillars underwent deformation at a very high strength close to theoretical strength. This was mostly seen in smaller pillars sizes (140 – 240nm). Figure 5.9 compares the engineering stress versus strain for two ~240nm indium pillars. These pillars were fabricated on the same substrate, all conditions, including plating conditions, annealing time, etc, were kept constant between the two pillars and the compression tests were done at a similar rate and on the same day. As seen in figure 5.9, one pillar attains a flow stress of ~363 MPa at 5% strain which corresponds to ~ 9.2% of the bulk shear modulus,  $G = 4.35 \text{ GPa}$  [33] and the other at 48 MPa which is about an order of magnitude lower. This indicates that the stress at which the first pillar deforms falls within the expected theoretical strength for metals ( $\sim G/30 - G/10$ ) [33]. Although there are no visible differences between the two pillars (Figure 5.10 (a) and (b)), previous microstructural characterization of indium nanopillars fabricated using this technique by the  $\mu\text{SXR}$ D technique shows that indium nanopillars which exhibit flow stresses approaching the theoretical value are pristine and do not contain any measurable initial dislocations [33]. In contrast, the low strength indium nanopillars are believed to contain a non-zero initial density of fabrication induced dislocations, resulting in their bulk-like attained strengths and strain rate sensitivity. Therefore, it can be said that the main factor that induces this type of size effect is the initial dislocation density. The pillar undergoing deformation is initially dislocation free and therefore it yields at a strength near theoretical.

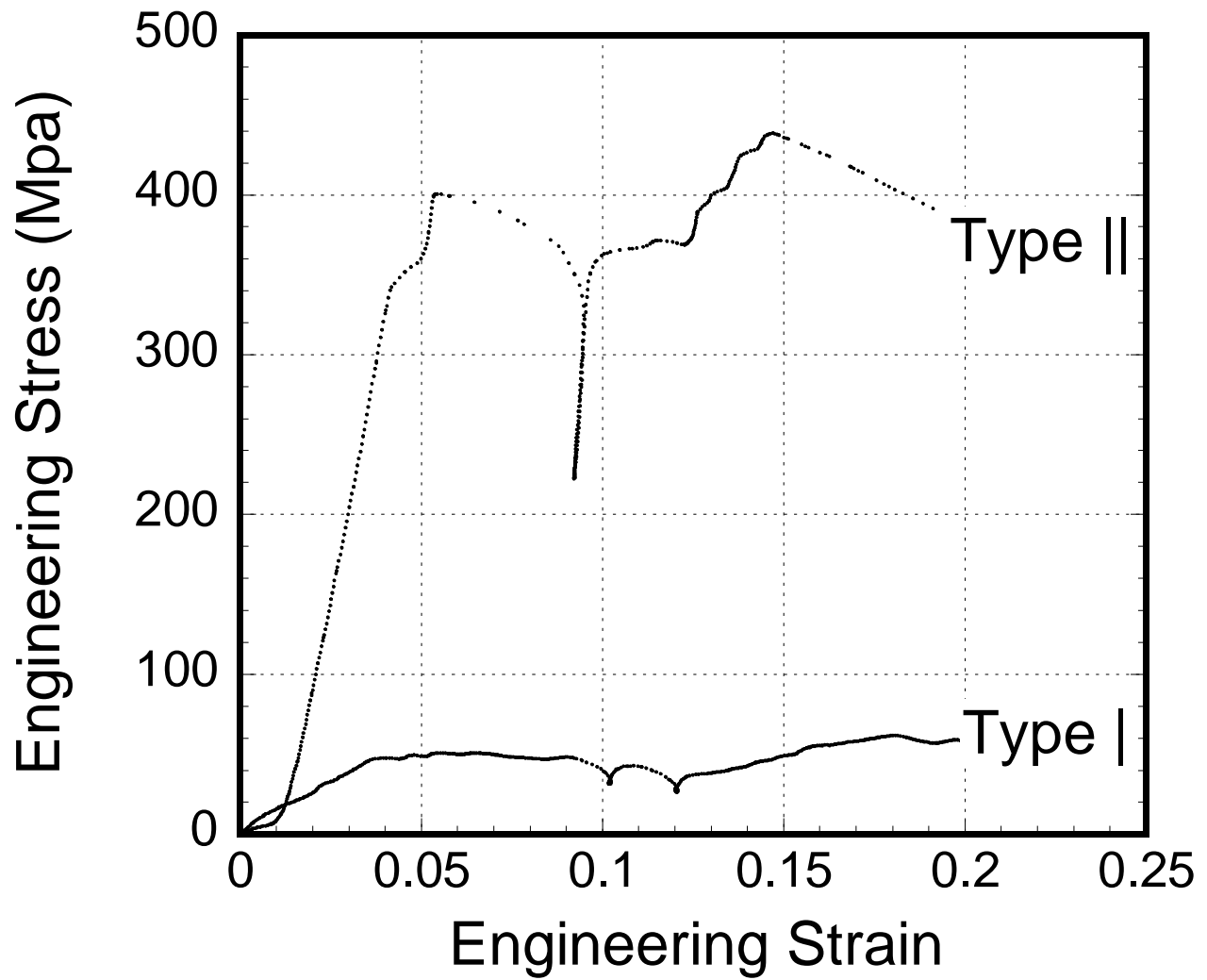


Figure 5.9: Engineering Strain vs. Engineering Stress for 240 nm Indium nano-pillars going through Type I and Type II deformation

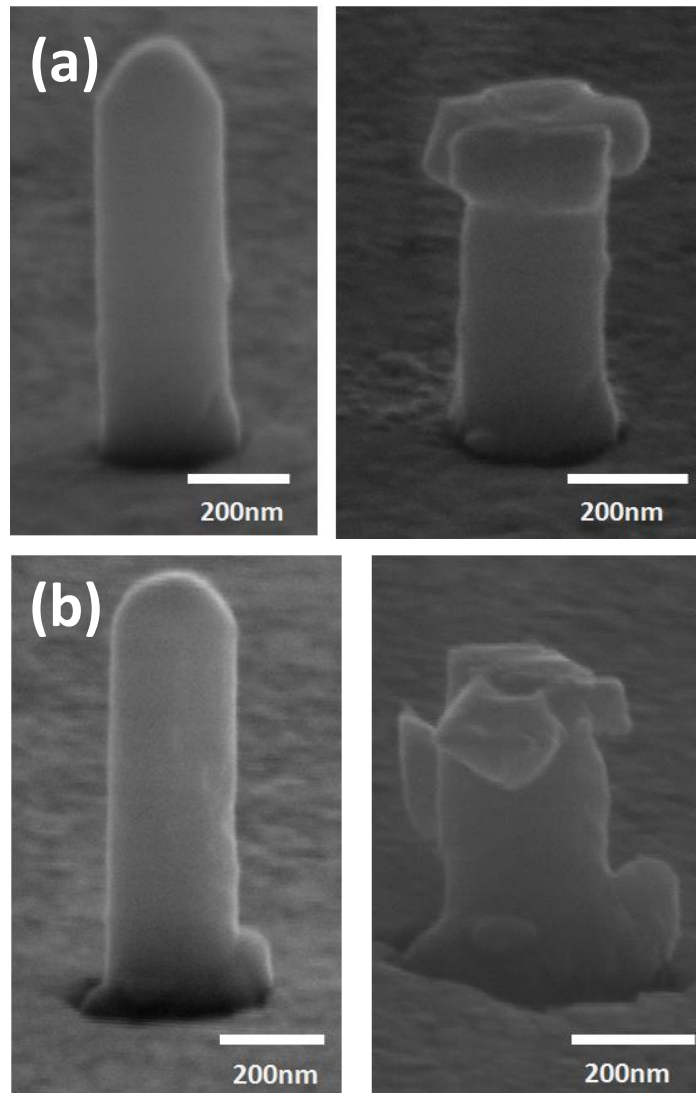


Figure 5.10: SEM images of 240 nm indium nano-pillars going through (a) Type I (b) and Type II deformation before (left) and after (right) compression

### 5.3.4 Mechanical Annealing (Dislocation Annihilation)

More high strength pillars were expected in the smaller sizes (<240nm). However, most of these pillars deformed in an extraordinary manner. As it can be seen in figure 5.11, the pillars seem to reach a very high stress value after a certain percentage of strain. This was seen in ~90% of the ~140nm and ~60% of the ~240nm pillars that were compressed. Some reached theoretical strength after 5-10% strain while others underwent more than 30% strain before reaching the theoretical strength. Figure 5.9 (a) shows two 240 nm indium nanopillars that deform at low load during the initial portion of the test but the load increases suddenly for both pillars, before 1% strain at points 1 shown on the figure, and the pillars start to deform under high strength followed by a crystallographic shear at point 2. The post compression SEM images in Figure 5.12(a)-(b) verify the final crystallographic shear of the pillars.

This behaviour is similar to that of Ni Crystals studied by Z.W. Shan (34) at the National Center for Electron Microscopy at Lawrence Berkely National Laboratory. In this study, they were able to directly observe the microstructural evolution of the pillars in relation to the mechanical data with a unique instrument which allows nano scale compression tests inside a Transmission Electron Microscope (TEM). They were able to perform and record *in situ* compression tests of Ni pillars with ~160 nm diameter and 850nm in length. By examining the recorded data, they observe a sharp increase in load, almost near theoretical strength. As it can be seen in figure 5.13 (c), after 170nm of compression, the pillar starts deforming at a much higher strength. Post TEM images shown in figure 5.13 (b) confirmed that the remaining portion of the pillar remained dislocation free [34].

Because of the damage that is caused by exposure to high energy ion or electron beams, it is not possible to perform such *in situ* tests on indium in order to confirm the results shown in figure 5.13 is in fact a vanishing of dislocations. But there are several evidences that can lead us to believe that this behaviour of indium is similar to that of Ni pillars, i.e. the pillars attain high stresses due to “mechanical annealing” in which the mere application of mechanical stresses results in the escape of dislocation.

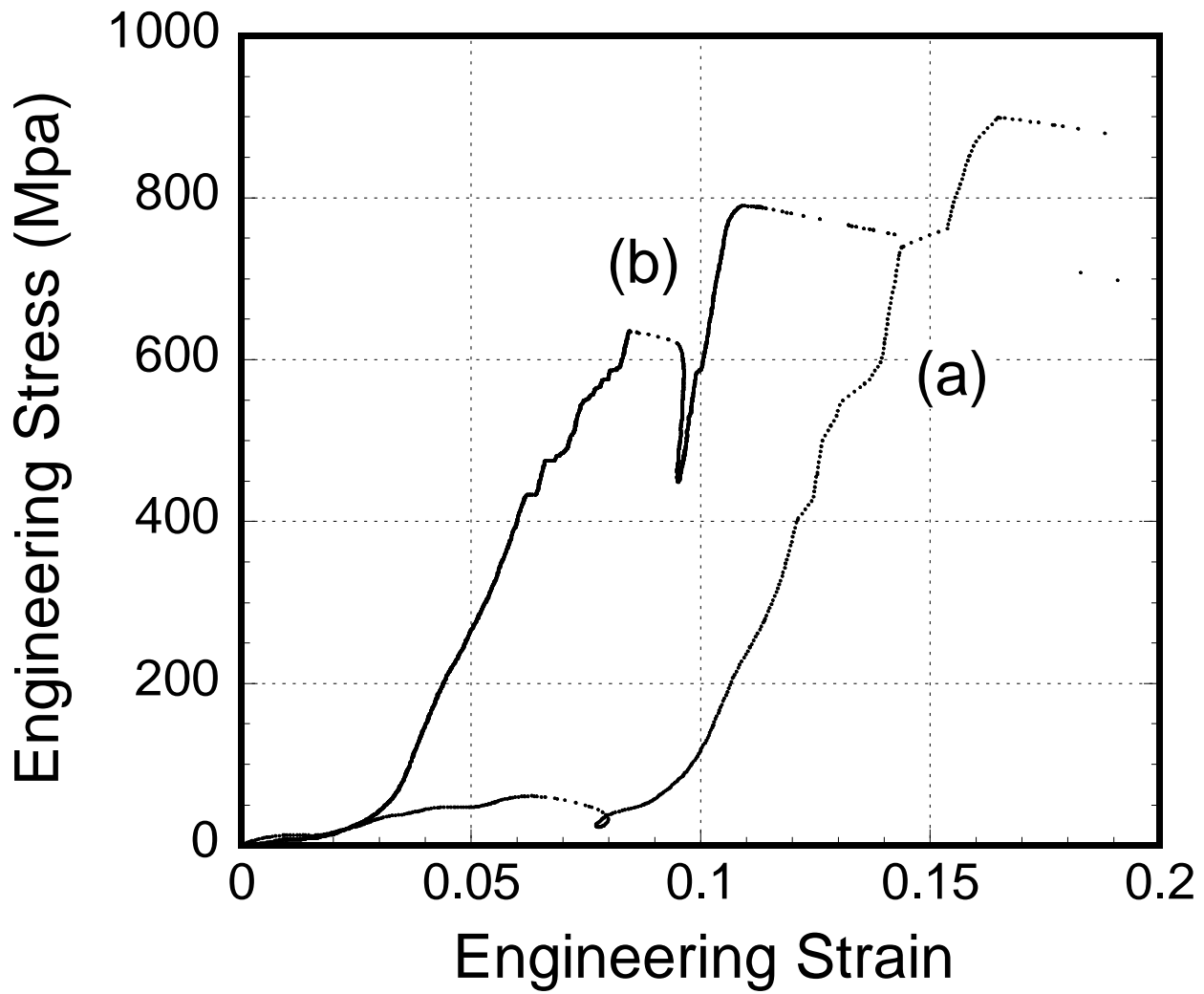


Figure 5.11: Engineering Strain vs. Engineering Stress for two ~240 nm Indium nano-pillars (shown in figure 5.12) going through Type III deformation

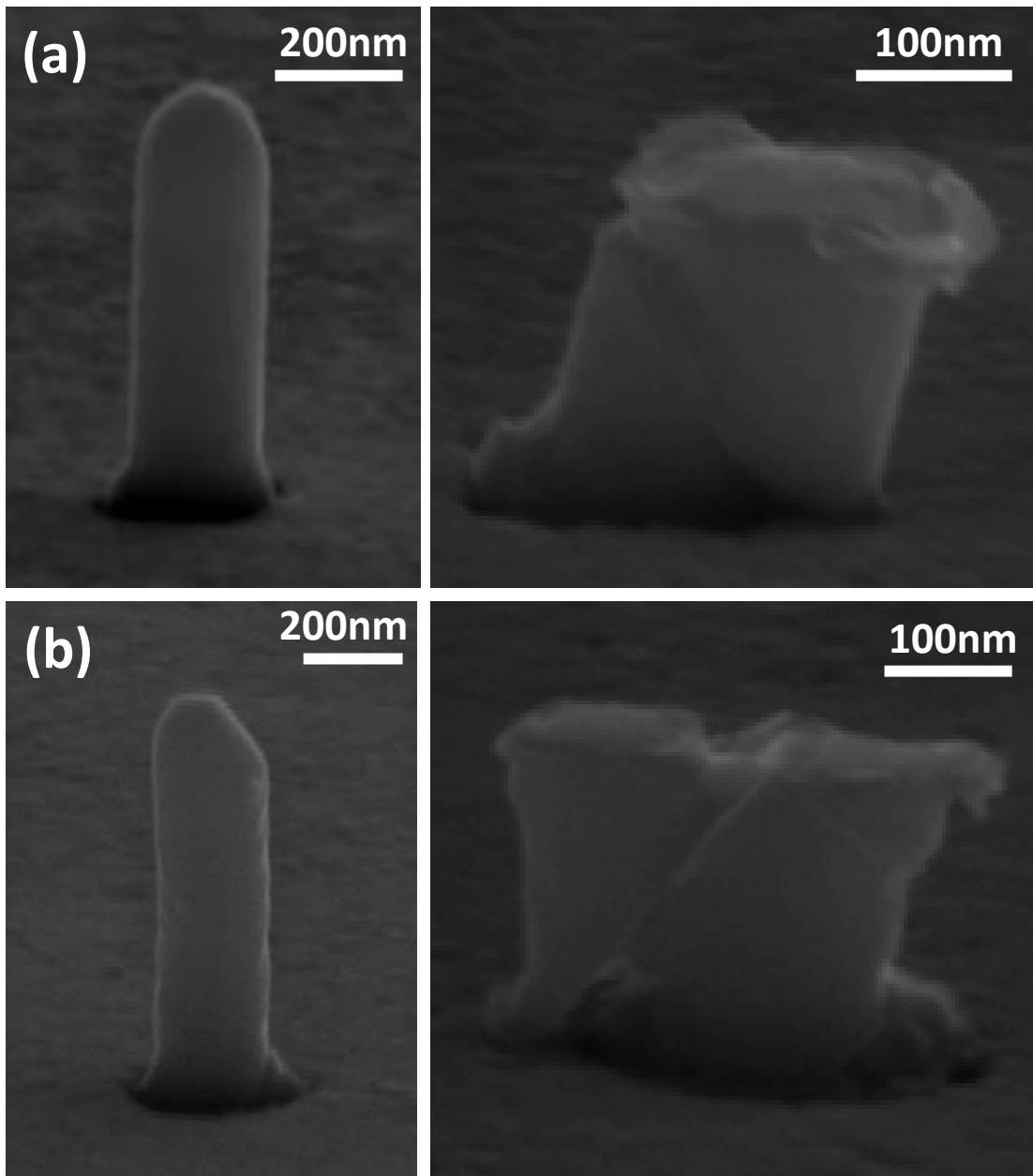


Figure 5.12: SEM images of ~240 nm indium nanopillars going through type III deformation before (left) and after (right) compression (stress-strain strain relations shown in figure 5.11)

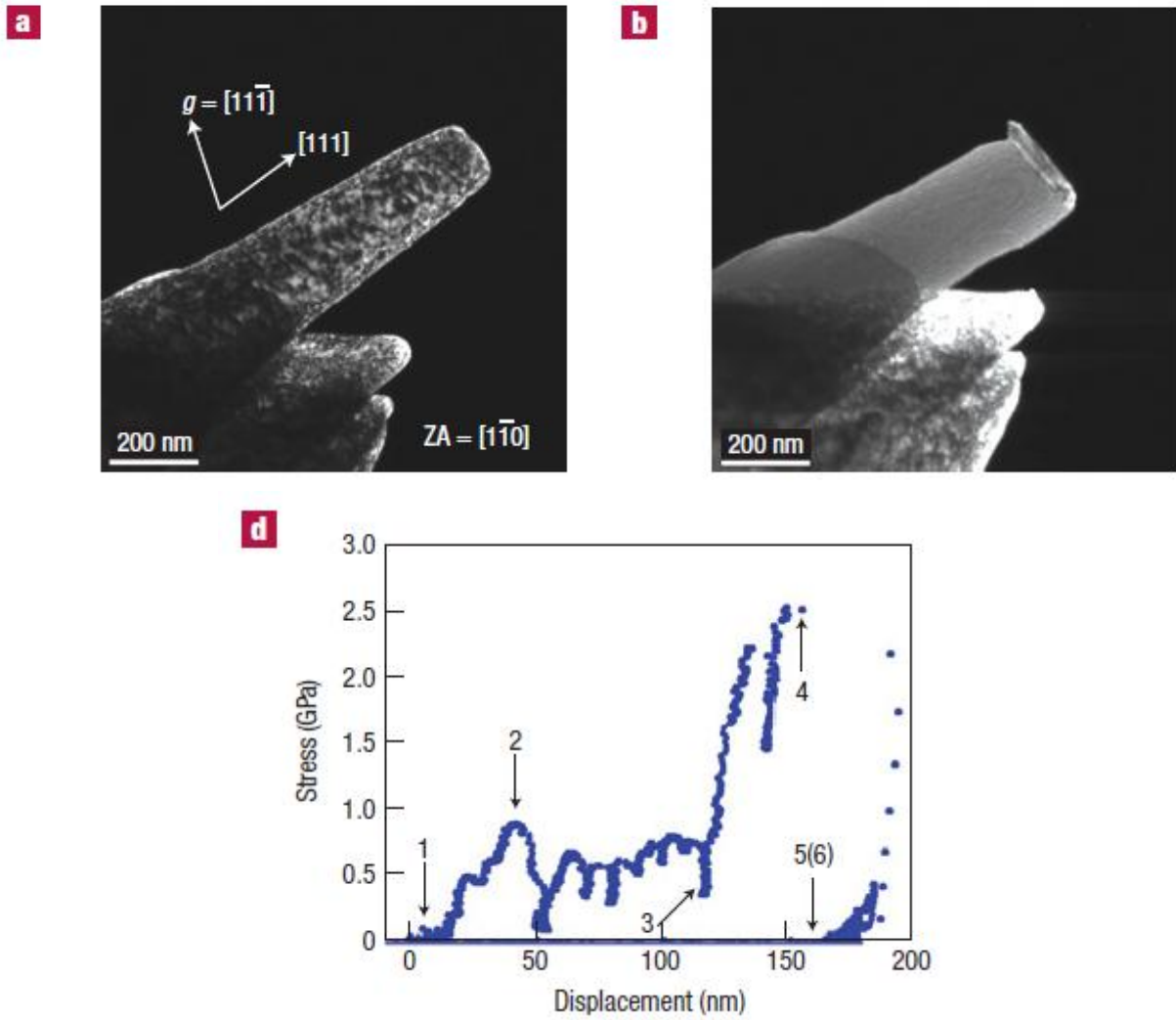


Figure 5.13: Ni single crystal nanopillars before (a) and after (b) compression and representative displacement vs stress curve (d)

## 5.4 Conclusions

In conclusion, fabricated indium nanopillars showed 3 types of size effects. First, among the pillars deforming at low stresses, a power-law exponent of  $\sim -0.55$  similar to that of most FCC single crystals was seen. The second type of pillars were pillars that deformed at strengths  $\sim 10$  times larger than the first group of pillars. These pillars are believed to be pristine crystals. Finally, the third type of pillars began their plastic deformation at low strengths but showed a drastic increase in flow stress and continued plastic deformation at strengths near theoretical. These pillars are believed to consist of very few dislocations which are forced out of the pillar by applying pure mechanical stress.

This phenomenon raises questions about the accuracy of compression of high strength FIB fabricated pillars. The substrate of these pillars is of the same material as the pillars but a dislocation free pillar is much harder than the bulk substrate and this can lead to a “sink in” of the pillar into the substrate. Shan et al. explain this as a “*hard spike punching into relatively soft ground*” [34]. The movement of the pillar into the bulk substrate in the case of high strength pillars can result in lower readings of the strength of the pillar. There have been attempts to correct for this plastic deformation, or deflection of the substrate [16] but the deformation might not be entirely plastic when the pillar is an order of magnitude stronger than the substrate it’s attached to. This sink in of the pillar was not seen in our experiments since an indium pillar at theoretical strength is still softer than the bulk silicon/gold substrate it is attached to.

## Chapter 6: Inelastic Buckling of Palladium, Cobalt and Rhodium Nanopillars

### 6.1 Introduction

Submicron and nanometer scale electroplated polycrystalline metallic structures are commonly used in microelectromechanical systems (MEMS) and nanoelectromechanical systems (NEMS) [96-98]. In many cases these devices, such as M/NEMS sensors, require components with large surface area to volume ratios in order to increase their sensitivity and overall performance. To achieve this, micron to nanometer scale metallic structures with high aspect ratios (length/width) are often employed. For example, Favier *et al.* [96] used palladium mesowire arrays to construct hydrogen gas sensors and switches, while another research group [97] fabricated metal resonators using rhodium. In MEMS packaging, small scale and high aspect ratio cobalt structures are used as heating components to assist solder bonding [98]. In order to design and fabricate mechanically robust M/NEMS devices, it is important to understand the deformation mechanisms of high aspect ratio nanostructures that they comprise of. Recently, as reviewed by Uchic *et al.* [99] and Greer *et al.* [100], it has been demonstrated that the mechanical properties of metals may be strongly dependent on the physical dimensions of the structures. Through uniaxial compression tests on a wide range of crystalline metals, such as, gold [101], molybdenum [102], tin [103], bismuth [104], and others [100], it was shown that the plastic flow stresses may increase significantly as the dimensions of the structures are reduced to the submicron and nanometer scales. This *smaller-is-stronger* size dependence in the strengths of metallic nanostructures has been well established through compression tests of metal columns with moderate length-to-radius aspect ratios, typically between 4 and 8. However, few studies have investigated the buckling behavior of polycrystalline metal nanostructures under uniaxial compressive stresses. Understanding failure by buckling in high aspect ratio metal nanostructures is ultimately vital in the design of reliable nanoscale devices, since they often consist of long slender components.

A common model to describe the bulk scale elastic buckling behaviors of high aspect ratio columns is Euler's formula, which relates the critical load of buckling ( $P_{cr}$ ) to the elastic modulus ( $E$ ) and the second

moment of inertia ( $I$ ):

$$P_{cr} = \frac{\pi EI}{(KL)^2} \quad (1)$$

where  $L$  is the length of the columnar structure and  $K$  is the boundary constraint factor. The moment of

inertia ( $I$ ) for a cylindrical structure with radius ( $r$ ) is  $\frac{(\pi r^4)}{4}$ . When the uniaxial load is greater than the critical value, any external disturbance to the structure may lead to a catastrophic failure via buckling. The Euler model performs well when the column length is significantly greater than the radius and the deformation is purely elastic. However, for intermediate-length columns, the buckling load deviates from the Euler model since the material may begin to buckle with applied stresses greater than the proportional limit. In order to predict this critical buckling load accurately for structures with smaller length-to-radius ratios, a tangent modulus method was developed by Engesser [105]. This method is an extension of the Euler model where the elastic modulus ( $E$ ) is substituted with the tangent modulus ( $E_t$ ) in Eq. (1). The tangent modulus is defined as the slope at any specific point on the uniaxial compression stress – strain curve. When the applied stress is less than the proportional limit, the tangent modulus has the value of the elastic modulus. However, tangent modulus becomes smaller beyond the proportional limit. Hsin *et al.* [106] extracted the elastic modulus of individual silicon nanowires by using uniaxial compression technique with an atomic force microscope cantilever beam. The lengths of these nanowires were hundreds of times larger than their respective radii. With the assumption of pure elastic buckling, they were able to extract the elastic properties of the nanowires. Chang *et al.* [107] also used the buckling technique to characterize the Young's modulus of long titanate nanowires fabricated by a hydrothermal process. To the best of our knowledge, there is no detailed study on the buckling behavior under uniaxial compression of individual polycrystalline metallic nanostructures.

In this chapter, a detailed study is performed in order to further understand catastrophic buckling failure

mechanisms of polycrystalline metallic cylindrical columns with diameters near 130 nm. The three materials selected for this work are palladium, cobalt, and rhodium, with elastic moduli of ~117 GPa [84], ~208 GPa [108], and 379 GPa [109], respectively. The columnar nanostructures were fabricated by an electron beam lithography and electroplating approach, and have final length-to-radius ratios in the range of 4 to 20. The electroplated nanopillars all possess fine grained microstructures with an average grain sizes less than 100 nm. As such, the fabricated nanostructures are considered polycrystalline. Through uniaxial compression in a nanoindenter outfitted with a flat diamond tip, the tangential moduli of these materials were extracted from the measured buckling load results through use of Eq. (1). The calculated results are slightly smaller than with the bulk elastic moduli. In addition to characterization of the critical loads for buckling failure, this study also investigates the ductility of these metallic nanostructures. Inspections of the failed specimens by scanning electron microscopy (SEM) revealed that the cobalt and rhodium samples exhibit fracture near the middle of the column after buckling. In contrast, palladium specimens did not fracture even though they were plastically deformed with strain greater than ~ 24 %.

## **6.2 Experimental Methods**

### **6.2.1 Electron Beam Lithography Process**

Palladium, cobalt, and rhodium nanopillars were fabricated using similar electron beam lithography and metal electroplating methods presented in the previous chapters [110]. A schematic drawing of the processing steps is illustrated in Figure 2.1. In comparison to conventional focused ion beam (FIB) milling of small scale metal columns for mechanical tests, the nanopillars prepared in this study are free of artefacts generated through high energy Ga<sup>+</sup> ion exposure. Additionally, smaller specimens (< 200 nm diameter) are produced with virtually no tapering, which allows for the generation of high aspect ratio structures. Silicon substrates with [111] out-of-plane orientation were coated by electron beam evaporation with a 20 nm thick titanium adhesion layer followed by a 100 nm thick gold layer. The substrates were then spin coated with a 1 μm thick layer of 950 kD polymethylmethacrylate (PMMA,

MicroChem Corp.) electron beam lithography resist. A Leica EBPG 5000+ electron beam lithography system operating with a 100 kV acceleration voltage was used to pattern an array of 130 nm diameter holes. Following the exposure, the PMMA resist was developed for 60 seconds with a 1:3 solution of methylisobutylketone and isopropyl alcohol. The prepared wafer was diced into square  $\sim 1 \text{ cm}^2$  chips with the patterned PMMA resist template in the chip center before electroplating.

### 6.2.2 Nano-pillar Electroplating

Galvanostatic electroplating technique was used to deposit palladium, cobalt, and rhodium into the patterned PMMA resist templates. The palladium tetrammine (II) chloride based electroplating solutions were manufactured by Technology Without Limits (West Warwick, RI) while the rhodium plating solution was provided by Krohn Industries Inc. (Carlstadt, NJ). During deposition, the palladium and rhodium electroplating solutions were maintained at room temperature and  $\sim 40 \text{ }^\circ\text{C}$ , respectively. The cobalt electroplating solution was prepared in house with ultrapure water and contained 0.2 M cobalt (II) sulphate heptahydrate ( $\text{CoSO}_4 \cdot 7\text{H}_2\text{O}$ , 98 % purity, Alfa Aesar) and 0.1 M boric acid ( $\text{H}_3\text{BO}_3$ , 98 % purity, VWR). The pH of the cobalt electroplating solution was adjusted close to 6 using a 1.0 M NaOH. In all cases, the gold/titanium seed layer underneath the PMMA resist template acted as the cathode. A Teflon backing and custom gold coated clips were used to mount the PMMA coated substrates in the solution and electrically interface with the gold/titanium cathode layer. A platinized titanium mesh (Stan Robinstein Associate Inc.) was used as the anode for both palladium and rhodium electroplating, while a 5 mm diameter cobalt rod (99.95% purity, Alfa Aesar) was used as a soluble anode for cobalt electroplating. In all cases, both electrodes were submerged approximately 3 cm into 200 mL of the plating solution and separated by roughly 2.5 cm from each other. The total cathode area, which included the patterned PMMA coated substrate, a blank  $1 \text{ cm}^2$  gold/titanium coated silicon wafer chip, and the gold clips was maintained at  $\sim 3.5 \text{ cm}^2$ . For the palladium, cobalt, and rhodium electroplating processes,

a constant current density value of 18 mA/cm<sup>2</sup>, 2.2 mA/cm<sup>2</sup>, and 9 mA/cm<sup>2</sup> was maintained, respectively. The deposition times were adjusted according to the desired nanopillar height. After electroplating, the PMMA resist was removed with acetone.

The as-fabricated microstructures of a 1000 nm diameter palladium and 500 nm diameter cobalt nanopillars were characterized by transmission electron microscopy (TEM) and electron diffraction measurements. Larger nanopillar specimens were selected for TEM analysis due to the difficulty preparing thin TEM samples from smaller 130 nm diameter specimens. These larger pillars were prepared by an identical electron beam lithography and electroplating method as describe above, but with a larger circular opening in the PMMA resist template. The nanopillars selected for TEM analysis were cross-sectioned using standard FIB techniques for TEM sample preparation. The sample preparation and TEM imaging were conducted at the Canadian Centre for Electron Microscopy at McMaster University in Hamilton, ON, Canada. To avoid Ga<sup>+</sup> ion induced microstructural damage during the various FIB milling processes, the nanopillars were first coated with thick protective carbon layers by electron beam assisted and ion beam assisted deposition techniques. After FIB cross-sectioning, samples were lifted out of the substrate and transferred to a TEM lift-out grid using a micromanipulator and standard lift-out methodology. A FEI Titan 80-300 TEM operated at 300 kV was used to perform imaging and electron diffraction measurements on the cross-sectioned nanopillars.

### **6.2.3 Uniaxial Compression Testing**

An in-situ nanoindenter (Nanomechanics Inc, Knoxville, TN, USA) equipped with a custom 8 x 8 μm<sup>2</sup> diamond flat punch tip was used for the uniaxial compression testing of electroplated palladium, cobalt, and rhodium nanopillars. The as-fabricated nanopillars were inspected by scanning electron microscopy (SEM) prior to mechanical testing. A deformation rate of 1 nm/s was selected for all specimens compressed in this work.

## 6.3 Results and Discussions

### 6.3.1 Nanopillar Geometry and Microstructure

The geometry, surface topography, and microstructures of as-fabricated nanopillars were analyzed using high resolution SEM and TEM. Figures 6.1(a) to (c) show representative SEM micrographs of electroplated 130 nm diameter palladium, cobalt, and rhodium specimens. The nanostructures shown in Figure 6.1 all have similar length-to-radius ratios near 10. In all of the structures, the side walls are relatively smooth and do not possess any voids or pores. The columns are oriented near perfectly normal to the substrate and, unlike nanopillars produced by conventional FIB milling, there is virtually no tapering present. The uniformity in radius throughout the nanopillar length is a critical feature for specimens tested in this work in order to prevent stress concentrations which may lead to premature catastrophic failure. Figures 6.2 (a) and (b) show dark field TEM images of 500 nm diameter palladium and 1050 nm diameter cobalt nanopillars respectively. The TEM analysis reveals that the as-fabricated nanopillars are solid and without any internal voids. The electron diffraction patterns collected from these two specimens confirms that the electroplating conditions produce a polycrystalline microstructure. A high-resolution SEM micrograph of a 1050 nm diameter rhodium nanopillar is shown in Figure 6.2 (c). This image clearly indicates that the electroplated rhodium is also polycrystalline with grains that are smaller than 100 nm.

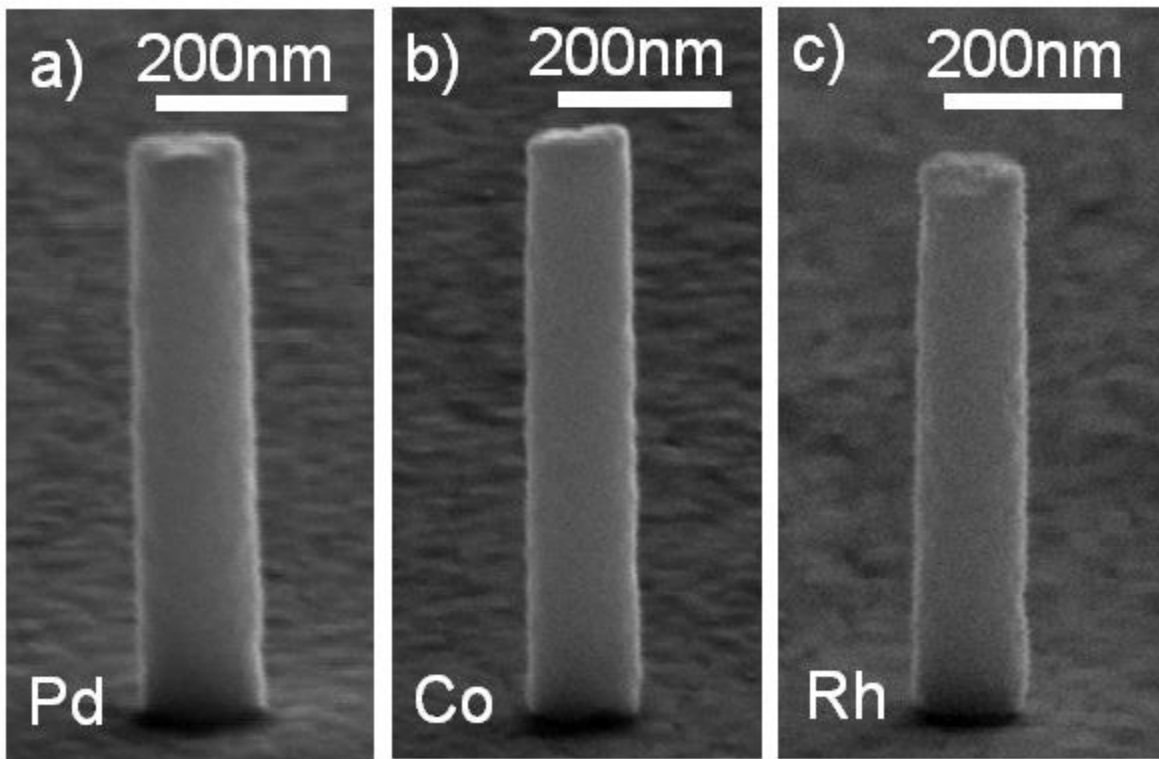
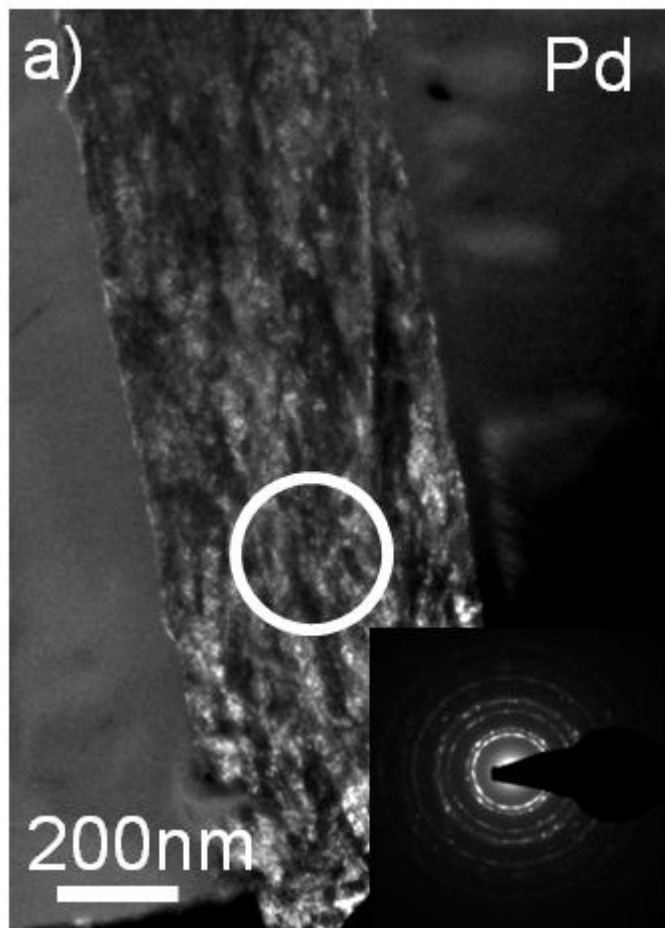


Figure 6.1: SEM micrograph of as-fabricated nanopillars - (a) palladium; (b) cobalt; and (c) Rhodium. All structures have diameters of ~130nm and aspect ratio ( $L/r$ ) near 10. All SEM images taken at a  $70^\circ$  stage tilt.



**Figure 6.2:** (a) TEM dark field image of the full length of a 520 nm palladium nano-pillar along with diffraction pattern. (b) TEM dark field image of the full length of a ~520 nm Cobalt nano-pillar along with diffraction pattern. (c) High magnification SEM image of 1050nm Rhodium nanopillar

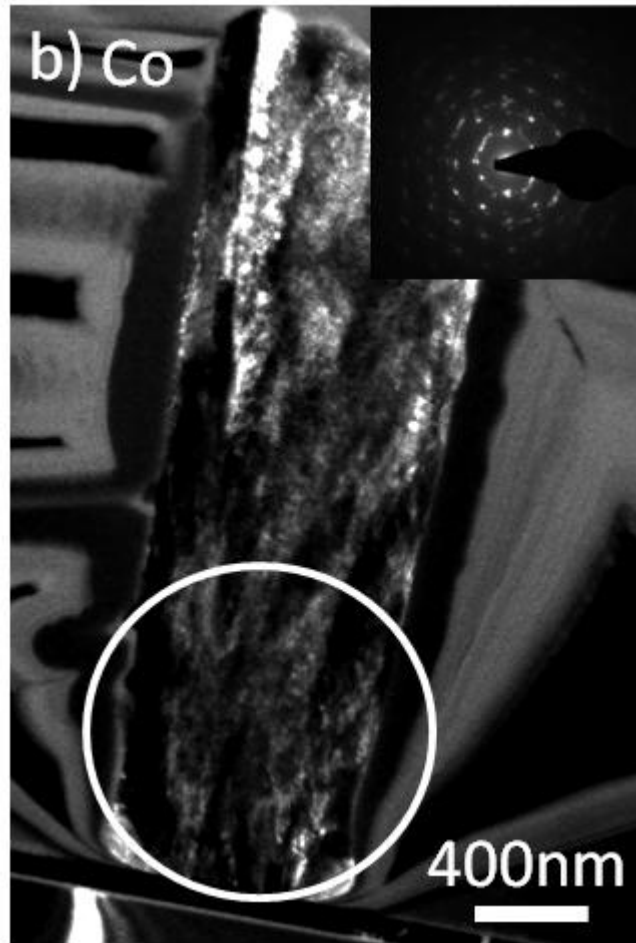


Figure 6.3: (a) TEM dark field image of the full length of a 520 nm palladium nano-pillar along with diffraction pattern. (b) TEM dark field image of the full length of a ~520 nm Cobalt nano-pillar along with diffraction pattern. (c) High magnification SEM image of 1050nm Rhodium nanopillar

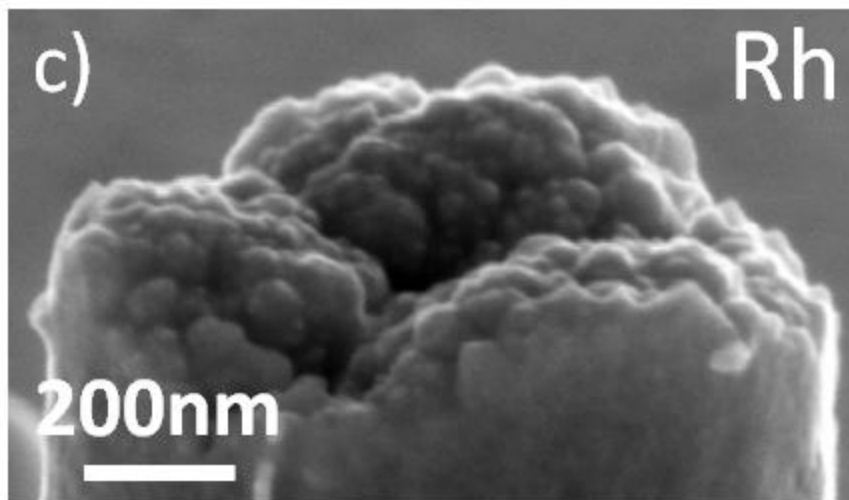


Figure 6.4: (a) TEM dark field image of the full length of a 520 nm palladium nano-pillar along with diffraction pattern. (b) TEM dark field image of the full length of a ~520 nm Cobalt nano-pillar along with diffraction pattern. (c) High magnification SEM image of 1050nm Rhodium nanopillar

### 6.3.2 Post Compression SEM Analysis

To gain understanding of the deformation mechanisms operating in the electroplated nanopillars, all specimens were compressed at  $\sim 1$  nm/s and inspected with high resolution SEM. Figure 6.3 (a) to (c) displays the post compression SEM images of typical deformed palladium nanopillars with length-to-radius ratios near 3.4, 8, and 18 respectively. It is evident that the compressed palladium specimens do not buckle when their initial height is less than 3.4 times their radius. Figure 4 (a) shows that low aspect ratio palladium nanopillars deform uniformly with isotropic increase in cross-sectional area. The compressed nanopillar also has a barrel like shape, with a greater increase in diameter near the mid-point of the column. For taller palladium nanostructures, Figure 6.3 (b) shows the structure begins to exhibit failure by bending under the compressive stress. However, there is no crack formation or significant change in nanopillar diameter near the bending midpoint. Finally, Figure 6.3 (c) shows that palladium nanostructures with large aspect ratios demonstrate significant deformation when compressed uniaxially. Buckling is the clear deformation mechanism, and although this specimen has been bent by nearly  $90^\circ$ , no crack or other fracture event is observed. Further inspections of other deformed high aspect ratio palladium nanopillars revealed that specimens with length-to-radius ratios near 20 may bend plastically up to  $119^\circ$  without crack formation. This corresponds to a linear engineering strain approximately 24 % on the outside surface of the nanopillar. Thus, high aspect ratio palladium specimens exhibit a very high ductility during deformation at the nanoscale. It is also important to note that the deformed palladium nanostructures are all well adhered to the gold layer underneath, regardless of deformation mechanism. Additionally, strong adhesion at the palladium/gold interface impedes lateral shifts during compression. The same is not true for the palladium/nanoindenter interface at the top of the nanopillar, which may shift laterally as observed in Figure 6.3 (c).

Post compression SEM images of cobalt nanopillars with initial length-to-radius ratios near 5, 7, and 14 are shown in Figures 6.4 (a) to (c) respectively. The post mortem analysis reveal that cobalt specimens behave in a very similar manner to palladium where buckling characteristics are not exhibited until the

height of the structures are at least seven times larger than the radius. Interestingly, Figure 6.4 (c) reveals that the deformed cobalt specimens fracture near the middle of the structure with a bending strain similar to the palladium nanopillar shown in Figure 6.4 (c). This suggests that the cobalt nanostructures are less ductile than palladium. However, it is clear that the nanopillar failure shown Figure 6.4 (c) is not brittle fracture since the top and bottom sections of the cobalt specimen remain attached.

Figures 6.5 (a) to (c) display the deformation character of rhodium nanopillars with length-to-radius ratios of 5, 7, and 17. Again, a similar buckling to palladium and cobalt nanopillars is apparent in rhodium specimens, with higher aspect ratio structures demonstrating failure by buckling. Similar to cobalt, fracture is observed in the deformed high aspect ratio rhodium specimen shown in Figure 6.5 (c). Rhodium, like palladium and cobalt, shows excellent adhesion to the underlying gold substrate, and no lateral shifting at this interface is observed. Contrastingly, the top nanopillar interface for all materials is not mechanically constrained and free lateral shifts occur.

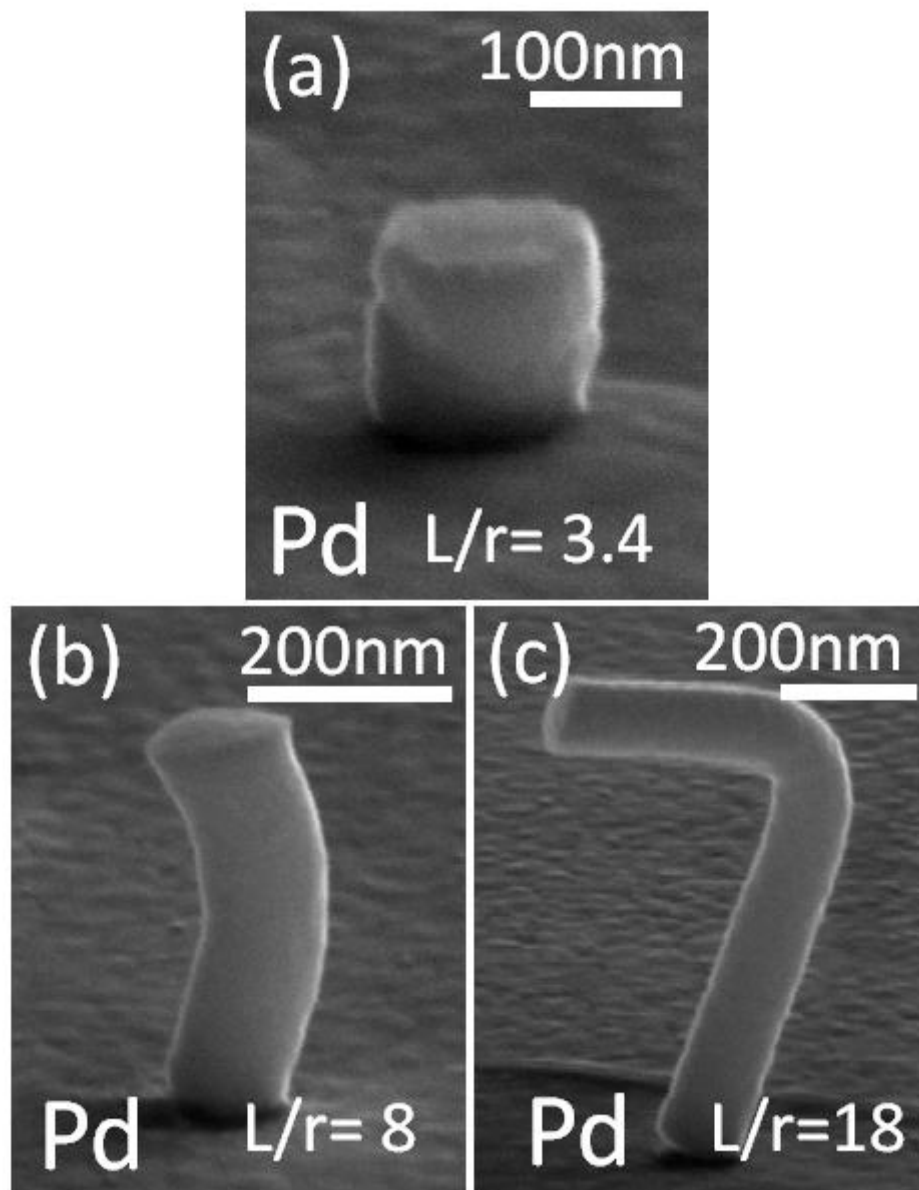


Figure 6.3. Post compression SEM micrographs of Pd pillars with different aspect ratios ( $L/r$ ) of (a)3.4, (b) 8, and (c) 18.

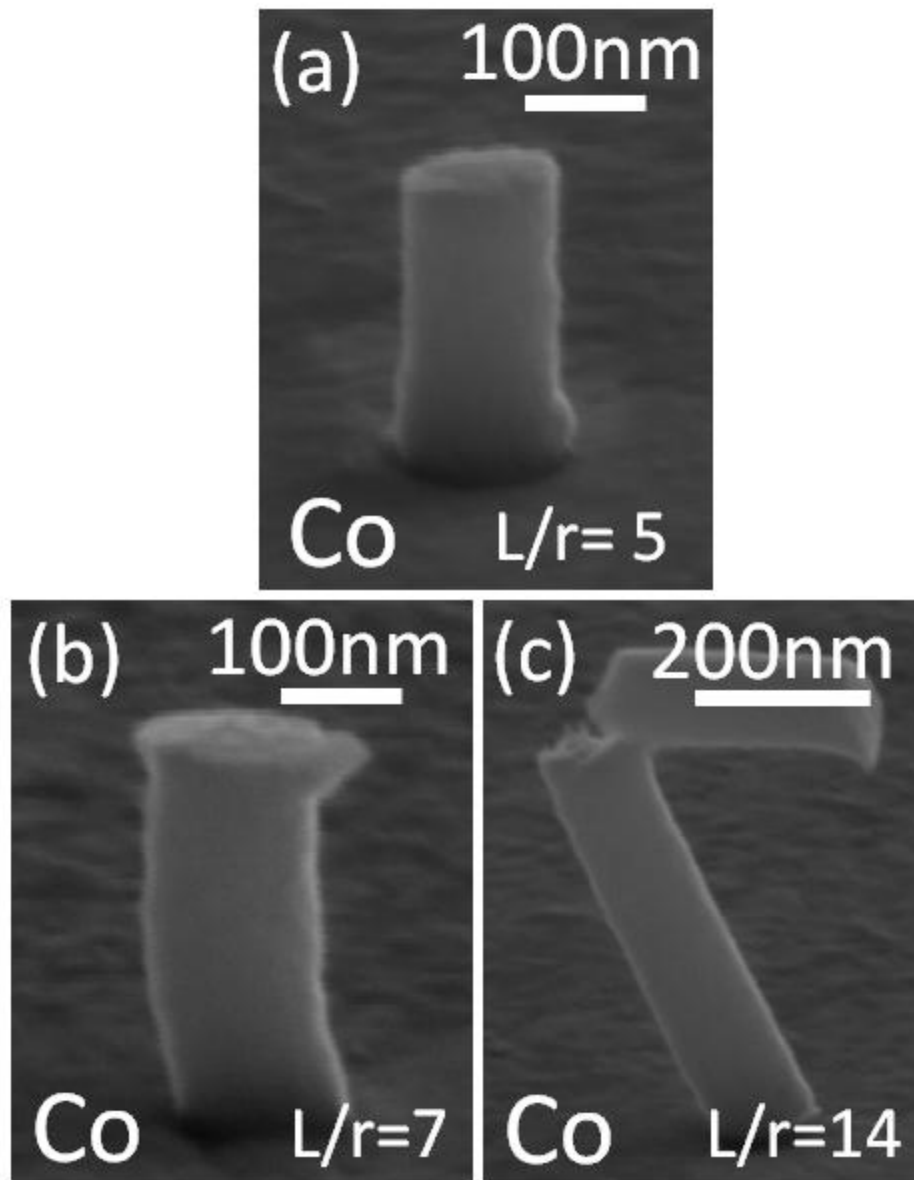


Figure 6.4. Post compression SEM micrographs of Co pillars with different aspect ratios ( $L/r$ ) of (a) 5, (b) 7, and (c) 14.

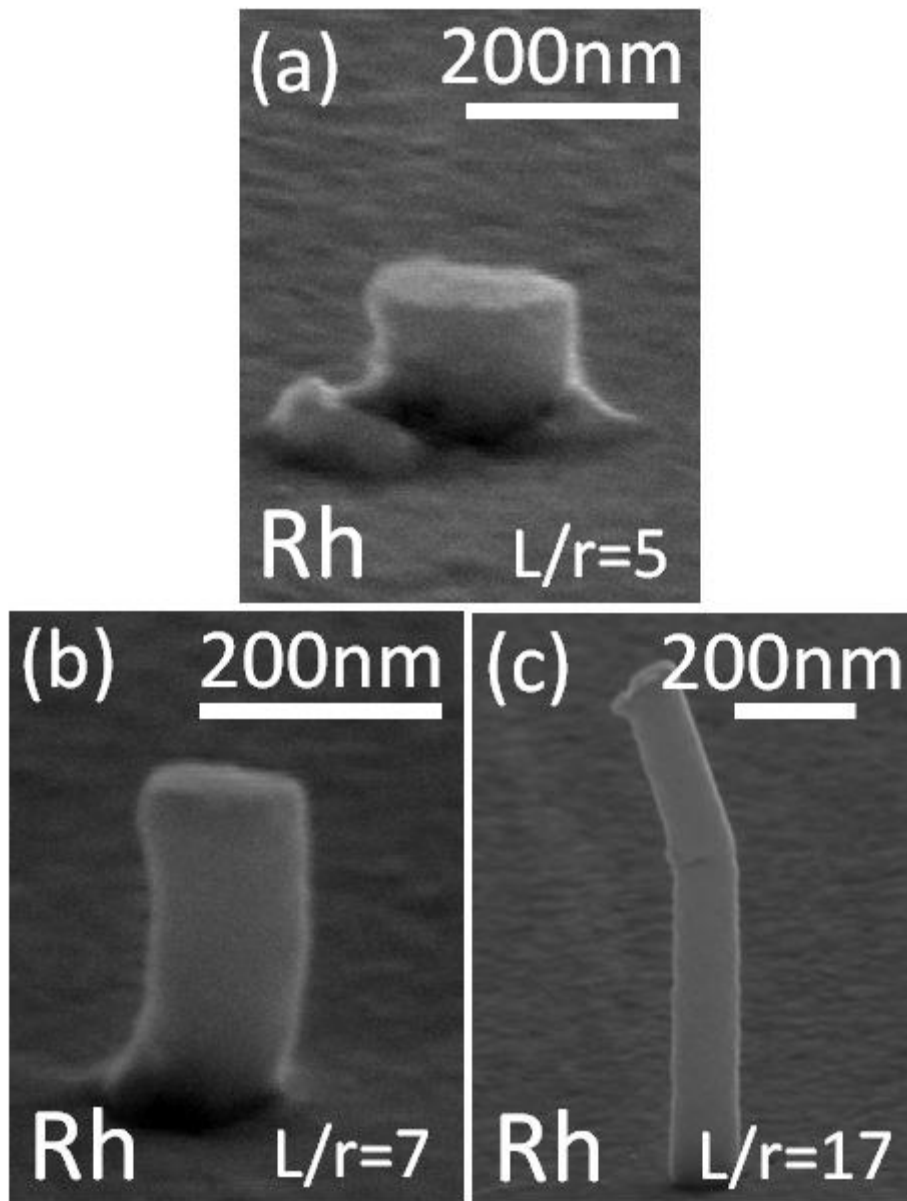


Figure 6.5. Post compression SEM micrographs of Rh pillars with different aspect ratios ( $L/r$ ) of (a) 5, (b) 7, and (c) 17.

### 6.3.3 Load-Displacement Behaviors

The load-displacement responses of palladium, cobalt, and rhodium nanostructures are summarized in Figure 6.6 (a) to (c), respectively. Figure 6.6 (a) shows the influence of length-to-radius ratio on the resistance to applied loads of 130 nm diameter palladium nanostructures. Clearly, increasing nanopillar height results in a weaker structure which sustains far less compressive force. This is expected since the onset of buckling deformation occurs when the length-to-radius ratio reaches a value near 7, as was observed in post-mortem SEM analysis. For buckled nanopillars with length-to-radius ratios of at least 7, the load-displacement curves show a clear instability shortly after reaching the maximum load. The maximum load the nanostructures can support before failure by bulking is characterized as the critical load of buckling ( $P_{cr}$ ). Figure 6.6 (a) shows that the critical load values exhibited by palladium nanopillars reduce as the columnar structures become taller with constant initial cross-sectional area.

The load-displacement curves of cobalt and rhodium nanopillars are plotted in Figure 6.6 (b) and (c), respectively. Like the palladium results, shorter cobalt and rhodium nanopillars sustain the highest critical load values prior to failure. These figures also show that for nanopillars which have the same aspect ratios, the cobalt nanostructures support more mechanical load than palladium before buckling. This is expected since cobalt has a bulk elastic modulus two times that of palladium. According to Eq. (1), the critical load of buckling  $P_{(cr)}$  is directly proportional to the elastic modulus of the material. A similar observation is made when comparing rhodium nanostructures to cobalt and palladium.

The critical loads corresponding to catastrophic buckling failure for palladium, cobalt, and rhodium nanopillars are summarized in Figures 6.7 (a) to (c) respectively. The buckling loads are plotted as a function of length-to-radius ratios. The results presented in Figure 8 only include data from nanopillars that exhibit buckling deformation after the compression tests, which generally corresponds to a length-to-radius ratio greater than 7. From Figure 6.7, a significant dependence is observed between the critical applied load prior to deformation by buckling and the nanostructure aspect ratio. For palladium nanopillars (Figure 6.7 (a)), the maximum load supported reduces rapidly for length-to-radius ratios

between 7 and 15. A very similar observation is made in Figures 6.7 (b) and (c) for both cobalt and rhodium nanopillars, respectively. However, also in Figures 6.7 (b) and (c), as the nanopillar length-to-radius ratio is increased beyond 15, the critical load values begin to stabilize and reduce with column height at a much slower rate.

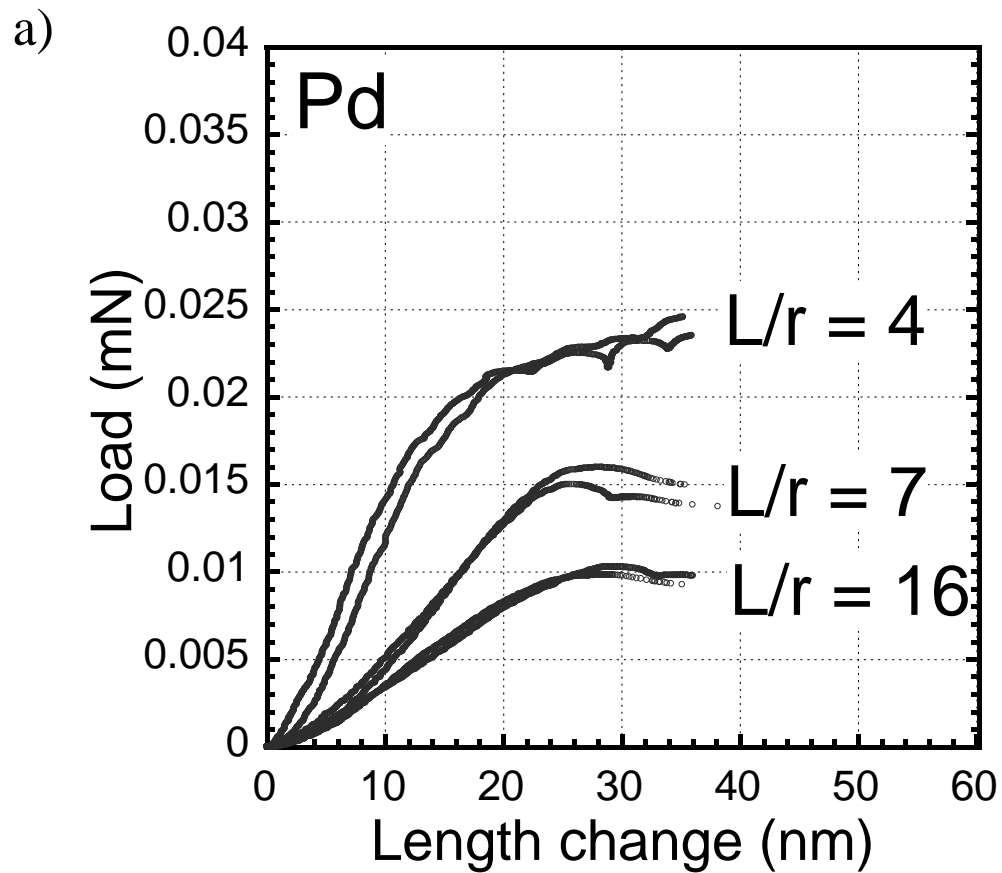


Figure 6.6. Representative engineering stress–strain curves of 130nm diameter pillars (a) Pd, (b) Co, and (c) Rh. All pillars were deformed at a displacement rate of 1nm/s.

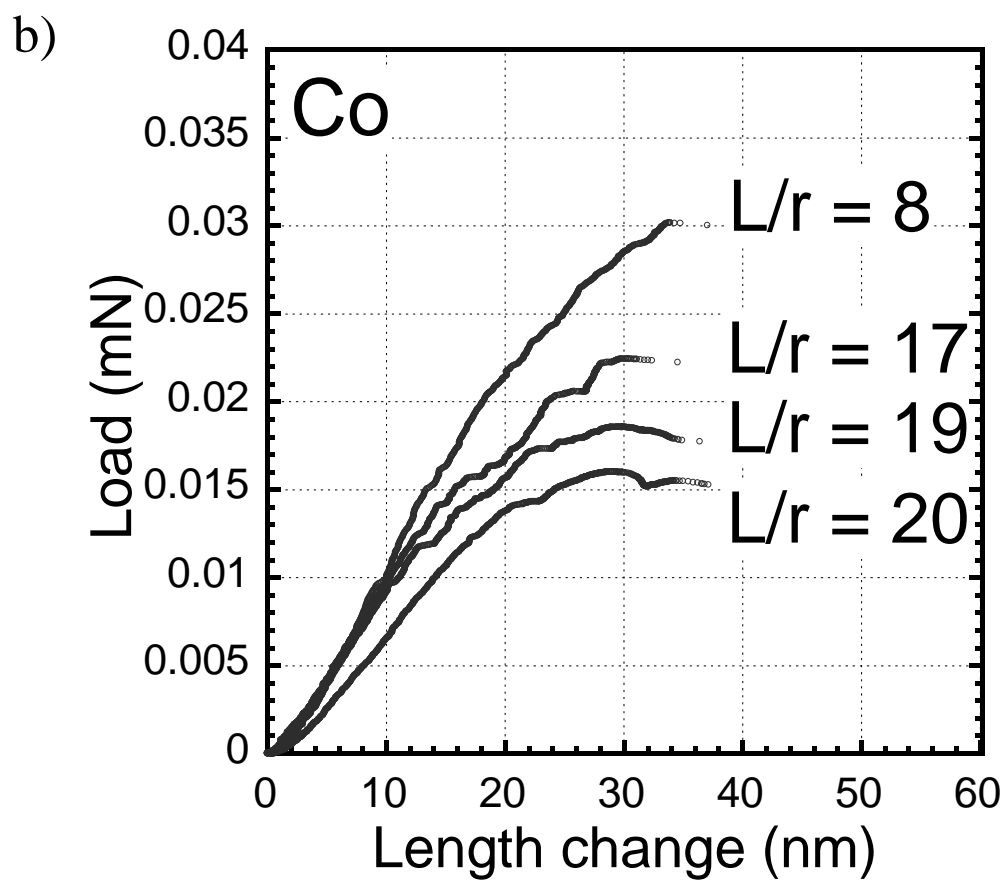


Figure 6.6. Representative engineering stress–strain curves of 130nm diameter pillars (a) Pd, (b) Co, and (c) Rh. All pillars were deformed at a displacement rate of 1nm/s

c)

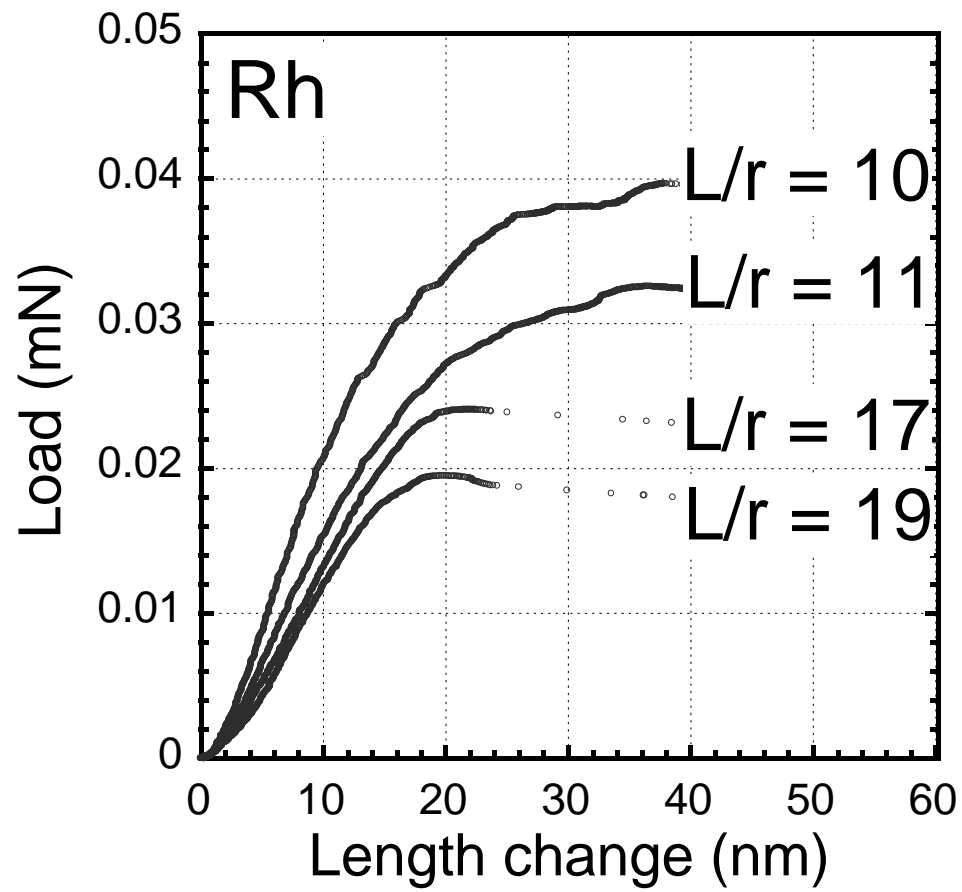


Figure 6.6. Representative engineering stress–strain curves of 130nm diameter pillars (a) Pd, (b) Co, and (c) Rh. All pillars were deformed at a displacement rate of 1nm/s

It is important to note that a constant displacement rate was used for all nanostructures compressed in this work. As a result, the materials are actually deformed by a range of strain rates, defined as the displacement rate divided by the initial nanopillar height, with taller specimens being compressed at slower strain rates. It has been recently shown in the compression of molybdenum, indium, tin, bismuth, and copper nanopillars that strength of these materials are strain rate sensitive at the nanoscale. In order to demonstrate that the strain rate does not affect the critical load results presented in this work, a series of compression experiments were performed at different displacement rates on palladium, cobalt, and rhodium nanopillars with the aspect ratios of 16, 14, and 11 respectively. These specimens were uniaxially compressed with displacement rates in the range of ~0.2 nm/s and 20 nm/s. The critical buckling load results are plotted as a function of the deformation rate in Figure 6.8. The measured critical loads plotted in Figure 6.8 show virtually no change in all three materials with two orders of magnitude change in displacement rate. Therefore, variance in the actual strain rate used to compress the nanopillar specimens in this work are not expected to influence the final critical load results.

The critical loads,  $P_{(cr)}$ , of palladium, cobalt, and rhodium nanopillars were plotted in Figures 6.9 (a) to

(c) as a function of the effective cross-sectional area,  $\frac{\pi^2 I}{(KL)^2}$ . In this analysis, the interface between the nanopillar and substrate is assumed to be perfectly bonded, while the nanopillar/nanoindenter interface is assumed to free to move. These assumptions were based on the actual observations of the deformed structures, such as those micrographs revealed in figure 6.3-6.5, where the base of the pillars were restrained from lateral motion and the top interfaces allow to slide freely. The corresponding constraint factor ( $K$ ) for these boundary conditions has a value of 2.0 [105]. According to the Euler and the tangent modulus buckling models, the elastic modulus of very long slender structures or tangent modulus of intermediate length pillars can be extracted from the linear slope of these plots. The data in Figure 6.9 was fitted with the linear relationship and revealed that the slope for palladium, cobalt, and rhodium nanostructures are 90 +/- 6 GPa, 175 +/- 9 GPa, and 375 +/- 23 GPa, respectively. The quoted error spread corresponds to one standard deviation. These values are slightly smaller than the bulk elastic

modulus of the corresponding materials. A summary of these values is presented in table 6.1. Sanders *et al.* [84] characterized the elastic modulus for bulk scale samples of nanocrystalline palladium samples with an average grain size of 16 nm by uniaxial tensile test. Their results showed that the material has an elastic modulus value near 117 GPa, which is slightly greater than the upper limit of the results measured in this work. The elastic properties of bulk nanocrystalline cobalt specimens were measured by Karimpoor *et al.* [108], also by uniaxial tensile tests. They show the elastic modulus value of  $208 \pm 23$  GPa, which also greater than the current results. Bulk coarse grained rhodium specimens have moduli of 379 GPa [111] is again slightly greater than the averaged modulus results presented here. These comparisons indicate that the slopes extracted from Figure 6.9 are not identical to elastic modulus of the corresponding materials. Instead, it is the tangent moduli as described by the Engesser model. This is often observed during the compression buckling for intermediate length structures such as those studied in this work.

a)

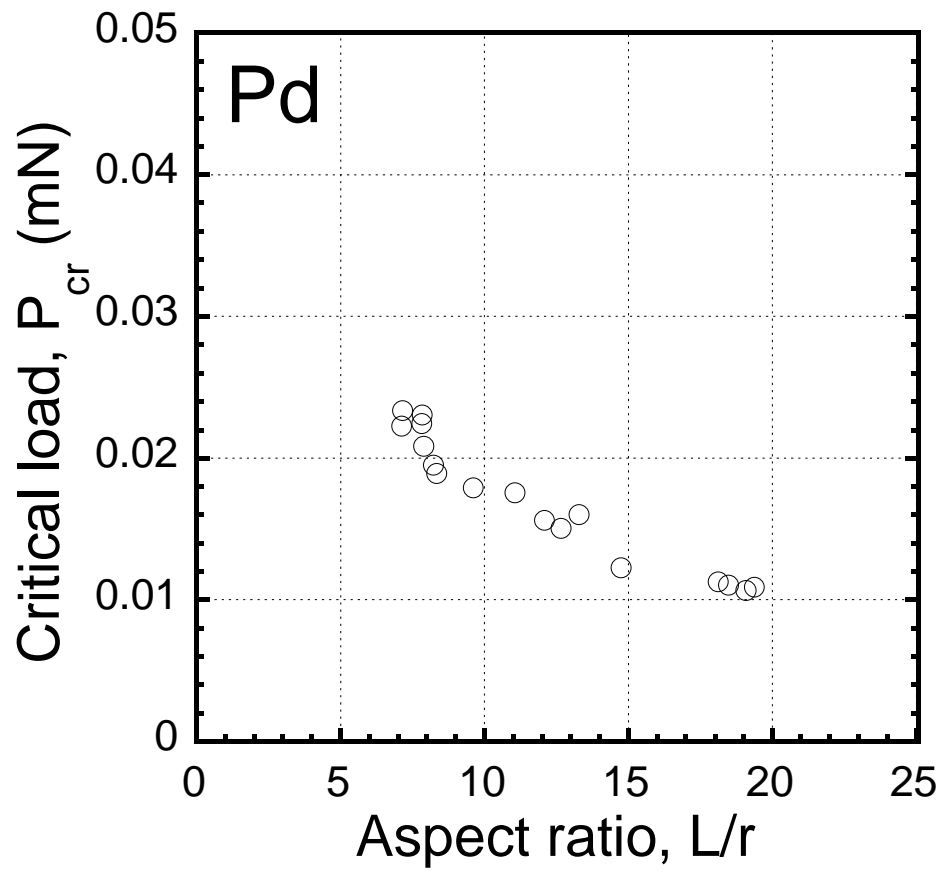


Figure 6.7. Plot of critical buckling load as a function of aspect ratios ( $L/r$ ) (a) Pd; (b) Co; and (c) Rh nanostructures.

b)

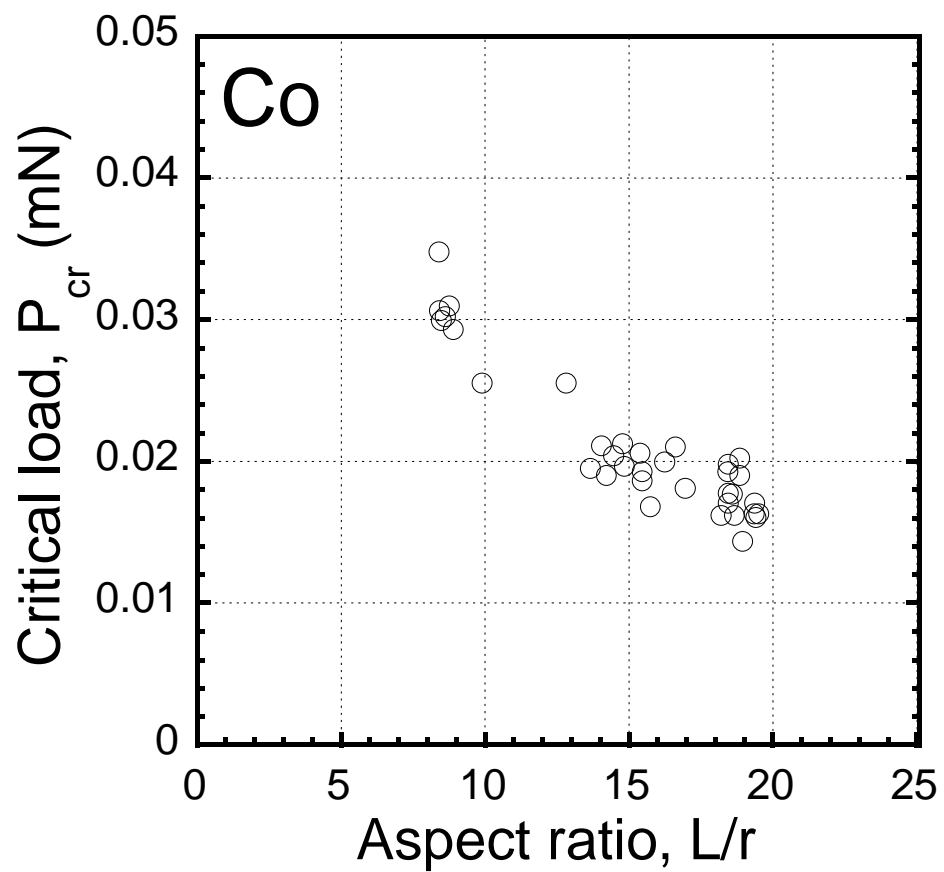


Figure 6.7. Plot of critical buckling load as a function of aspect ratios ( $L/r$ ) (a) Pd; (b) Co; and (c) Rh nanostructures.

c)

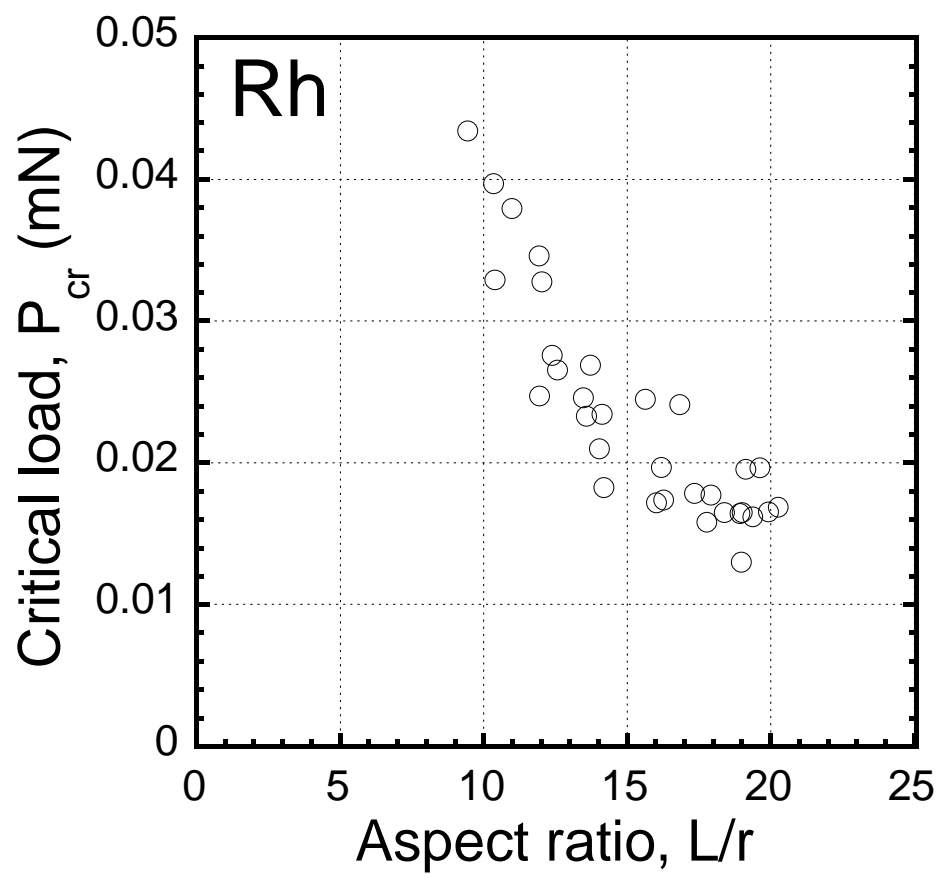


Figure 6.7. Plot of critical buckling load as a function of aspect ratios ( $L/r$ ) (a) Pd; (b) Co; and (c) Rh nanostructures.

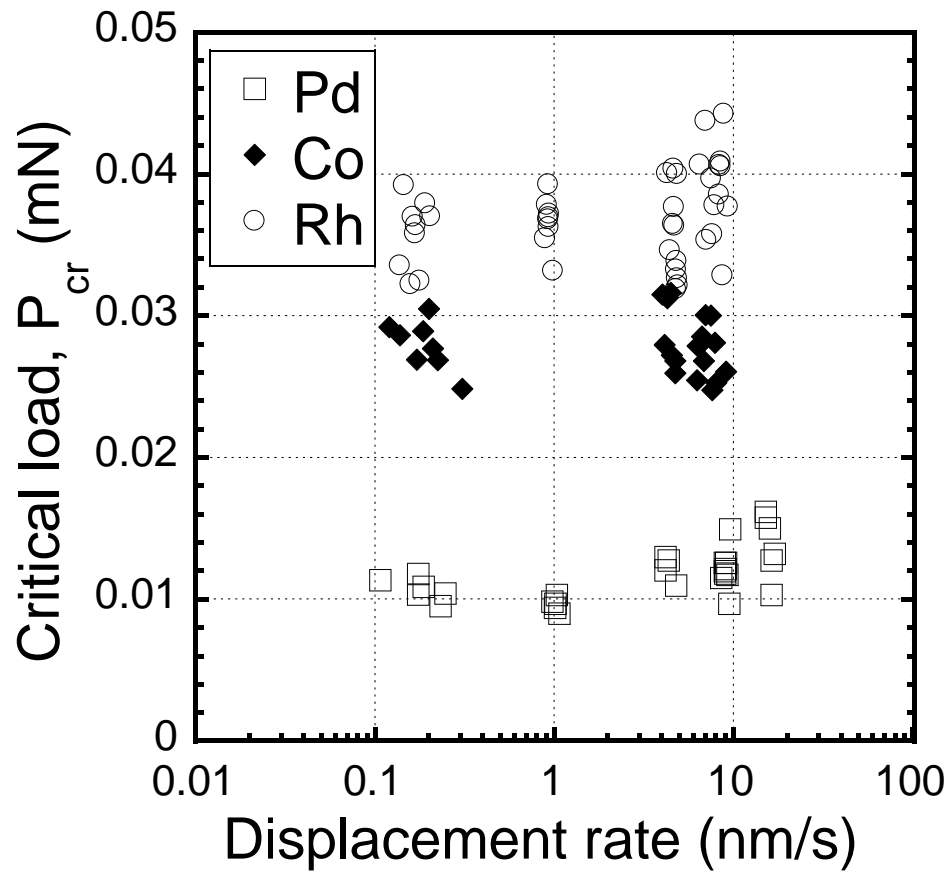


Figure 6.8. Critical buckling load of Pd ( $L/r=16$ ), Co ( $L/r=14$ ), and Rh ( $L/r=11$ ) pillars at different displacement rates.

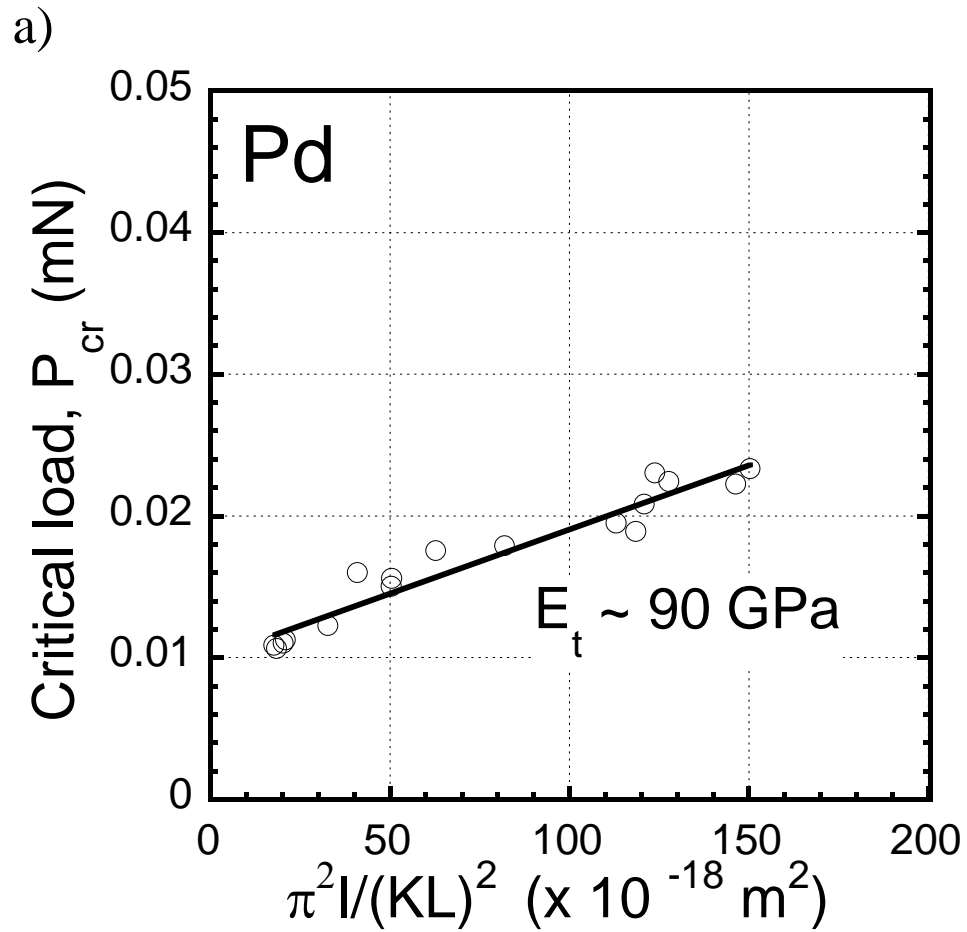


Figure 6.9. Plot of critical buckling load as a function of effective area  $\pi^2 I / (KL)^2$  for (a) Palladium (b) Cobalt and (c) Rhodium nanopillars.

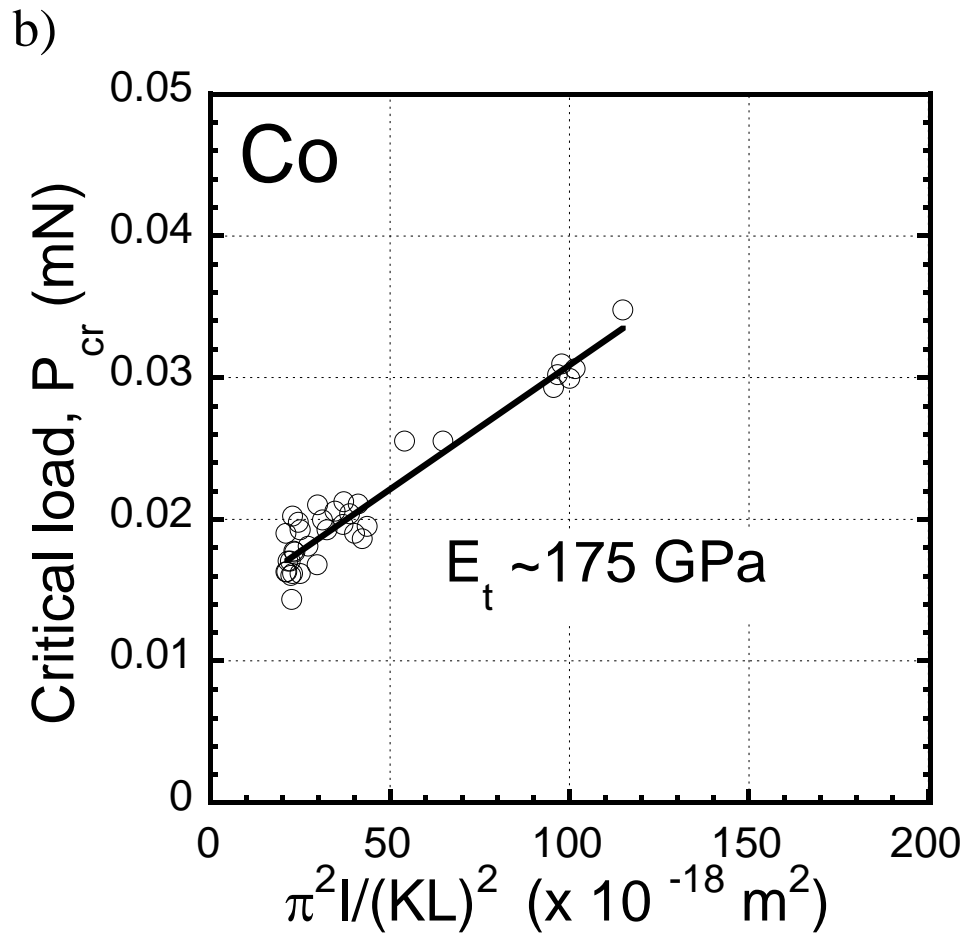


Figure 6.9. Plot of critical buckling load as a function of effective area  $\pi^2 I / (KL)^2$  for (a) Palladium (b) Cobalt and (c) Rhodium nanopillars.

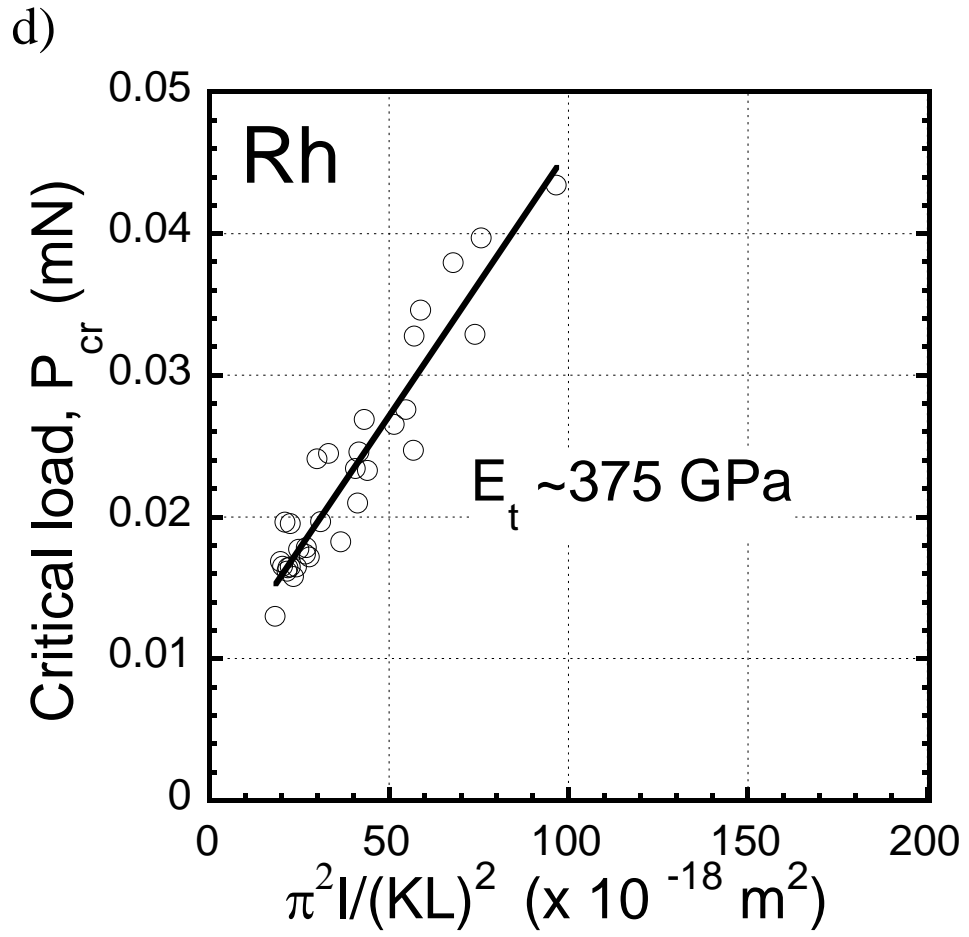


Figure 6.9. Plot of critical buckling load as a function of effective area  $\pi^2 I / (KL)^2$  for (a) Palladium (b) Cobalt and (c) Rhodium nanopillars.

<b>Specimens</b>	<b>Bulk modulus (GPa)</b>	<b>Nanopillar tangent modulus (GPa)</b>	<b>R<sup>2</sup></b>
Pd	117 [13]	90 +/- 6	0.94
Co	208 [14]	175 +/- 9	0.96
Rh	379 [15]	375 +/- 23	0.95

**Table 6.1. Summary of measured elastic modulus values for palladium, cobalt, and rhodium nanopillars and their bulk counterparts.**

## 6.4 Conclusions

Polycrystalline palladium, cobalt, and rhodium nanopillars with diameters of 130 nm and length-to-radius ratios in the range of 4 to 20 were successfully fabricated. Through uniaxial compression tests, the buckling behavior and critical buckling loads of these nanostructures were characterized. The critical buckling loads were shown to be insensitive to displacement rate. By extracting the slope from the critical load versus effective area plots, the tangent moduli of the fabricated nanopillars were calculated to be  $90 \pm 6$  GPa,  $175 \pm 9$  GPa, and  $375 \pm 23$  GPa for nanoscale palladium, cobalt, and rhodium respectively. SEM inspection of the buckled nanostructures reveal that palladium nanopillars do not exhibit fracture despite nearly 24 % of engineering strain, and are significantly more ductile than similar cobalt or rhodium nanostructures. In contrast, cobalt and rhodium specimens with length-to-radius ratios near 20 display crack formation after buckling.

## Chapter 7: Conclusions and Future Research Directions

Before small scale mechanical testing methods were implemented, most mechanical properties of materials were known to be independent of their shape and geometry. All materials studied in this work show that when the dimensions of the material structures are reduced to nano scale, they plastically deform at strengths and with mechanisms different from that of their bulk counterparts. This proposes a need for a new study of the behaviours of all materials in this scale.

Our results showed different types of size-dependant deformation for the 4 materials studied.

In single crystal tin and indium, and polycrystalline bismuth nanostructures with 1 grain, the pillars showed a strengthening effect with a decrease in pillar size. This strengthening was attributed to dislocation starvation in nanoscale rather than a multiplication of dislocations in bulk single crystal structures. In simple words, with the existence of free surfaces, the dislocations leave the pillar structures faster than new dislocations are generated. In nanocrystalline palladium however, the existence of free surfaces mediated the deformation process and resulted in an inverse size effect where the pillars became softer at smaller diameters (or smaller surface area to volume ratios).

Another size effect was seen in polycrystalline bismuth nanostructures; if the size of the pillars was near the size of the material grain size, the pillars exhibited higher strengths. This was attributed to the existence of grain boundaries in larger pillars and a transition between grain boundary mediated processes to dislocation processes in small pillar sizes.

Finally, a fourth type of size effect was seen in indium nanostructures; some pillars were able to reach flow stresses near theoretical strength after the application of purely mechanical strain.

### 7.1 Micro-tensile Tests

Although many micro-compression tests have been conducted, the tensile behaviour of most metals at nano scale are yet to be studied. In situ tensile testing equipments have the capability of performing nano scale tensile tests on specially designed specimens [111]. An important part of the tensile test methods is

the fabrication of these specimens. Using the electroplating methods shown in this work, tensile test specimens could also be fabricated.

## **7.2 Variable Temperature Tests**

Temperature effects on the deformation behaviour of all the presented materials would be another interesting research direction. To the best of our knowledge, there is no data presented on the high or low temperature behaviour of material under micro-compression. The nanoindenter is operational at temperatures 20° above and below room temperature allowing a range of temperatures that materials can be studied under micro-compression. However, load holding tests performed on fused silica showed great thermal drift for very small changes in temperature. This drift will highly affect the compression results at high temperatures, especially for the smaller pillar diameters, resulting in an over or under estimation of the flow stress. Tests on a group of 1000 nm and 200nm indium nanopillars shown in figure 7.2 and 7.3 respectively, present a comparison between the room temperature data and tests run at 32°C with 2-3°C variations in temperature. For these tests, the heating process was done via an incandescent light bulb which was shut off at the beginning of each test. This method resulted in a rather stable temperature for the period of pillar compression. The variation (decrease) in temperature was higher for the lower strain rates due to longer times for these compression tests. This result is reflected in the presented data showing an apparent decrease in the flow stress for a decrease in strain rate in the case of 240 nm pillars. For the 1000nm pillars this effect is less visible.

In conclusion, to study the effects of temperature on the plastic deformation of materials using micro and nano indentation methods, one needs to present accurate drift correction methods. And due to the extreme sensitivity of the indenter to temperature changes, the temperature needs to be held constant during the entire compression test.



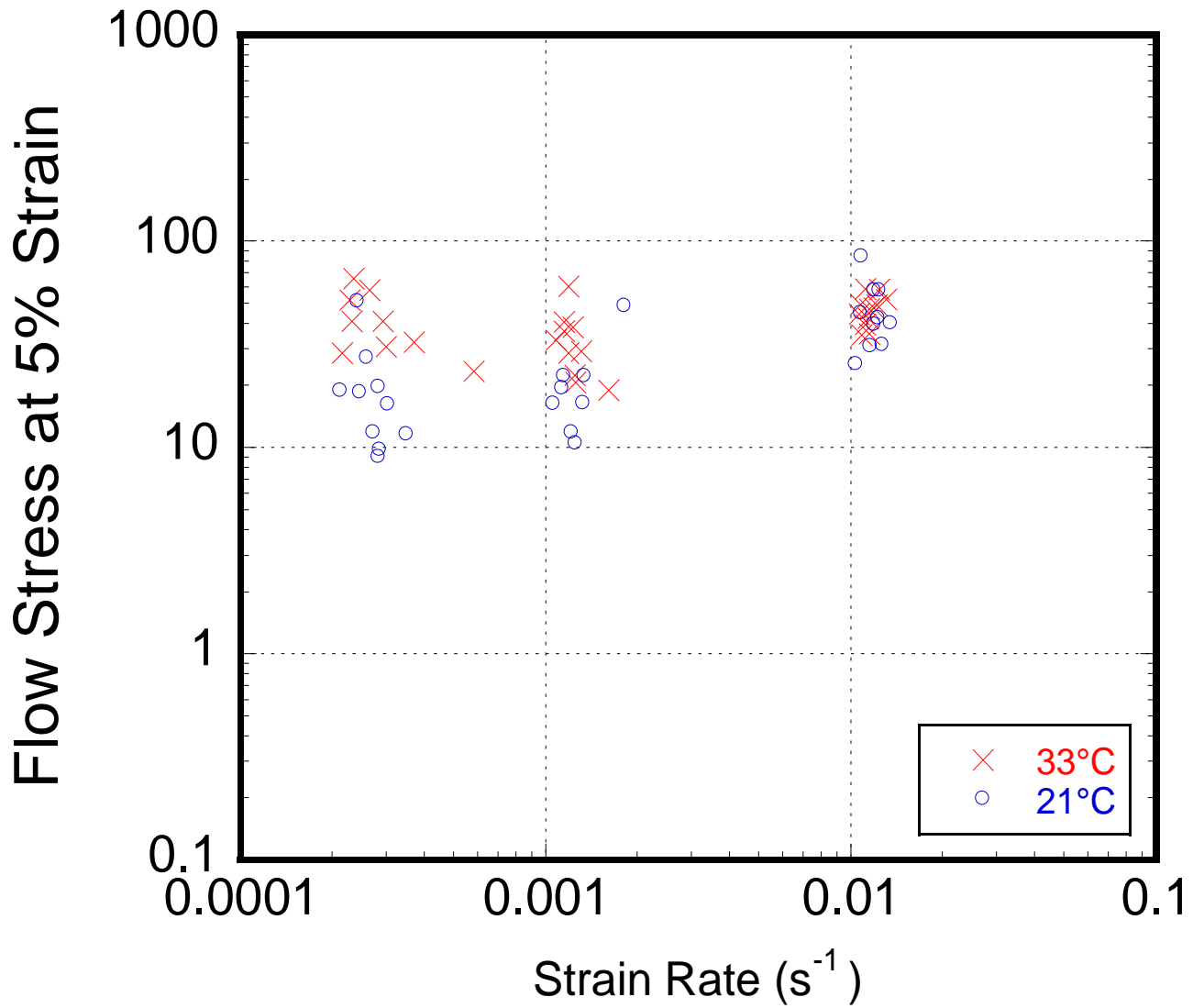


Figure 7.2: High temperature flow stresses at 5% strain for 200nm indium nanopillars at 3 different stain rates compared to room temperature tests

### 7.3 Statistical Analysis

Impact energy of the indenter with the pillars depends on the mass of the indenter and the velocity of its approach to the compression test specimen. Usually, an approach velocity of 10nm/s is used in these tests which corresponds to an impact energy of about 2-5 eV. A. B. Mann saw, that by reducing the approach velocity, less scatter was seen in their data [112]. The argument is that the initial impact of the pillar can be the cause of dislocation initiations. For example, it might well be that the smaller indium nano pillars are all initially pristine and dislocations are only generated by the initial impact of the nanoindenter. All our tests were conducted with an approach velocity of 10nm/s. A statistical analysis on a large group of pillars with different surface approach velocities would show the effects of this parameter in micro-compression tests.

Also, in Sn and In nano pillars, two different deformation behaviour were seen. Figure 7.3 (a) shows a representative indium nanopillar deformed by extrusion and Figure 7.3 (b) shows a 1000nm indium nanopillar deformed by crystallographic shear. Although extensive statistical analysis has not been done, crystallographic shear seems to be a more dominant deformation mechanism in the smaller sized indium nanopillars. A study on the distribution of these deformation types and their effects on pillar flow stresses is another path for future research. Along with extensive  $\mu$ SXRD studies on pillar microstructures prior to and after compression an explanation of this extrusion type deformation can be presented. One proposed explanation is that in a pillar with multiple slip systems, the dislocations stay within the pillars changing directions from one active slip plane to another resulting in lower flow stresses whereas in the case of crystallographic shear, the pillar moves along one slip plane until it reaches a free surface.

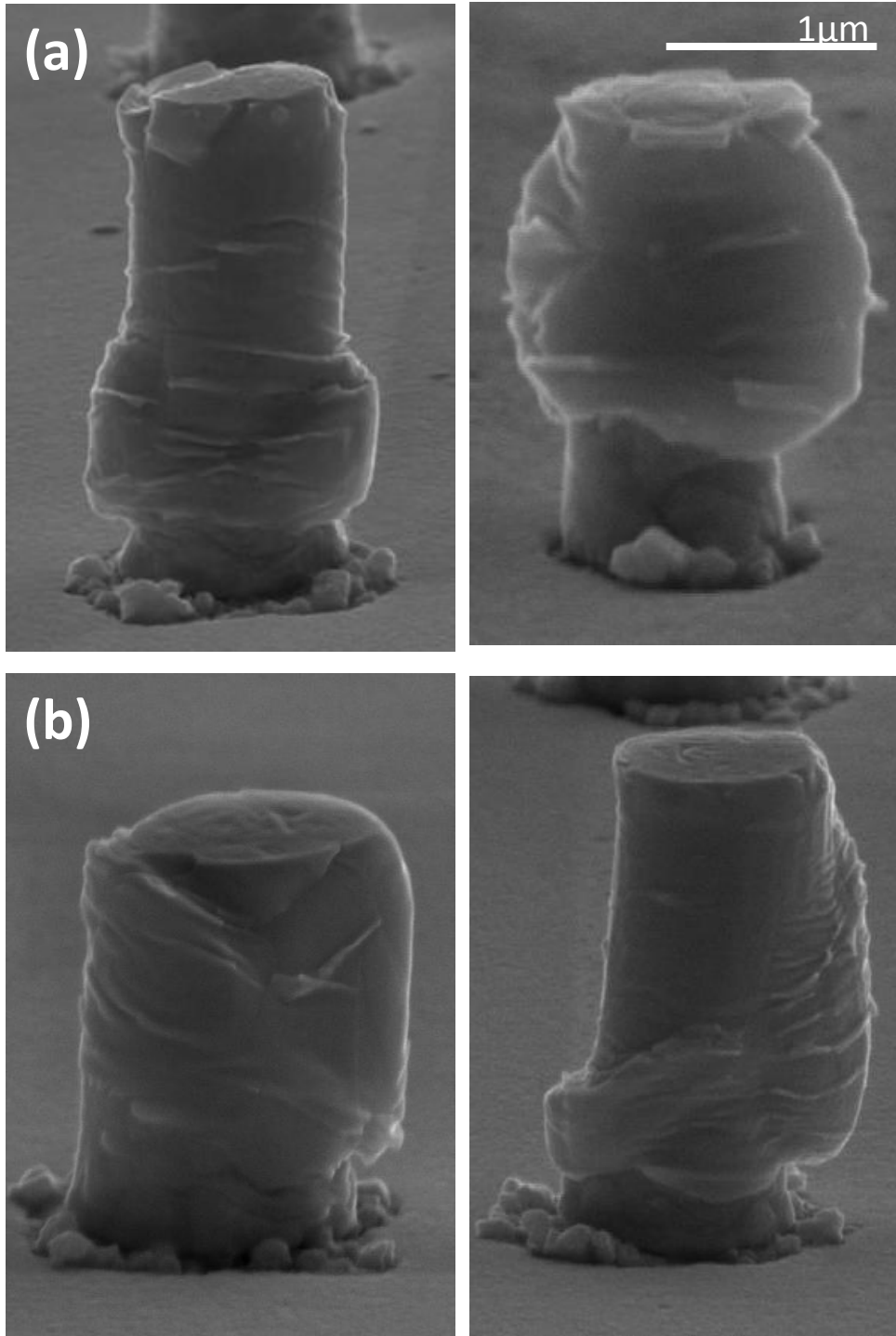


Figure 7.3: Indium ~1070 nm pillars showing two different forms of deformation : (a) barrelling (b) barrelling followed by plastic crystallographic shear

#### **7.4 In-situ Experimentss**

Finally, in order to fully understand the behaviour of these metals at each point of the mechanical micro-compression test, nano scale compression tests inside a Transmission Electron Microscope (TEM) should be conducted for these materials, similar to the experiments run at the National Center for Electron Microscopy at Lawrence Berkely National Laboratory [34]. This will result in a more thorough understanding of the different mechanisms contributing to the plastic deformation.

## Bibliography

- [1] U. Messerschmidt, *Dislocation Dynamics during Plastic Deformation (1<sup>st</sup> edition)*: Springer-Verlag, 2010.
- [2] M.D. Uchic, P.A. Shade, D.M. Dimiduk, “*Plasticity of Micrometer-Scale Single Crystals in Compression*,” *Annual Review of Materials Research*, vol 39, 2009, p. 361.
- [3] W.C. Pharr, G.M. Oliver, “*An improved technique for determining hardness and elastic modulus using load and displacement sensing indentation experiments*,” *Journal of Materials Research*, vol. 7, 1992, p.1564
- [4] H. Bei, S. Shim, E.P. George, M.K. Miller, E.G. Herbert, G.M. Pharr, “*Compressive strengths of molybdenum alloy micro-pillars prepared using a new technique*,” *Scripta Materialia*. Vol. 57, 2007, p. 397
- [5] H. Zhang, B.E. Schuster, Q. Wei, K.T. Ramesh, “*The design of accurate micro-compression experiments*”, *Scripta Materialia*. Vol. 54, 2005, p. 181.
- [6] G.M. Pharr, T.Y. Tsui, A. Bolshakov, J.C. Hay, “*Nanoindentation of soft films on hard substrates: Experiments and finite element simulations*,” *Composites Science and Technology*. Vol. 68, 2008, p. 147.
- [7] T.Y. Tsui, G.M. Pharr, “*Substrate effects on nanoindentation mechanical property measurement of soft films on hard substrates*” *Journal of Materials Research*, vol. 14, 1999, p. 292.
- [8] N.A. Sakharova, J.V. Fernandes, J.M. Antunes, Oliviera MC, “*Comparison between Berkovich, Vickers and conical indentation tests: A three-dimensional numerical simulation study*,” *International Journal of Solids and Structures*, vol. 46, 2009, p. 1095.
- [9] R.A. Mirshams, P. Parakala, “*Nanoindentation of nanocrystalline Ni with geometrically different indenters*,” *Materials Science and Engineering A.*, vol. 372, 2004, p. 252.
- [10] M.D. Uchic, D.M. Dimiduk, “*A methodology to investigate size scale effects in crystalline plasticity using uniaxial compression testing*,” *Materials Science and Engineering A*. Vol. 400, 2005, p. 268.
- [11] M.D. Uchic, D.M. Dimiduk, J.N. Florando, W.D. Nix, “*Sample Dimensions Influence Strength and crystal plasticity*” *Science*, 2004, vol. 305, p. 986.
- [12] D.M. Dimiduk, M.D. Uchic, T.A. Parthasarathy, “*Size-affected single-slip behavior of pure nickel microcrystals*,” *Acta Materialia*. Vol. 53, 2005, p. 4065.
- [13] C.P. Frick, B.G. Clark BG, S. Orso, A.S. Schneider, E. Arzt, “*Size effect on strength and strain hardening of small-scale [1 1 1] nickel compression pillars*,” *Materials Science and Engineering: A*, vol. 489, 2008, p. 319.
- [14] M.D. Uchic, D.M. Dimiduk, “*A methodology to investigate size scale effects in crystalline plasticity using uniaxial compression testing*,” *Materials Science and Engineering A*, vol. 400-401, 2005,

p.268.

- [15] J. R. Greer, W. C. Oliver, W.D. Nix, “*Size dependence of mechanical properties of gold at the micron scale in the absence of strain gradient*,” *Acta Materialia*, vol. 53, 2005, p. 1821.
- [16] J.R. Greer, W.D. Nix, “*Size dependence of mechanical properties of gold at the sub-micron scale*,” *Applied Physics A*, vol. 80, 2005, p. 1625.
- [17] C.A.Volkert, E.T. Lillerodden, “*Size effects in the deformation of sub-micron Au columns*,” *Philosophical Magazine*, vol. 86, 2006, p. 5567.
- [18] S. Brinckmann, J-Y Kim, J.R. Greer, “*Fundamental Differences in Mechanical Behavior between Two Types of Crystals at the Nanoscale*,” *Physical Review Letters*. Vol. 100, 2008, p. 155502.
- [19] J.R. Greer, J-Y Kim, “*Tensile and compressive behavior of gold and molybdenum single crystals at the nano-scale*. *Acta Materialia*. Vol. 57, 2009, p. 5245.
- [20] S-W Lee , S.M. Han, W.D. Nix, “*Uniaxial compression of fcc Au nanopillars on an MgO substrate: The effects of prestraining and annealing*,” *Acta Materialia*. Vol. 57, 2009, p. 4404.
- [21] D. Kiener, W. Grosinger, G Dehm, R. Pippan, “*A further step towards an understanding of size-dependent crystal plasticity: In situ tension experiments of miniaturized single-crystal copper samples*” *Acta Materialia*. Vol. 56, 2008, p.580.
- [22] D. Kiener, C. Motz, T. Schöberl, M. Jenko, G. Dehm, “*Determination of Mechanical Properties of Copper at the Micron Scale*,” *Advanced Engineering Materials*. Vol. 8, 2006, p. 1119.
- [23] T. Andrew, M.J. Burek, J.R. Greer, “*Microstructure versus size: mechanical properties of electroplated single crystalline Cu nanopillars*,” *Physical Review Letters*, vol. 104, 2010, p. 135503.
- [24] G. Richter , K. Hillerich, D.S. Gianola, R. Monig, O. Kraft, C.A Volkert, “*Ultrahigh Strength Single Crystalline Nanowhiskers Grown by Physical Vapor Deposition*,” *nano letters*, vol 9, 2009, p. 3048.
- [25] H. Bei, S. Shima ,G.M. Pharr, E.P. George, “*Effects of pre-strain on the compressive stress–strain response of Mo-alloy single-crystal micropillars*,” *Acta Materialia*. Vol. 56, 2008, p. 4762.
- [26] J-Y Kim, J.R. Greer, “*Size-dependent mechanical properties of molybdenum nanopillars*,” *Applied Physics Letters*. Vol. 93, 2008, p. 101916 .
- [27] J-Y Kim, D. Jang D, J.R. Greer. “*Tensile and compressive behavior of tungsten, molybdenum, tantalum and niobium at the nanoscale*” *Acta Materialia*. Vol. 58, 2010, p. 2355.
- [28] A.S. Schneider, B.G. Clark, C.P. Frick, P.A. Gruber, E. Arzt, “*Effect of orientation and loading rate on compression behavior of small-scale Mo pillars*,” *Materials Science and Engineering A*, vol. 508, 2009, p.241.
- [29] A.S. Schneider, D. Kaufmann, B.G. Clark, C.P. Frick, P.A. Gruber, “*Correlation between Critical Temperature and Strength of Small-Scale bcc Pillars*”, *Physical Review Letters*. Vol. 103, 2009, p. 105501.
- [30] K.S. Ng and A.H.W. Ngan, “*Stochastic nature of plasticity of aluminum micro-pillars*,” *Acta*

Materialia, Vol. 56, 2008, pp. 1712-1720 .

[31] JY Kim, D. Jang and J.R. Greer, “*Insight into the deformation behavior of niobium single crystals under uniaxial compression and tension at the nanoscale,*” Scripta Materialia, Vol. 61, 2009, pp. 300-303

[32] S. M. Han, T. Bozorg-Grayeli, J. R. Groves and W. D. Nix, “*Size effects on strength and plasticity of vanadium nanopillars,*” Scripta Materialia, Vol. 63, 2010, pp. 1153-1156 .

[33] G. Lee G, J.Y. Kim, A.S. Budiman, N. Tamura, M. Kunz, K. Chen K, M.J. Burek, J.R. Greer, TY Tsui, “*Fabrication, structure and mechanical properties of indium nanopillars*” Acta Materialia , Vol. 58, 2010, pp. 1361-1368.

[34] Z. W. Shan, Raja K. Mishra, S. A. Syed Asif, Oden L. Warren & Andrew M. Minor, “*Mechanical annealing and source-limited deformation in submicrometre-diameter Ni crystals*” Nature Materials , Vol. 7, 2007, pp. 115 - 119.

[35] Michael D. Uchic, Paul A. Shade, Dennis M. Dimiduk, “*Plasticity of Micrometer-Scale Single Crystals in Compression*” Annu. Rev. Mater. Res. , Vol. 39, 2009, p. 361.

[36] M.J. Burek and Julia R Greer, “*Fabrication and Microstructure Control of Nanoscale Mechanical Testing Specimens via Electron Beam Lithography and Electroplating*” Nano letters, Vol. 10, 2010, pp. 69–76.

[37] M. Abtew, G. Selvaduray, “*Lead-free Solders in Microelectronics,*” Materials Science and Engineering, 2000, Vol. 27, pp. 95-141.

[38] J. Glazer, “*Metallurgy of low temperature Pb-free solders for electronic assembly,*” International Materials Reviews, Vol. 40, 1995, pp. 65-93.

[39] W.J. Plumbridge, “*Solders as high temperature engineering materials*”, Materials at High Temperatures, Vol. 17, 2000, pp. 381-387.

[40] H. Mukaibo, T. Momma, M. Mohamedi, T. Osaka, “*Structural and Morphological Modifications of a Nanosized 62 Atom Percent Sn-Ni Thin Film Anode during Reaction with Lithium*” Journal of The Electrochemical Society, 2005, Vol. 152, pp. A560-A565.

[41] F. Yang F, J.C.M. Li, “*Deformation behavior of tin and some tin alloys,*” Journal of Materials Science: Materials in Electronics, Vol. 18, 2007, pp. 191-210.

[42] S.N.G. Chu, J.C.M. Li, “*Impression creep of [beta]-tin single crystals*” Materials Science and Engineering, Vol. 39, 1979, pp. 1-10.

[43] Fuqian Yang and J. C. M. Li, “*Deformation behavior of tin and some tin alloys,*” Journal of Materials Science Materials in Electronics, Vol. 18, 2007, pp. 191-210.

[44] O.D. Sherby, “*Factors affecting the high temperature strength of polycrystalline solids*” Acta Metallurgica, Vol. 10, 1962, pp. 135-147 .

[45] R.E. Frenkel, O.D. Sherby and J.E. Dorn, “*Activation energies for creep of cadmium, indium, and tin,*” Acta Metallurgica, Vol. 3, 1955, pp. 470-472 .

[46] F.E. Jaumot, A. Sawatzky, “*Diffusion of Gold in Single Crystals of Silver,*” Journal of Applied

Physics, Vol. 27, 1956, pp. 1186-1188.

[47] Weertman, J.E. Breen and J, “*A Framework for Modeling Creep in Pure Metals,*” Trans. AIME, Vol. 203, 1955, p. 1230.

[48] F. Mohamed, K. Murty, J. Morris, “*Deformation of Zirconium Alloys at the Nanoscale,*” Metallurgical and Materials Transactions B, Vol. 4, 1973, pp. 935-940.

[49] V. Raman and R. Berriche, “*An investigation of the creep processes in tin and aluminum using a depth-sensing indentation technique,*” Journal of Materials Research, Vol. 7, 1992, pp. 627-638.

[50] D. Josell, “*Exact solution for the zero creep load of a wire,*” Acta Metallurgica et Materialia, Vol. 41, 1993, pp. 2179-2183 .

[51] M. Tian, J. Wang, J. Snyder, J. Kurtz, Y. Liu, P. Schiffer, T.E. Mallouk, M.H.W. Chan, “*Synthesis and characterization of superconducting single-crystal Sn nanowires*” Applied Physics Letters, Vol. 83, 2003, pp. 1620-1622.

[52] N. Tamura, A.A. MacDowell, R. Spolenak, B.C. Valek, J.C. Bravman, W.L. Brown, R.S. Celestre, H.A. Padmore, B.W. Batterman, J.R. Patel, “*Scanning X-ray microdiffraction with submicrometer white beam for strain/stress and orientation mapping in thin films*” Journal of Synchrotron Radiation, Vol. 10, 2003, pp. 137-143.

[53] A.S. Budiman, S.M. Han, J.R. Greer, N. Tamura, J.R. Patel, W.D. Nix, “*A search for evidence of strain gradient hardening in Au submicron pillars under uniaxial compression using synchrotron X-ray microdiffraction*” Acta Materialia, Vol. 56, 2008, pp. 602-608.

[54] G. Feng, A.S. Budiman, W.D. Nix, N. Tamura, J.R. Patel, “*Indentation size effects in single crystal copper as revealed by synchrotron x-ray microdiffraction*” Journal of Applied Physics, Vol. 104, 2008, pp. 043501-043512.

[55] A.S. Budiman, N. Li, J.K. Baldwin, J. Xiong, H. Luo, Q. Wei, N. Tamura, M. Kunz, K. Chen, A. Misra, “*Growth and structural characterization of epitaxial Cu/Nb multilayers,*” Thin Solid Films. Article in Press, 2010, Corrected Proof .

[56] Z. Budrovic, H. Van Swygenhoven, P.M. Derlet, S. Van Petegem, B. Schmitt, “*Plastic deformation with reversible peak broadening in nanocrystalline Ni*” Science, Vol. 304 , 2004, pp. 273-276.

[57] J.R. Greer, C.R. Weinberger, W. Cai, “*Comparing the strength of f.c.c. and b.c.c. sub-micrometer pillars: Compression experiments and dislocation dynamics simulations,*” Materials Science and Engineering: A, Vol. 493, 2008, pp. 21-25.

[58] Nagasaka, M. “*Temperature Dependence of Plastic Deformation in White Tin Single Crystals,*” Japanese Journal of Applied Physics, Vol. 28, 1989, pp. 446-452.

[59] F. Yang F, J.C.M. Li, “*Deformation behavior of tin and some tin alloys,*” Journal of Materials Science: Materials in Electronics, Vol. 18, 2007, p. 191.

[60] Abteu M, Selvaduray G, “*Lead-free Solders in Microelectronics*” Materials Science and

Engineering: R: Reports, Vol. 27, 2000, p. 95.

[61] J. Glazer, “*Metallurgy of low temperature Pb-free solders for electronic assembly*,” International Materials Reviews, Vol. 40, 1995, p. 65.

[62] WJ. Plumbridge, “*Solders as high temperature engineering materials*” Materials at High Temperatures, Vol. 17, 2000, p. 381.

[63] M Tian, J Wang, N Kumar, T Han , Y Kobayashi , Y Liu , TE Mallouk, MHW Chan, “*Observation of Superconductivity in Granular Bi Nanowires Fabricated by Electrodeposition.*” 2006, Nano letters, Vol. 6, p. 2773.

[64] Cullity BD, Stock SR. *Elements of X-Ray Diffraction (3rd Edition)*. s.l. : Prentice Hall, 2001.

[65] EA. Brandes. *Smithells metals reference book*. 6. 1983.

[66] Vickers W, Greenough GB. Cleavage, “*Fracture of Bismuth Single Crystals*”, Nature, Vol. 178, 1956, p. 563.

[67] Das G, Bever M, “*Deformation and stored energy of polycrystalline bismuth*” Metallurgical and Materials Transactions A, Vol. 9, 1978, p. 1875.

[68] Otake S, Namazue H, Matsuno N., “*Critical Resolved Shear Stresses of Two Slip Systems in Bismuth Single Crystals*,” Japanese Journal of Applied Physics, Vol. 19, 1979, p. 433.

[69] RE Frenkel, OD Sherby, JE Dorn, “*Activation energies for creep of cadmium, indium, and tin*,” Acta Metallurgica, Vol. 3, 1995, p. 470.

[70] A. Seeger. *Modeme Probleme der Metallphysik*. Berlin, Heidelberg : Springer-Verlag, 1965.

[71] Burek MJ, Greer JR, “*Fabrication and Microstructure Control of Nanoscale Mechanical Testing Specimens via Electron Beam Lithography and Electroplating*,” Nano Letters, Vol. 10, 2010, p. 69.

[72] Mayo MJ, Nix WD, “*A micro-indentation study of superplasticity in Pb*,” Acta Metallurgica, Vol. 36, 1988, p. 2183.

[73] E. Czerwosz, P. Dluzewski, J. Keczkowska, M. Kolzowski, M. Suchanska, H. Wronka, “*Palladium nanocrystals and their properties*,” Material Science , Vol. 26, 2008,.

[74] Palladium, Stillwater. Palladium Metal of the 21st century. [Online] Stillwater Palladium, 2008. [Cited: 2 15, 2011.] <http://www.stillwaterpalladium.com/>.

[75] Q. Chen, Z. Huang, D. Luck, J. Beckers, PH Brun, B. C. Wilson, A. Scherz, Y. Salomon, F. W. Hetzel, “*Preclinical Studies in Normal Canine Prostate of a Novel Palladium-Bacteriopheophorbide (WST09) Photosensitizer for Photodynamic Therapy of Prostate Cancer*,” Photochemistry and Photobiology, Vol. 76, 2002, pp. 438-445.

[76] R. Birringer, H. Gleiter, H. -P. Klein and P. Marquardt, “*Nanocrystalline materials: an approach to a novel solid structure with gas-like disorder*” Physics Letters A, Vol. 102, 1984, p. 365.

[77] B.E. Schuster, Q. Wei, H. Zhang, K. T. Ramesh, “*Microcompression of Nanocrystalline Nickel*,” Applied Physics Letters, Vol. 88, 2006, pp. 103112 - 103112-3 .

[78] D. Jang, J. R. Greer. “*Size-induced weakening and grain boundary-assisted deformation in 60*

*nm grained Ni nanopillar*,” Scripta Materialia, Vol. 64, 2010. Pp. 77-80.

[79] E. Czerwosz, P. Dłużewski, J. Kęczkowska, M. Kozłowski, M. Suchańska, and H. Wronka, “*Palladium nanocrystals and their properties*”, I State Conf. on Nanotechnology 188, (2007).

[80] J. Löffler, J. Weissmüller, “*Grain Boundary atomic structure in Nanocrystalline Palladium from x-ray atomic distribution Functions*,” Physical review B, Vol. 52,1995, pp. 7076–7093.

[81] J. Schiøtz, F. D. Di Tolla and K. W. Jacobsen, “*Softening of nanocrystalline metals at very small grain sizes*,” Nature, Vol. 391, 1998, p. 561.

[82] V. Yamakov, D. Wolf, S. R. Phillpot and H. Gleiter, “*Grain-boundary diffusion creep in nanocrystalline palladium by molecular-dynamics simulation*,” Acta Materialia, Vol. 50, 2002, pp. 61-73

[83] P. Kęblinski, D. Wolf, S.R. Phillpot, H. Gleiter, “*Structure of grain boundaries in nanocrystalline palladium by molecular dynamics simulation*,” Scripta Materialia, Vol. 41, 1999, pp. 631-636.

[84] P.G. Sanders, J. a Eastman, and J.R. Weertman, “*Elastic and tensile behavior of nanocrystalline copper and palladium*,” Acta Materialia, vol. 45, 1997, pp. 4019-4025.

[85] G.W. Nieman, J.R. Weertman and R.W. Siegel, “*Mechanical behavior of nanocrystalline metals*” Nanostructured Materials, Vol. 1, 1992, pp. 185-190 .

[86] P.G. Sanders, C.J. Youngdahl, J.R. Weertman, “*The strength of nanocrystalline metals with and without flaws*,” Evanston : s.n., Materials Science and Engineering, Vol. A2344236, 1997, pp. 77-82 .

[87] Y. Wei, A. F. Bower, H. Gao, “*Enhanced strain-rate sensitivity in f.c.c. nanocrystals due to grain-boundary diffusion and sliding*,” Acta Materialia, Vol. 56, 2008, pp. 1741-1752.

[88] Gumbusch, D.V. Bachurin and P. Karlsruhe, “*Molecular Dynamics Study of Plastic Deformation of nanocrystalline palladium*,” Germany : High Performance Computing in Science and Engineering, 2010.

[89] Robert J. Asaro, Subra Suresh, “*Mechanistic models for the activation volume and rate sensitivity in metals with nanocrystalline grains and nano-scale twins*,” Acta Materialia, Vol. 53,2005, pp. 3369–3382.

[90] R. Schwaiger, B. Moser, M. Dao, N. Chollacoop and S. Suresh, “*Some critical experiments on the strain-rate sensitivity of nanocrystalline nickel*,” Acta Materialia, Vol. 51, 2003, pp. 5159-5172.

[91] Z. Jiang, X. Liu, G. Li, Q. Jiang, and Jianshe Lian, “*Strain rate sensitivity of a nanocrystalline Cu synthesized by electric brush plating*” , Applied Physics Letters, 2006, Vol. 88.

[92] Planken, O. Van Der Biest and J. Van Der, “*The plastic deformation of indium single crystals*,” Acta Metallurgica, Vol. 21, 1973, pp. 1629-1639.

[93] B.N. Lucas, W. C. Oliver, “*Indentation power-law creep of high-purity indium*,” Metallurgical and Materials Transactions A, Vol. 30, 1999, pp. 601-610.

[94] U. Messerschmidt, “*Dislocation Dynamics During Plastic Deformation*,” Springer Series in Materials Science, Vol. 129, 2010.

- [95] J. Weertman, "Creep of indium, lead and some of their alloys with various metals," *Trans. Metallurg. Soc. AIME*, 1960, Vol. 218, p. 207.
- [96] F. Favier, E.C. Walter, M.P. Zach, T. Benter, and R.M. Penner, "Hydrogen sensors and switches from electrodeposited palladium mesowire arrays.," *Science (New York, N.Y.)*, vol. 293, Sep. 2001, pp. 2227-31.
- [97] M. Li, T.S. Mayer, J. a Sioss, C.D. Keating, and R.B. Bhiladvala, "Template-grown metal nanowires as resonators: performance and characterization of dissipative and elastic properties.," *Nano letters*, vol. 7, Nov. 2007, pp. 3281-4.
- [98] H.-A. Yang, M. Wu, and W. Fang, "Localized induction heating solder bonding for wafer level MEMS packaging," *Journal of Micromechanics and Microengineering*, vol. 15, Feb. 2005, pp. 394-399.
- [99] M. Uchic and D. Dimiduk, "A methodology to investigate size scale effects in crystalline plasticity using uniaxial compression testing," *Materials Science and Engineering A*, vol. 400-401, Jul. 2005, pp. 268-278.
- [100] J.R. Greer and J.T.M. De Hosson, "Plasticity in small-sized metallic systems: Intrinsic versus extrinsic size effect," *Progress in Materials Science*, vol. 56, Aug. 2011, pp. 654-724.
- [101] J. Greer and W. Nix, "Nanoscale gold pillars strengthened through dislocation starvation," *Physical Review B*, vol. 73, Jun. 2006, pp. 1-6.
- [102] J.-Y. Kim, D. Jang, and J.R. Greer, "Tensile and compressive behavior of tungsten, molybdenum, tantalum and niobium at the nanoscale," *Acta Materialia*, vol. 58, Apr. 2010, pp. 2355-2363.
- [103] M.J. Burek, A.S. Budiman, Z. Jahed, N. Tamura, M. Kunz, S. Jin, S.M.J. Han, G. Lee, C. Zamecnik, and T.Y. Tsui, "Fabrication, microstructure, and mechanical properties of tin nanostructures," *Materials Science and Engineering: A*, vol. 528, Jul. 2011, pp. 5822-5832.
- [104] M.J. Burek, S. Jin, M.C. Leung, Z. Jahed, J. Wu, A.S. Budiman, N. Tamura, M. Kunz, and T.Y. Tsui, "Grain boundary effects on the mechanical properties of bismuth nanostructures," *Acta Materialia*, vol. 59, 2011, pp. 4709-4718.
- [105] Ansel C. Ugural, *Mechanics of Materials, John Wiley and Sons, Inc.*, 2008
- [106] C.-L. Hsin, W. Mai, Y. Gu, Y. Gao, C.-T. Huang, Y. Liu, L.-J. Chen, and Z.-L. Wang, "Elastic Properties and Buckling of Silicon Nanowires," *Advanced Materials*, vol. 20, 2008, pp. 3919-3923.
- [107] M. Chang, J.R. Deka, and F.C. Chang, "Effect of synthesis process on the Young's modulus of titanate nanowire," *Physica Status Solidi (a)*, vol. 207, 2010, pp. 327-333.
- [108] A. A. Karimpoor and U. Erb, "Mechanical properties of nanocrystalline cobalt," *Physica Status Solidi (a)*, vol. 203, 2006, pp. 1265-1270.
- [109] *ASM Handbook Volume 8, Mechanical Testing and Evaluation*; The Materials Information Society: Materials Park, Ohio, 1990; p 2198.
- [110] M.J. Burek, A.S. Budiman, Z. Jahed, N. Tamura, M. Kunz, S. Jin, S.M.J. Han, G. Lee, C. Zamecnik, and T.Y. Tsui, "Fabrication, microstructure, and mechanical properties of tin nanostructures,"

*Materials Science and Engineering: A*, vol. 528, Jul. 2011, pp. 5822-5832.

[111] D. C. Gianola, C. Eberl, “*Micro- and nanoscale tensile testing of materials*,” *JOM*, vol. 61, 2007, pp. 24-35.

[112] A. B. Mann and J. B. Pethica, “*The role of atomic size asperities in the mechanical deformation of nanocontacts*” *Applied Physical Letters*, Vol. 69, 1996, p. 907.